**Title**
Stability, Sensitivity, and Selectivity of Graphene FET-based Gas Sensors

**Permalink**
https://escholarship.org/uc/item/3vr42589

**Author**
Hayasaka, Takeshi

**Publication Date**
2019

Peer reviewed|Thesis/dissertation

Stability, Sensitivity, and Selectivity of Graphene FET-based Gas Sensors

by

Takeshi Hayasaka

A dissertation submitted in partial satisfaction of the

requirements for the degree of

Doctor of Philosophy

in

Engineering - Mechanical Engineering

in the

Graduate Division

of the

University of California, Berkeley

Committee in charge:

Professor Liwei Lin, Chair
Professor Dorian Liepmann
Professor Ana Claudia Arias

Fall 2019

Stability, Sensitivity, and Selectivity of Graphene FET-based Gas Sensors

**Abstract**

Stability, Sensitivity, and Selectivity of Graphene FET-based Gas Sensors

by

Takeshi Hayasaka

Doctor of Philosophy in Engineering - Mechanical Engineering

University of California, Berkeley

Professor Liwei Lin, Chair


Miniaturized gas sensors are expected to witness a high demand in the next decade in various industry fields due to the small foot print, low power consumption, and low manufacturing cost. To date, various miniaturized gas sensors have been proposed by combining key sensing principles/materials and micro/nano fabrication technologies. Among those platforms, graphene-based gas sensor is especially promising due the unique features: gas sensing capability at room temperature, unique electrical properties, and the truly two dimensional structure. On the other hand, several issues have prevented the graphene-based gas sensors from being applied to practical gas sensing applications in the ambient air: the electrical properties of graphene-based gas sensors are susceptible to the environmental factors when they are operated at room temperature; the gas sensitivity is relatively low when compared with heated metal oxide (MOX) type gas sensors; and the poor gas selectivity. As for the poor gas selectivity issue, electronic nose has been proposed to tackle the issue; however, the sensor performance is severely constrained by the inefficient functionalization process. Therefore, in order to realize practical miniaturized gas sensors, a new class of gas sensing scheme is required.

The aim of this dissertation is to demonstrate a new class of miniaturized gas sensing platform by improving the stability, sensitivity, and selectivity of graphene-based gas sensors through fundamental properties of graphene, a novel measurement scheme, and microfabrication process.

The influences of temperature, $H_2O$ (humidity), and $O_2$ on the stability of the electrical properties and the gas sensing characteristics of graphene field effect transistor (GFET)-based gas sensors are studied as these environmental factors are often encountered in practical gas sensing applications. Both empirical results and theoretical analyses are characterized for heated GFET-based gas sensors from room temperature to 100 °C under a wide range of applied gate voltages. It is found that at a constant applied gate voltage of $-20$ V with respect to the gate voltage at the charge neutrality point $V_{NP}$, the sensitivity of the device to $H_2O$ decreases; while the sensitivity to $O_2$ decreases first, and increases afterwards as the operation temperature increases. These phenomena are explained by using the physisorption

and chemisorption models between the tested gases and the graphene surface. Furthermore, devices operate in the hole regime result in lower sensitivity to $H_2O$ and $O_2$ as compared to those results for the electron regime. As such, these studies provide foundations to improve the stability of GFET-based gas sensors in practical application environments under the influences of ambient air, temperature, and humidity.

Unique graphene-catalyst hybrid structure is proposed to realize both high gas sensitivity and reproducibility. The proposed device structure is readily realized by standard MEMS fabrication process. For the catalytic layer, atomic layer deposition (ALD) $RuO_2$ is used. The gas sensing properties of a pristine-GFET and a ALD-$RuO_2$ functionalized GFET are compared. Three distinctive advancements have been achieved: (1) enhanced sensitivity using the scheme of electron mobility characterizations by a hybrid structure of graphene and ALD-$RuO_2$ base layer; (2) first demonstration of gas sensing by means of the 4-dimentional (4D) physical properties vectors of graphene FETs; and (3) using the 16-dimensional (16D) characteristic gas sensing pattern to distinguish water vapor and methanol. As such, the proposed unique device structure and the measurement scheme could offer enhanced sensitivity as well as selectivity.

The poor gas selectivity problem has been a long-standing issue for miniaturized chemiresistor type gas sensors. An e-nose system based on a single GFET is developed to achieve selectivity, miniaturization, low cost, and low power consumption. Instead of using multiple functional materials, the gas sensing conductivity profiles of a GFET are recorded and decoupled into four distinctive physical properties and projected onto a feature space as 4D output vectors and classified to differentiated target gases by using machine learning analyses. Our single-GFET approach coupled with trained pattern recognition algorithms was able to classify water, methanol, and ethanol vapors with high accuracy quantitatively. Furthermore, the gas sensing patterns of methanol were qualitatively distinguished form that of water vapor in a binary mixture condition, suggesting that the proposed scheme is capable of differentiating a gas in the realistic scenario of ambient environment with background humidity. As such, this work offers a new class of e-nose sensing scheme using a single GFET without multiple functional materials towards practical gas sensing applications.

*To my parents*

# Contents

# List of Figures

# List of Tables

# Acknowledgments

I would like to thank my research advisor, Professor Liwei Lin, for his guidance and supports throughout the times of good and bad in my graduate career. I have been fortunate to have had the opportunity of leaning how he approaches research challenges and many other issues in real life. What I have learnt in my academic training under his guidance will protect me over the course of my life. What I appreciate the most about him is all the given opportunities interacting with the people at Berkeley including those who are mentioned here.

I owe deep gratitude to my qualifying examination and dissertation committee, Professor Dorian Liepmann, Professor Hayden Taylor, Professor Ana Claudia Arias, and Professor Zi Qiang Qiu, for finding their time to review my work and providing valuable inputs.

I would also like to thank Yumeng (Simon) Liu with whom I spent most of my time at UC Berkeley. We had worked together on the same projects for two years. He trained me on all the necessary tools for our projects in Marvell Nanofabrication Laboratory with patience, mostly over weekends in order to avoid conflict with my course works. He taught me the fundamental knowledge of our research, how to build up scientific discussions, how to construct research presentation slides, and how to make a good presentation. Whenever I was not confident about what I was doing, he encouraged me with humor. He was a mentor, teacher, and good friend. I consider the time I spent with him is the best part of my life at UC Berkeley. In addition, I enjoyed listening political discussions between Simon and Hyun Sung Park.

I also owe many thanks to Huiliang Liu and Yoshihiro Kubota for their dedications to our projects. Huiliang Liu's contributions include but not limited to most of the key experiments, development of the most complicated part of the MATLAB codes, documentation of the experimental results, analyses, publications, presentations, and initiatives in the meetings with our funding agencies. Yoshihiro Kubota stayed at Berkeley for one year and literally saved my graduate career. When we built a new experimental setup, he built up majority of the software and hardware systems from scratch. He learnt LabVIEW on his own, designed all the necessary programs, and made us possible to carry out our experiments automatically. He kept working hard until the very last minute of his stay at Berkeley so that I did not have to encounter any technical issue on conducting my experiments. Our work would not have been possible without these two persons.

I was also very fortunate to collaborate with Albert Lin. I have closely worked with him in the last one year of my graduate career. He was responsible for the analysis part in our project. He learnt Machine Learning Analysis on his own, acquired the related knowledge quickly with deep understanding, and gave a new perspective to our research. He alway moved quickly and completed our tasks ahead of time.

To my billiards buddies, Vernalyn C. Copa, Lorenzo P. Lopez Jr., Regine A. Loberternos, Laureen Ida M. Ballesteros, Rogie M. Madula, Jamela Pangasinan, Ilbey Karakurt, and Sedat Pala; I thank you all for sharing the fun Friday nights. I think I improved my skill the most through the games with Regine A. Loberternos.

I am also thankful to my roommates in the first year at Berkeley, Paolo Toni and Erina Yokosuka. Thank you for sharing many experiences, chatting, exploring the town together, and being good roommates.

Another special thanks to Tomohiro Ishikawa and Professor Takeshi Kawano, who provided many valuable information and advices for me before I came to Berkeley. They told me how Berkeley is a nice place, and now I can agree with them.

During my graduate career, several Japanese people have visited the Lin lab, Professor Ken Saito, Dr. Kento Kariya, Dr. Yuki Ohara, and Professor Junji Sone; I would like to thank them for their open-mindedness, casual conversations, and for sharing a lot of fun times.

I would like to express my gratitude to my father who had been always encouraging me pursuing my own path, although he cannot see my work today. I would like to thank my mother for her unconditional love. I would also like to thank my brother who has been always cheering the family with humor. Last, but not least, I would like to express my sincerest thanks to my sister who has been taking care of my mother and many other things from the time when I came to Berkeley to the present. I have been able to pursue my graduate career at Berkeley because of her.

# Chapter 1

# Introduction

## 1.1  Abstract

In this chapter, the background and the motivation of this dissertation are introduced. The demand for miniaturized gas sensors has been grown rapidly in the recent years due to the various driving factors. The gas sensor market forecasts further growth in the next decade foreseeing emerging applications. To date, various miniaturized gas sensors have been developed by combining key sensing principles/materials and micro/nano fabrication technologies. Although miniaturization itself has been successfully demonstrated in the past, some of the sensor performances have been compromised mainly due to the unavoidable trade-offs. Graphene-based gas sensors have emerged in the last decade as novel chemical-to-electrical transducers with several unusual physical properties. Yet the poor gas selectivity issue has severely constrained the graphene-based gas sensors being applied to practical applications. On the other hand, the advantages of the electrical tunability of the graphene field effect transistor (FET) based gas sensors have not been fully explored in previous studies, while the fundamental physical properties of graphene have been extensively studied.

This dissertation aims to study the poor gas selectivity issue of graphene-based gas sensors through fundamental properties of graphene, development of a novel measurement scheme, and microfabrication process.

## 1.2  Miniaturized Gas Sensors

### 1.2.1  Demand on miniaturized gas sensors

Miniaturized gas sensors are expected to witness a high demand in the next decade in various sectors including industrial, consumer electronics, automotive, medical, environmental, and petrochemical fields, due to the small foot print, low power consumption, and low manufacturing cost [1–3]. The examples of applications in each sector are described below:

- Industrial: Monitor $CO_2$ level to control heating, ventilating, and air conditioning (HVAC) systems efficiently; monitor $CO_2$ level in storage units as an indicator of early food spoilage.

- Consumer electronics: Detect alcohols, CO, $CO_2$, $NO_2$, and volatile organic compounds (VOCs) by integrating miniaturized gas sensors into smartphones, tablets, and wearable devices.

- Automotive: Monitor emission levels (e.g., $NO_2$) and minimize vehicle energy consumption levels.

- Medical: $O_2$ gas sensors are required for anesthesia machines, ventilators, and $O_2$ monitors.

- Environmental: Wireless gas sensor networks are demanded for continuous and real-time environmental monitoring systems.

- Petrochemical: Wireless gas sensor networks are demanded to detect explosive and/or toxic gases in work places.

The major driving factors of the growing demand include demand for continuous and real-time indoor and outdoor air quality monitoring [4, 5], increasing enforcement of occupational health and safety regulations by governments [6], and demand for emerging consumer electronics applications [7].

By taking the advantages of several unique features, which conventional bulky gas sensors do not possess, miniaturized gas sensors could offer both mobile gas sensing platforms and spatially distributed usages. These highly desirable platforms can stimulate emerging gas sensing applications such as preventive health care with mobile devices, including smartphones. For example, some of the VOCs in human breath are known as biomarkers for clinical diagnostics; $NH_3$ and NO are related to helicobacter pylori infections of stomach and asthma, respectively [8]. On the other hand, spatially distributed gas sensing platforms are suitable to monitor air pollution (e.g., CO, $NO_2$, and $SO_2$) with high spatial resolution [5].

## 1.2.2 Examples of miniaturized gas sensors

To date, various miniaturized gas sensors have been proposed by combining key sensing principles/materials and micro/nano fabrication technologies [9, 10]. In this subsection, several types of miniaturized gas sensors are introduced.

### 1.2.2.1 Metal oxide semiconductor (MOX) type gas sensors

Metal oxide semiconductor (MOX) type gas sensors have been widely used since its emergence in 1970's due to the high sensitivity and low cost [11, 12] as they have been further miniaturized in recent years with $<10$ mm$^2$ foot prints [12, 13].

A schematic of the working principle of MOX type gas sensors is shown in Fig. 1.1. The surface of MOX type gas sensors may be covered with chemisorbed oxygen species as $O_2^-$, $O^-$, or $O^{2-}$, depending on the nature of MOX and the operating temperature (Fig. 1.1**a**). The chemisorbed oxygen species deplete electrons from the surface of the MOX. The depleted region is also called space charge region (SCR). The surface electric potential $V_s$ associated with SCR creates Schottky barriers at the grain boundaries. Therefore, the electrical conductivity of the MOX is reduced due to the chemisorbed oxygen species on the surface. Upon exposure to reducing gases, e.g., CO, the trapped electrons are released into the SCR after that the chemisorbed oxygen species oxidize the reducing gases (Fig. 1.1**b**). The electrical conductivity increases as the SCR diminishes with lowered Schottky barriers by $\Delta eV_s$. As such, the electrical conductivity of MOX type gas sensors are modulated by the presence of target gases [14].
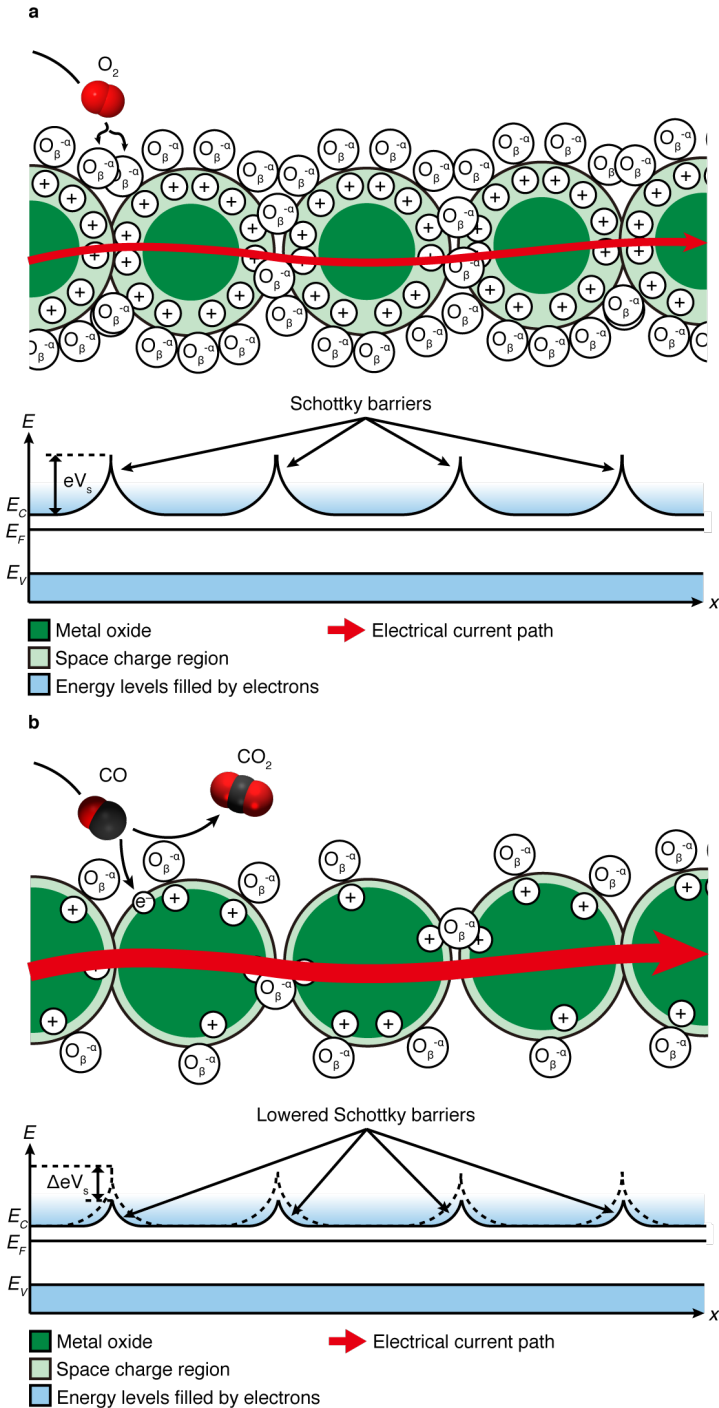
Figure 1.1: Schematic of the structural and electron energy band models of MOX type gas sensors before **a** and after **b** exposure to reducing gas (CO in this case).

Important factors influencing the gas sensing performance of MOX type gas sensors include the chemical composition of the sensing materials, micro/nano-scale structures (surface area), additive catalysts (usually noble metals), pre-adsorbed species on the surface, device design including heater and electrode, operation temperature, and humidity level. Regarding the sensing materials, the early works focused on $SnO_2$ and ZnO in 1960's-1970's, followed by various other oxide materials including $WO_3$, $TiO_2$, and $In_2O_3$. More recently, the sensing elements have been integrated with micro hotplates and micro electronics achieving lower power consumption, low manufacturing cost, faster response, and higher sensitivity, owing to the recently advanced micro electro mechanical systems (MEMS) technologies [12, 14].

Although MOX type sensor is one of the most widely accepted gas sensing technologies, the poor gas selectivity has been a long-standing issue [9]. Another major drawback is the relatively high power consumption (typically in the order of several tens of mW) associated with the high operation temperature (typically >200 °C) [15].

### 1.2.2.2 Electrochemical type gas sensors

Electrochemical type gas sensors, specifically, amperometric type gas sensors, have been widely used to detect various gases including $H_2$, $O_2$, CO, $NO_2$, NO, $O_3$, $SO_2$, $H_2S$, and volatile organic compounds (VOCs). A simplified schematic of the basic sensor configuration of an electrochemical (amperometric) gas sensor is illustrated in Fig. 1.2. A typical electrochemical type gas sensor is composed of gas membrane, working electrode, counter electrode, reference electrode, electrolyte, and casing structure. When an electrochemical type gas sensor is exposed to a target gas, the gas molecules diffuse into the membrane and come in contact with the working electrode/electrolyte interface. Under a proper applied potential, redox reaction will occur on the working electrode and on the counter electrode. Electrons associated with the reaction will pass through the external circuit between the working electrode and the counter electrode, while the electrolyte transports ions such that a electrical current flows the sensor [16].

From the 1980's, microelectrodes have been developed by using MEMS technologies, and it enabled miniaturization of electrochemical type gas sensors. Miniaturization realizes faster sensor response time, higher sensitivity, and lower manufacturing cost [16].

The major advantages of electrochemical type gas sensors include the relatively high selectivity, highly linear sensor response, high sensitivity (ppm order), and relatively low manufacturing cost. On the other hand, the major drawbacks include the limited operation temperature range, temperature depend performance, relatively short lifetime, and cross-sensitivity.
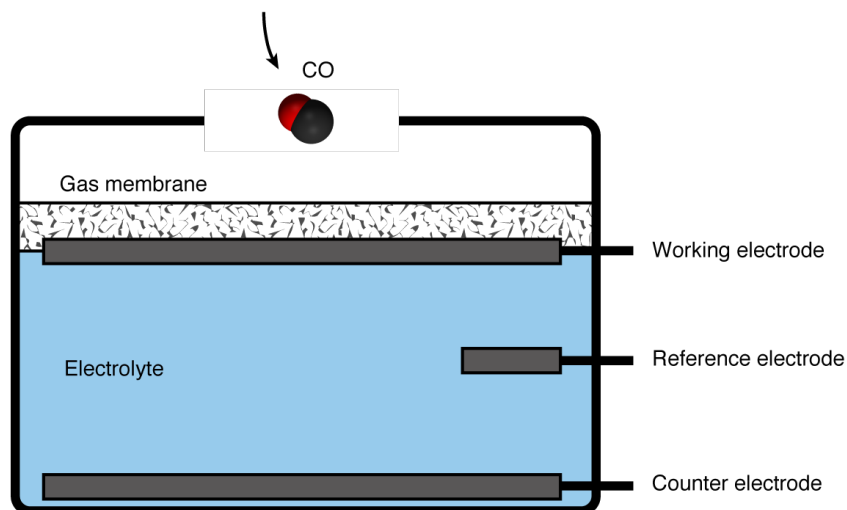
Figure 1.2: Simplified schematic of an electrochemical type gas sensor structure.

### 1.2.2.3   Optical type gas sensors

Optical type gas sensors have several advantages including higher selectivity, stability, and much longer lifetime. A simplified schematic of optical type gas sensor structure is illustrated in Fig. 1.3. Optical type sensors are composed of three major components: light source, sample cell (also optical path), and light detector. Infrared (IR) light source is predominantly used as its interference with mist and particulate matters are smaller than that of other frequency bands. Due to the negligible optical dispersion, the IR is also called non-dispersive infrared (NDIR). Gas molecules passing through the sample cell of an NDIR type gas sensor absorb specific energy of IR, thereby a unique IR spectrum is obtained for each gas type. This working principle leads to inherently high gas selectivity and stability. In addition, the system do not require frequent maintenance as the components do not chemically react with target gases. NDIR type gas sensor is especially advantageous to detect $CO_2$ as $CO_2$ is difficult to detect by using other technologies due to the chemically inert nature [17].

The drawbacks of the optical type gas sensors include the relatively larger structure, higher power consumption, higher manufacturing cost, and complexity of the system. Recently, miniaturized optical type gas sensors have been developed by utilizing miniaturized infrared (IR) source and detectors, however, the size of the device is still much larger than that of MOX type gas sensors.
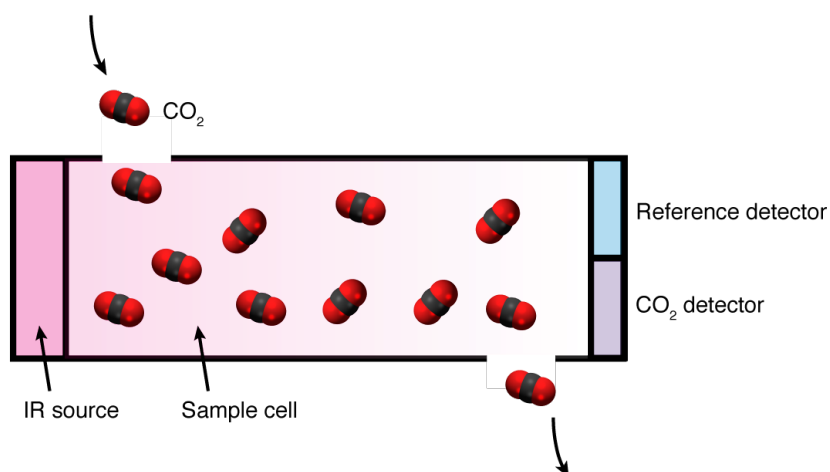
Figure 1.3: Simplified schematic of optical type gas sensor structure.

### 1.2.3 Summary

In the previous subsection, three types of miniaturized gas sensors were introduced. The cross-selectivity is a common issue for both MOX and electrochemical type gas sensors while they have several advantages as miniaturized gas sensors. In contrast, optical type gas sensors have high gas selectivity while they are expensive and bulky compared with MOX and electrochemical type gas sensors. The drawbacks of each technology can be compensated by combining different types of gas sensors into one system; however, such system tend to be bulky, power-hungry, and expensive. Therefore, despite the fact that several gas sensing technologies are available, further studies will be required to realize a miniaturized gas sensing system for practical applications.

## 1.3 Graphene-Based Gas Sensors

Graphene is a monolayer of carbon atoms experimentally obtained in 2004 as a stable structure under ambient conditions [18]. After its discovery, the fundamental properties and the potential applications have been extensively studied [19]. Graphene-based gas sensor is one of the most promising applications as graphene's inherent properties are well suited for chemical transducers. The advantages of graphene as a gas sensing material include the high surface area to volume ratio, high conductivity with low Johnson-Nyquist noise, and low 1/f noise due to few crystal defects. These features contribute to maximize the signal to noise ratio, i.e., the gas sensitivity [20].

One of the most attractive features of graphene-based gas sensors is the high gas sensitivity at room temperature, which leads to the low power consumption, typically in the

order of a few tens of $\mu$W. This is very different from MOX type gas sensors which are typically operated at >200 °C, therefore the typical power consumption is in the order of several tens of mW. Power consumption is one of the most important criteria for miniaturized gas sensor applications as mentioned in the previous section. In addition, graphene's truly two-dimensional structure is compatible with standard MEMS batch fabrication process, such that both miniaturization and lower manufacturing cost can be realized. Moreover, the contact resistance can be minimized by patterning the electrodes in a four-probe configuration (Fig. 1.4).
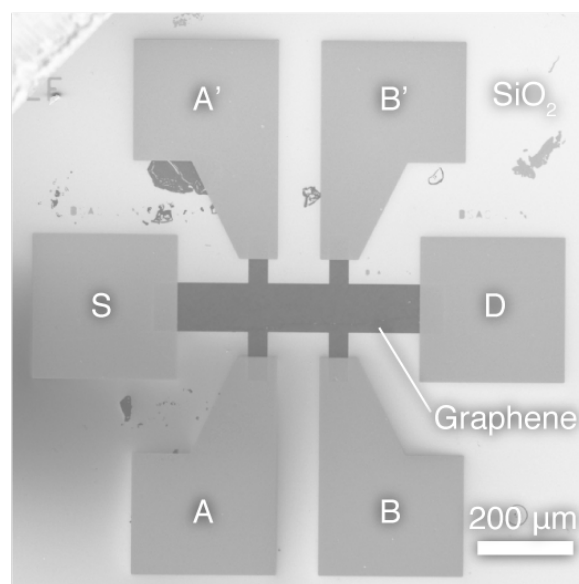


Figure 1.4: A graphene-based gas sensor with four-probe configuration. An electrical current is supplied between S and D. The voltage across A and B is measured. A' and B' may be used for the Hall measurement or as spare inner electrodes.


There are mainly two methods to synthesize large scale graphene: chemical vapor deposition (CVD) and epitaxial growth. Graphene can be epitaxially grown on a SiC wafer under high temperature. Although the quality of epitaxially grown graphene is high, SiC wafer is expensive and the transfer process to other wafers is difficult. CVD graphene can be synthesized on metal substrate such as Cu and Ni. $CH_4$ and $H_2$ are generally used as carbon source and carrier/etching gas. CVD graphene can be transferred onto various materials with large scale, while the transfer process may induce more defects [21]. At present, large scale graphene is commercially available in the market. Therefore, the manufacturing process of graphene-based gas sensors can be potentially scaled up.

Due to the facts mentioned above, graphene-based gas sensor is a promising platform for miniaturized gas sensor applications. The low power consumption is especially advantageous

compared with MOX type gas sensors. On the other hand, graphene-based gas sensors have suffered from the poor gas selectivity issue. This issue is the central topic of this dissertation and will be discussed further in later chapters.

## 1.4  Electronic Nose

In various fields, evaluation of odor of interest has been a critical factor for various purposes [22, 23]. For example, in food and beverage industry, evaluation of odor is required for variety of processes: (1) inspection of quality of products to avoid spoilage; (2) control of ripening or fermentation; and (3) quality classification of the same product. Conventional methods for the above processes include human sensory panels and classical analytical systems such as gas chromatography-mass spectrometry (GC-MS). Another example is disease diagnosis. Some of volatile organic compounds (VOCs) contained in exhaled breath can be directly linked to specific diseases. Therefore, noninvasive disease diagnosis is possible by using GC-MS. While GC-MS is advantageous for a quantitative analysis, it not only requires both specialized expensive equipment and highly trained personnel for the operation, but also is time consuming [24]. Therefore, in the past few decades, there has been a demand to replace the conventional expensive methods to less expensive methods. One of the promising analytical systems is called electronic nose (or e-nose).

The concept of electronic nose appeared around the late 1980's. The term, electronic nose, can be defined as: *An instrument, which comprises an array of electronic chemical sensors with partial specificity and an appropriate pattern-recognition system, capable of recognising simple or complex odors* [23]. The key concept of the electronic nose is to mimic the entire mammalian olfactory system by using engineering approach. In the mammalian olfactory system, each olfactory receptor has multiple sites for odorant binding, enabling the detection of more than one odorant for each olfactory receptor. Each combination of activated receptors generates a unique code for a specific odorant, making it possible to distinguish between thousands of odorants. On the other hand, the counterparts in the artificial e-nose are cross-sensitive artificial sensor arrays, signal transducers, and signal processing followed by data analysis with pattern recognition algorithms. E-nose has been intensively studied from late 1980's to 1990's. Although several studies have successfully demonstrated classifying different type of odors of interest, such as foods, beverage, and VOCs, only few technologies have been transferred into commercial products [25, 26].

A sensor array in an e-nose system generates output vectors which are projected to a feature space. A feature space is an abstract space in which each output vector is represented as a point and the dimension of the output vector is determined by the number of features evaluated. In order to realize higher analytical capabilities, a higher dimensionality in a feature space is desired for sufficient information. Ideally, the axes in a feature space are orthogonal to each other. There are several different factors which can be tuned in order to increase the dimensionality of a feature space: sensing materials, transducers, geometries of transducers, modulations of parameters and their combinations (e.g., bias voltage, temper-

ature, and gas flow) [27]. Obviously, a sensor array with identical multiple sensor elements do not increase the dimensionality of a feature space by itself as it will end up with one dimensional feature space. Thus, as described above, one or more factors must be properly tuned for a higher dimensionality in a feature space. Therefore, for the development of e-nose systems, the central interests have been increasing the dimensionality in the feature spaces and the improvement of pattern recognition methods.

Several different types of e-nose have been developed in the past few decades and they are summarized in Table 1.1. In the early stage of the development, the e-nose systems were constructed by assembling multiple commercial individual metal oxide gas sensors. $SnO_2$ based Taguchi gas sensors (TGS) from Figraro Engineering Inc. were repeatedly used as the sensor elements [28–31]. The output data set obtained from an e-nose system has the unique feature for each odor and thus it can be used to classify different odors. In cluster analysis, the output data set from N-sensor units can be regarded as N-dimensional pattern vectors, and the pattern vectors are supposed to be different for different odors [29, 30, 32]. In addition to the cluster analysis, various other pattern recognition algorithms were applied to e-nose such as multivariate analysis [29], artificial neural network [33, 34], and principal component analysis [25, 35–37]. For the sensor elements and transducers, MEMS technologies have been employed to realize miniaturized e-nose [36–38]. MEMS-based e-nose systems have employed several different gas sensing mechanisms: metal oxide with micro hotplate [38], piezotransduced single-crystal silicon bulk acoustic resonators with self assembled monolayers [36], and polymer carbon black composite [37]. It is important to mention that these MEMS-based e-nose systems require additional post processes for sensor element-specific properties, and these processes are not batch fabrication process. Therefore, while the e-nose systems can be miniaturized by MEMS technologies, the number of sensor elements is still limited by the sensor element-specific processes. In fact, the number of sensor elements in MEMS-based e-nose systems [36–38] are comparable or even smaller to macro scale e-nose systems [28–31]. As discussed above, the number of sensor elements is a critical factor to achieve a reliable e-nose system.

The remaining challenges in the development of e-nose can be classified into a few major categories: integration of sensor elements with efficient functionalization method, improvement of sensitivity, compensation of interference from humidity in the ambient air. As it is described above, it is not efficient way to modify the properties of metal oxide based sensor elements one by one, while the sensitivity of metal oxide based sensors are generally high enough for various target gases. Similarly, polymer-based sensor elements cannot be integrated by using conventional complementally metal oxide semiconductor (CMOS) compatible processes. Also, polymer-based e-nose may have long term stability issue, i.e., degradation of the active materials over time, and drift issue due to humidity. Inefficient integration processes end up with a smaller number of sensor elements and thus a smaller dimension in a feature space. This deficiency limits not only the analytical capabilities of e-nose, but also the miniaturization.

| Year | # of sensors | Sensor type | Materials | Target | Pattern recognition techniques | Ref. # |
|------|------|------|------|------|------|------|
| 1982 | 3 | Metal oxide | $SnO_2$ (TGS, Figaro) | VOCs | Comparing the ratio of the signals | [28] |
| 1991 | 6 | Metal oxide | $SnO_2$ (TGS, Figaro) | Coffee aroma | Multivariate analysis, cluster analysis, linear discriminant analysis | [29] |
| 1987 | 8 | Metal oxide | $SnO_2$ (TGS, Figaro) | VOCs | Cluster analysis | [30] |
| 1990 | 12 | Metal oxide | $SnO_2$ (TGS, Figaro) | VOCs | Weighted fault-tolerant least-squares method | [31] |
| 1993 | 8 | Quartz resonator and sensing membrane | Celluloses and lipids | Perfume | Neural network | [33] |
| 1993 | 12 | Conductive polymer | Poly-(pyrrole) | Beer | Cluster analysis | [32] |
| 1986 | 12 | Surface acoustic wave and coating | Polymer | VOCs | Principal component analysis, cluster analysis | [35] |
| 1993 | 10-15 | MOSFET with catalyst, TGS, NDIR | Pd, Ir, Pt, $SnO_2$ (TGS, Figaro) | Meat | Neural network | [34] |
| 2006 | 3 | Metal oxide | $SnO_2$ doped with Pt, Pd | Cigarette smoke, fast-food odor | Simple vector comparison in 3D data space | [38] |
| 2017 | 3 | PSBAR with self-assembled monolayers | GPTES, OTES, BPTS | VOCs | Principal component analysis | [36] |
| 2001 | 6 | Plymer-carbon black composite film | Polymer-carbon black composite | VOCs | Principal component analysis | [37] |
| N.A. | 32 | NoseChip nanocomposite | Nanocomposite | Aroma | PCA, KNN, Kmeans, CDA, SVM | [25] |

Table 1.1: Previous works on electronic nose

## 1.5 Dissertation Aim and Scope

As described in the previous sections, miniaturized gas sensors are expected to witness a high demand in the next decade in various industry fields due to the unique features. To date, various miniaturized gas sensors have been proposed by combining key sensing principles/materials and micro/nano fabrication technologies. Among those platforms, graphene-based gas sensor is especially promising due to the gas sensing capability at room temperature, unique electrical properties, and the truly two dimensional structure. On the other hand, the poor gas selectivity has been a critical issue for graphene-based gas sensors as well as for MOX type gas sensors. E-nose has been proposed to tackle the gas selectivity issue; however, the sensor performance is severely constrained by the inefficient functionalization

process. Therefore, in order to realize practical miniaturized gas sensors, a new class of gas sensing scheme is required.

The aim of this dissertation is to demonstrate a new class of miniaturized gas sensing platform by improving the stability, sensitivity, and selectivity of graphene-based gas sensors through a study of fundamental properties of graphene, a novel measurement scheme, and microfabrication process. Therefore, this dissertation focuses on the design, fabrication, and characterization of graphene-based gas sensors. In Chapter 2, the fundamentals of gas sensing based on graphene field effect transistor (FET) are described. Graphene FET is a powerful platform to study the gas sensing capability of graphene in depth owing to the tunable electrical properties. Chapter 3 discusses the influence of environmental factors on the stability of the electrical properties and the gas sensing properties of graphene FETs with a representative result shown in Fig. 1.5**a**. In order to explore possible calibration/compensation schemes, the influence of the operation temperature, $H_2O$ (humidity), $O_2$, and the gate voltage are studied. Chapter 4 discusses a chemical functionalization process via atomic layer deposition (ALD) to improve the sensitivity of graphene FET based gas sensors. ALD process is employed to realize a smooth catalytic base layer in a reproducible manner. In order to realize both high sensitivity and reproducibility, unique design is proposed for the graphene-catalyst hybrid sensing element (Fig. 1.5**b**). The proposed design is readily realized through standard MEMS fabrication process. Chapter 5 demonstrates an e-nose using a single graphene FET to address the gas selectivity issue. A novel measurement scheme is developed through a study of the fundamental properties of graphene FET. The tested gases are classified by signal processing and machine learning analysis. A representative result shown in Fig. 1.5**c**. Chapter 6 concludes this dissertation and discusses some possible future directions for this research.
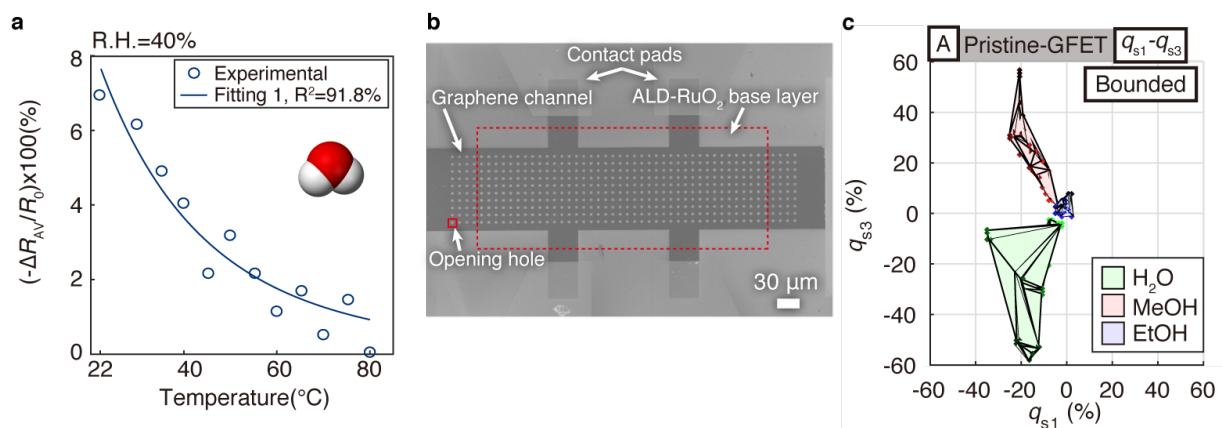
Figure 1.5: Some highlights in this dissertation. **a** Experimentally obtained sensitivity to $H_2O$ with respect to temperature and the fitting curve based on the physisorption model (taken from chapter 3). **b** Functionalized graphene FET via ALD process (taken from chapter 4). **c** 3D gas sensing patterns obtained by decoupling the electrical output signals (taken from chapter 5).

# Chapter 2

# Fundamentals of Gas Sensing Based on Graphene FETs

## 2.1 Abstract

In this chapter, the fundamentals of gas sensing based on graphene FETs are reviewed. The unique electrical properties of graphene are the direct consequence of the crystal structure of graphene. According to the linear energy dispersion relationship near the Dirac points, the electrons are considered to be *massless Dirac fermions* with exceptionally high carrier mobility. Due to the zero band gap and the Fermi level tunability with the FET configuration, the majority carrier of graphene can be either electron or hole depending on the Fermi level. The electrical properties of graphene including the carrier concentration $n$ and the carrier mobility $\mu$ can be comprehensively analyzed by using graphene FETs. Graphene FET structure can be readily fabricated by using standard MEMS fabrication processes, which are cost efficient batch fabrication. The gas-graphene interactions are divided into three major phenomena: gas adsorption, charge transfer, and charged impurity scattering. In order to take full advantage of the graphene FET structure, two major gas sensing schemes are introduced.

## 2.2 Electrical Properties of Graphene

Electrical properties of solids are determined by their electronic band structures. In this subsection, the electrical properties of graphene are described based on the electronic band structure. First, the electronic band structure is derived from the crystal structure of graphene. Graphene is made out of carbon atoms arranged in honeycomb crystal structure as shown in Fig. 2.1**a** [39]. Among the four valence electrons of carbon atoms, the three in-plane $sp^2$ hybridized orbitals contribute to the covalent bonding with the three nearest neighboring atoms and form $\sigma$ bands. The out-of-plane $2p_z$ orbital forms half-filled $\pi$ bands where the electrons are delocalized. Hence, the $\sigma$ and $\pi$ bands are responsible for the mechanical and
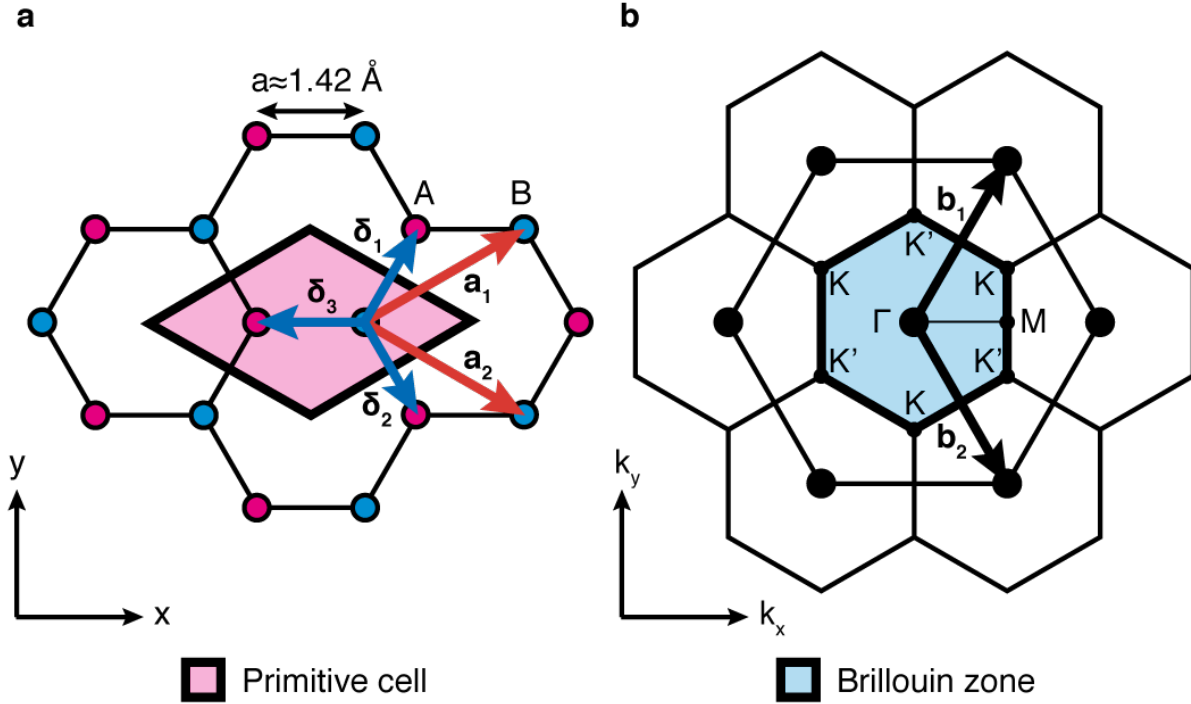
Figure 2.1: Honeycomb lattice and Brillouin zone of graphene. **a**: Lattice structure of graphene, made out of two interpenetrating triangular lattices ($\boldsymbol{a}_1$ and $\boldsymbol{a}_2$ are the lattice unit vectors, and $\boldsymbol{\delta}_i, i = 1, 2, 3$ are the nearest-neighbor vectors). **b**: Corresponding Brillouin zone. The Dirac cones are located at the $\boldsymbol{K}$ and $\boldsymbol{K}'$ points.

electrical properties of graphene, respectively. In the real space (Fig. 2.1**a**), the primitive cell of graphene is composed of two atoms with the primitive translation vectors written as [39]

$$\boldsymbol{a}_1 = \frac{a}{2}\left(3, \sqrt{3}\right), \quad \boldsymbol{a}_2 = \frac{a}{2}\left(3, -\sqrt{3}\right) \tag{2.1}$$

where $a \approx 1.42$ Å is the distance between the nearest neighboring carbon atoms. In the reciprocal space, the first Brillouin zone is also a hexagonal structure as shown in Fig. 2.1**b**, and the primitive vectors of the reciprocal lattice are written as [39]

$$\boldsymbol{b}_1 = \frac{2\pi}{3a}\left(1, \sqrt{3}\right), \quad \boldsymbol{b}_2 = \frac{2\pi}{3a}\left(1, -\sqrt{3}\right) \tag{2.2}$$

satisfying

$$\boldsymbol{a}_i \cdot \boldsymbol{b}_j = 2\pi\delta_{ij} \tag{2.3}$$

We establish the electronic band structure, i.e. $E\text{-}k$ dispersion relationship, for the electrons in the $\pi$ bands, considering the predominant contributions to the electrical properties, while

neglecting the influence from the $\sigma$ bands. We apply a tight binding model which is an opposite extreme case of the nearly free electron models, based on the following assumptions: (1) the electrons are tightly bound to the atoms; (2) the interactions with other electrons and potentials on surrounding atoms are limited; and (3) the wave functions can be expressed by a superposition. Considering the electrons in the $\pi$ bands only hop to the nearest neighboring sites, the tight binding Hamiltonian can be written as [39]

$$\hat{H} = -t \sum_i \sum_j \left( \hat{a}_i^\dagger \hat{b}_j + \hat{b}_j^\dagger \hat{a}_i \right) \tag{2.4}$$

where $\hat{a}_i(\hat{a}_i^\dagger)$ and $\hat{b}_j(\hat{b}_j^\dagger)$ are operators which annihilate (create) an electron on site $\boldsymbol{r}_i$ on sublattice $A$ and $B$, $t$ ($\approx$ 2.8 eV) is the nearest neighbor hopping energy. Next, let's define the nearest neighbor vectors in real space [39]

$$\boldsymbol{\delta}_1 = \frac{a}{2}\left(1, \sqrt{3}\right), \quad \boldsymbol{\delta}_2 = \frac{a}{2}\left(1, -\sqrt{3}\right), \quad \boldsymbol{\delta}_3 = -a\left(1, 0\right) \tag{2.5}$$

then the summation in Eq. (2.4) may be written as

$$\sum_i \sum_j \left( \hat{a}_i^\dagger \hat{b}_j + \hat{b}_j^\dagger \hat{a}_i \right) = \sum_i \sum_{\boldsymbol{\delta}} \left( \hat{a}_i^\dagger \hat{b}_{\boldsymbol{r}_i+\boldsymbol{\delta}} + \hat{b}_{\boldsymbol{r}_i+\boldsymbol{\delta}}^\dagger \hat{a}_i \right) \tag{2.6}$$

where $\hat{b}_{\boldsymbol{r}_i+\boldsymbol{\delta}}(\hat{b}_{\boldsymbol{r}_i+\boldsymbol{\delta}}^\dagger)$ annihilates (creates) an electron at the nearest neighboring $B$ site whose position is $\boldsymbol{r}_i+\boldsymbol{\delta}$. Given the translational invariance of the system, the annihilation (creation) operators can be written as [40]

$$\hat{a}_i = \frac{1}{\sqrt{N}} \sum_{\boldsymbol{k}} e^{i\boldsymbol{k}\cdot\boldsymbol{r}_i} \hat{a}_{\boldsymbol{k}} \qquad \hat{a}_i^\dagger = \frac{1}{\sqrt{N}} \sum_{\boldsymbol{k}} e^{-i\boldsymbol{k}\cdot\boldsymbol{r}_i} \hat{a}_{\boldsymbol{k}}^\dagger$$

$$\hat{b}_{\boldsymbol{r}_i+\boldsymbol{\delta}} = \frac{1}{\sqrt{N}} \sum_{\boldsymbol{k}'} \sum_{\boldsymbol{\delta}} e^{i\boldsymbol{k}'\cdot(\boldsymbol{r}_i+\boldsymbol{\delta})} \hat{b}_{\boldsymbol{k}'} \quad \hat{b}_{\boldsymbol{r}_i+\boldsymbol{\delta}}^\dagger = \frac{1}{\sqrt{N}} \sum_{\boldsymbol{k}'} \sum_{\boldsymbol{\delta}} e^{-i\boldsymbol{k}'\cdot(\boldsymbol{r}_i+\boldsymbol{\delta})} \hat{b}_{\boldsymbol{k}'}^\dagger \tag{2.7}$$

using Bloch's theorem. Hence, Eq. (2.4) may be rewritten with the help of Eqs. (2.6) and (2.7)

$$\hat{H} = -\frac{t}{N} \sum_i \sum_{\boldsymbol{\delta}} \sum_{\boldsymbol{k}} \sum_{\boldsymbol{k}'} \left[ e^{-i\left(\boldsymbol{k}-\boldsymbol{k}'\right)\cdot\boldsymbol{r}_i} e^{i\boldsymbol{k}'\cdot\boldsymbol{\delta}} \hat{a}_{\boldsymbol{k}}^\dagger \hat{b}_{\boldsymbol{k}'} + e^{i\left(\boldsymbol{k}-\boldsymbol{k}'\right)\cdot\boldsymbol{r}_i} e^{-i\boldsymbol{k}'\cdot\boldsymbol{\delta}} \hat{b}_{\boldsymbol{k}'}^\dagger \hat{a}_{\boldsymbol{k}} \right] \tag{2.8}$$

where

$$\frac{1}{N} \sum_i e^{\pm i\left(\boldsymbol{k}-\boldsymbol{k}'\right)\cdot\boldsymbol{r}_i} = \delta_{\boldsymbol{k}\boldsymbol{k}'} \tag{2.9}$$

Hence, Eq. (2.8) may be rewritten as

$$
\begin{aligned}
\hat{H} &= -t \sum_{\boldsymbol{\delta}} \sum_{\boldsymbol{k}} \left[ e^{i\boldsymbol{k}\cdot\boldsymbol{\delta}} \hat{a}_{\boldsymbol{k}}^{\dagger} \hat{b}_{\boldsymbol{k}} + e^{-i\boldsymbol{k}\cdot\boldsymbol{\delta}} \hat{b}_{\boldsymbol{k}}^{\dagger} \hat{a}_{\boldsymbol{k}} \right] \\
&= \sum_{\boldsymbol{k}} \left[ \begin{pmatrix} \hat{a}_{\boldsymbol{k}}^{\dagger} & \hat{b}_{\boldsymbol{k}}^{\dagger} \end{pmatrix} \begin{pmatrix} 0 & -t\sum_{\boldsymbol{\delta}} e^{i\boldsymbol{k}\cdot\boldsymbol{\delta}} \\ -t\sum_{\boldsymbol{\delta}} e^{-i\boldsymbol{k}\cdot\boldsymbol{\delta}} & 0 \end{pmatrix} \begin{pmatrix} \hat{a}_{\boldsymbol{k}} \\ \hat{b}_{\boldsymbol{k}} \end{pmatrix} \right] \\
&= \sum_{\boldsymbol{k}} \boldsymbol{\Psi}_{\boldsymbol{k}}^{\dagger} \hat{H}_{\boldsymbol{k}} \boldsymbol{\Psi}_{\boldsymbol{k}}
\end{aligned}
\tag{2.10}
$$

where $\hat{H}_{\boldsymbol{k}}$ is the Hamiltonian in the $\boldsymbol{k}$-representation which may be written as [40]

$$
\hat{H}_{\boldsymbol{k}} = -t \begin{pmatrix} 0 & f_{\boldsymbol{k}} \\ f_{\boldsymbol{k}}^{*} & 0 \end{pmatrix}, \quad f_{\boldsymbol{k}} = \sum_{\boldsymbol{\delta}} e^{i\boldsymbol{k}\cdot\boldsymbol{\delta}}
\tag{2.11}
$$

Hence, the energy eigenvalues of $\hat{H}_{\boldsymbol{k}}$ are

$$
E_{\pm} = \pm t |f_{\boldsymbol{k}}|
\tag{2.12}
$$

plugging in Eq. (2.5) for $|f_{\boldsymbol{k}}|$, we get

$$
\begin{aligned}
|f_{\boldsymbol{k}}| &= \sqrt{f_{\boldsymbol{k}} f_{\boldsymbol{k}}^{*}} \\
&= \sqrt{\left( \sum_{m}^{3} e^{i\boldsymbol{k}\cdot\boldsymbol{\delta}_m} \right) \left( \sum_{n}^{3} e^{-i\boldsymbol{k}\cdot\boldsymbol{\delta}_n} \right)} \\
&= \sqrt{\sum_{m}^{3} \sum_{n}^{3} e^{i\boldsymbol{k}\cdot(\boldsymbol{\delta}_m - \boldsymbol{\delta}_n)}} \\
&= \sqrt{3 + 2\cos\left(\sqrt{3}k_y a\right) + 4\cos\left(\frac{3}{2}k_x a\right)\cos\left(\frac{\sqrt{3}}{2}k_y a\right)} \\
&= \sqrt{1 + 4\cos\left(\frac{3}{2}k_x a\right)\cos\left(\frac{\sqrt{3}}{2}k_y a\right) + 4\cos^2\left(\frac{\sqrt{3}}{2}k_y a\right)}
\end{aligned}
\tag{2.13}
$$

Hence, the $E$-$k$ dispersion relationship of graphene may be written as [39, 40]

$$
E_{\pm}(\boldsymbol{k}) = \pm t \sqrt{1 + 4\cos\left(\frac{3}{2}k_x a\right)\cos\left(\frac{\sqrt{3}}{2}k_y a\right) + 4\cos^2\left(\frac{\sqrt{3}}{2}k_y a\right)}
\tag{2.14}
$$

where the plus and minus signs correspond to the conduction band ($\pi^*$) and the valence band ($\pi$), respectively. This energy dispersion relationship is plotted in Figs. 2.2**a&b**. Now

we look into the nature of the energy dispersion close to the Dirac points, $\boldsymbol{K}$ and $\boldsymbol{K'}$

$$\boldsymbol{K} = \frac{2\pi}{3\sqrt{3}a}\left(\sqrt{3}, 1\right), \quad \boldsymbol{K'} = \frac{2\pi}{3\sqrt{3}a}\left(\sqrt{3}, -1\right) \tag{2.15}$$

as the experimentally accessible energy level is limited to within $\sim \pm 0.5$ eV which is near the Dirac points. We will discuss about this accessible energy level later. It is convenient to define the relative wave vector around the Dirac points $\boldsymbol{K}$ and $\boldsymbol{K'}$ as

$$\boldsymbol{q} \equiv \boldsymbol{k} - \boldsymbol{K} \text{ (or } \boldsymbol{K'}\text{)}, \quad |\boldsymbol{q}| \ll |\boldsymbol{K}| \text{ (or } |\boldsymbol{K'}|\text{)} \tag{2.16}$$

Now $f_{\boldsymbol{k}}$ may be rewritten in terms of $\boldsymbol{q}$ as

$$\begin{aligned}
f_{\boldsymbol{k}} &= \sum_{\boldsymbol{\delta}} e^{i\boldsymbol{k}\cdot\boldsymbol{\delta}} \\
&= e^{-ik_x a}\left[1 + 2e^{i3k_x a/2}\cos\left(\frac{\sqrt{3}ak_y}{2}\right)\right] \\
\Rightarrow f_{\boldsymbol{K}+\boldsymbol{q}} &= e^{-iK_x a}e^{-iq_x a}\left[1 - 2e^{i3q_x a/2}\left\{\frac{1}{2}\cos\left(\frac{\sqrt{3}}{2}q_y a\right) - \frac{\sqrt{3}}{2}\sin\left(\frac{\sqrt{3}}{2}q_y a\right)\right\}\right] \\
&\approx e^{-iK_x a}\left(1 - iq_x a\right)\left[1 - 2\left(1 + i\frac{3}{2}q_x a\right)\left(\frac{1}{2} - \frac{3}{4}q_y a\right)\right] \\
&\approx -i\frac{3}{2}ae^{-iK_x a}\left(q_x + iq_y\right)
\end{aligned} \tag{2.17}$$

From the third line to the fourth line, Maclaurin series expansion was used. Since the global phase factor, $ie^{-iK_x a}$, does not have significant physical meaning, $f_{\boldsymbol{K}+\boldsymbol{q}}$ may be simplified as

$$f_{\boldsymbol{K}+\boldsymbol{q}} = -\frac{3a}{2}\left(q_x + iq_y\right) \tag{2.18}$$

Hence, near the Dirac point $\boldsymbol{K}$, the Hamiltonian in terms of $\boldsymbol{q}$ may be written as [39, 41]

$$\begin{aligned}
\hat{H}_{\boldsymbol{K}+\boldsymbol{q}} &= \frac{3at}{2}\begin{pmatrix} 0 & q_x + iq_y \\ q_x - iq_y & 0 \end{pmatrix} \\
&= \hbar v_F \begin{pmatrix} 0 & q_x + iq_y \\ q_x - iq_y & 0 \end{pmatrix} \\
&= \hbar v_F \left[q_x \begin{pmatrix} 0 & 1 \\ 1 & 0 \end{pmatrix} + q_y \begin{pmatrix} 0 & +i \\ -i & 0 \end{pmatrix}\right] \\
&= \hbar v_F \bar{\boldsymbol{\sigma}} \cdot \boldsymbol{q}
\end{aligned} \tag{2.19}$$

where the Fermi velocity of electron $v_F \equiv 3at/2\hbar \approx 10^6$ m/s which is about 300 times smaller than the speed of light, $\hbar \approx 6.582 \times 10^{-16}$ eV·s/rad is Planck's constant (divided by $2\pi$),
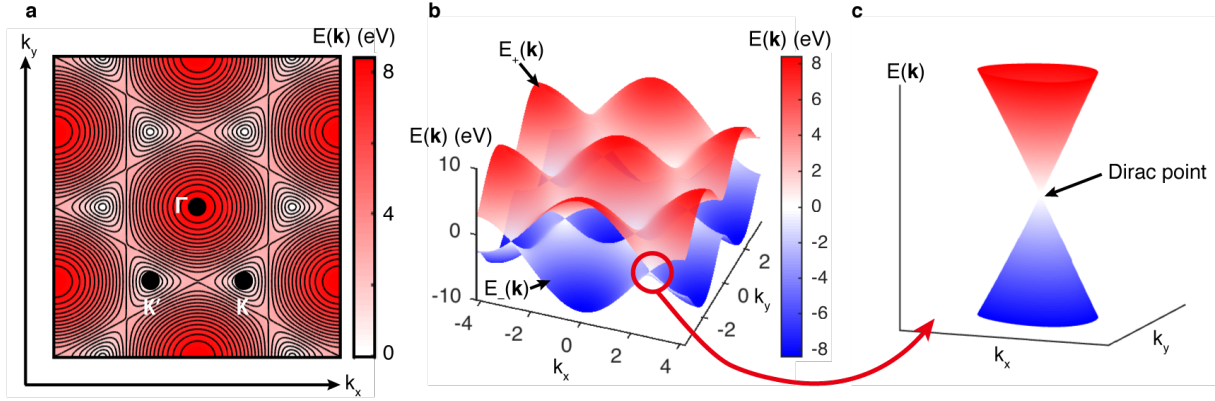
Figure 2.2: Energy dispersion relationship $E(\boldsymbol{k})$ of graphene. **a**: Top view of the energy dispersion $E(\boldsymbol{k})$ with contours. **b**: Energy dispersion $E(\boldsymbol{k})$. **c**: Linear energy dispersion $E(\boldsymbol{k})$ near $\boldsymbol{K}$ (Dirac point).

and $\bar{\boldsymbol{\sigma}}$ is the complex conjugate of Pauli vector, $\boldsymbol{\sigma} = (\sigma_x, \sigma_y, \sigma_z)$. Similarly, near the Dirac point $\boldsymbol{K}'$ [39, 41]

$$\hat{H}_{\boldsymbol{K}'+\boldsymbol{q}} = \hbar v_F \boldsymbol{\sigma} \cdot \boldsymbol{q} \tag{2.20}$$

Hence, for both Dirac points $\boldsymbol{K}$ and $\boldsymbol{K}'$, the energy eigenvalues of $\hat{H}_{\boldsymbol{K}+\boldsymbol{q}}$ ($\hat{H}_{\boldsymbol{K}'+\boldsymbol{q}}$) may be written as

$$E_{\pm}(\boldsymbol{q}) = \pm \hbar v_F |\boldsymbol{q}|, \quad |\boldsymbol{q}| \ll |\boldsymbol{K}| \, (\text{or } |\boldsymbol{K}'|) \tag{2.21}$$

This linear conical energy dispersion (Fig. 2.2**c**), *Dirac cone*, makes the electrical properties of graphene unique. In this linear energy dispersion, the velocity of electrons $v_F$ is independent of the momentum and the energy. In general, massive particles (e.g. electrons) have parabolic energy dispersions given by $E(p) = p^2/(2m^*) = \hbar^2 k^2/(2m^*)$, where $m^*$ is an effective mass, as plotted in Fig. 2.3**a**. On the other hand, for relativistic particles, the energy-momentum relation, $E(p) = \sqrt{(cp)^2 + (m_0 c^2)^2}$ [42], where $c$ is the speed of light, becomes linear in the limit of zero rest mass

$$\lim_{m_0 \to 0} E(p) = c|p| (= \hbar c |k|) \tag{2.22}$$

as shown in Fig. 2.3**b**. It is clear that Eq. (2.21) can be obtained by replacing the speed of light $c$ in Eq. (2.22) by the Fermi velocity of the electrons in graphene $v_F$. These theoretical considerations indicate that the electrons in graphene at the low energy regime near the Dirac points are massless and quasi-relativistic particles with the Fermi velocity $v_F$. Therefore, the electron dynamics in graphene is described by the Dirac equation, rather than the Schrödinger equation. Hence, the electrons near the Dirac points in graphene are called *massless Dirac fermions*. Indeed, this unusual electron transport in graphene was experimentally validated by observing that the electrons in graphene can propagate without scattering over large distances in the order of micrometers [18]. The mobility $\mu$ has

**a**

**b**
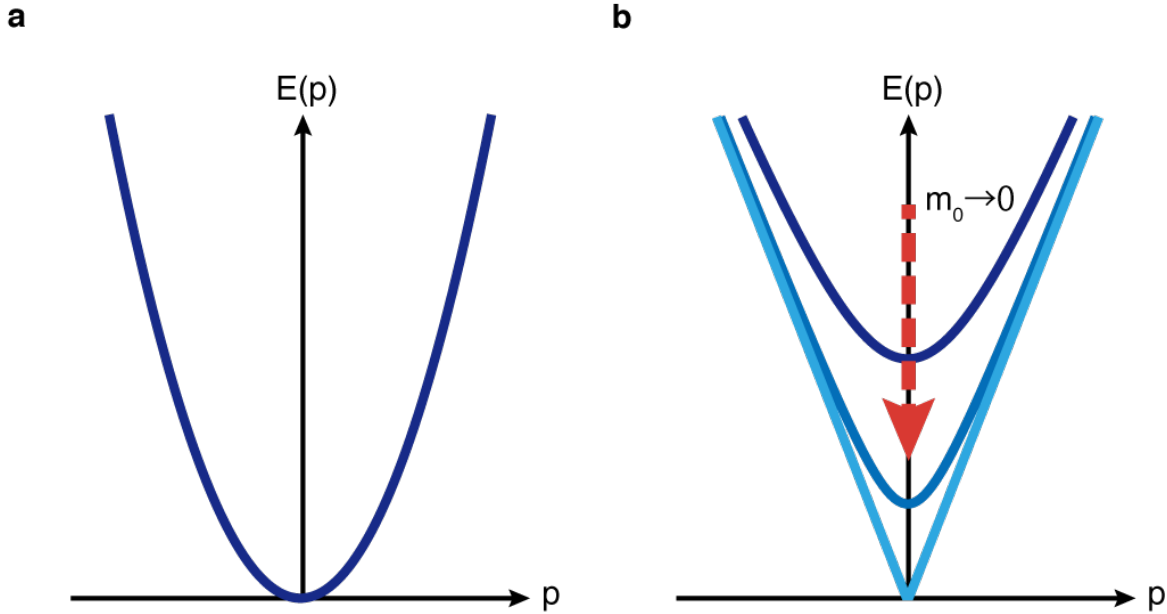


Figure 2.3: Energy-momentum relations. **a**: Energy-momentum relation for classical motion given by $E(p) = p^2/(2m^*) = \hbar^2 k^2/(2m^*)$. **b**: Energy-momentum relation for relativistic motion given by $E(p) = \sqrt{(cp)^2 + (m_0 c^2)^2}$ approaches linear relation as $\lim_{m_0 \to 0}$.

been observed up to 15,000 cm$^2$/(V·s) even under ambient conditions, which is much higher than other commonly used conductors and semiconductors: Cu (32 cm$^2$/(V·s)), Si (1,400 cm$^2$/(V·s)), Ge (3,900 cm$^2$/(V·s)), and GaAs (8,500 cm$^2$/(V·s)), all for electrons [18, 19, 41, 43]. In addition to the quasi-relativistic property, graphene exhibits ambipolar electric field effect, i.e., both electrons and holes can be majority carrier across the Dirac points where the conduction band and the valence band touch each other. The density of states $D(E)$ near the Dirac points may be derived from the number of states $N(k)$ as follows [39, 41]

$$N(k)dk = N(E)dE = \frac{A2\pi k dk}{(2\pi)^2} \times 2 \times 2$$

$$\Rightarrow N(E) = \frac{A2}{\pi} \frac{k dk}{dE}$$

$$= \frac{A2}{\pi} \frac{|E|}{(\hbar v_F)^2} \tag{2.23}$$

$$\Rightarrow \frac{N(E)}{A} = D(E) = \frac{2|E|}{\pi \hbar^2 v_F^2}, \quad |E| \ll |t|$$

where $A$ is the primitive cell area given by $A = 3\sqrt{3}a^2/2$. The factors in the first line take into account the degeneracy due to the electron spins and the non-equivalent points $\boldsymbol{K}$ and

$\boldsymbol{K'}$. Hence, the density of states should be linearly proportional to the energy level near the Dirac points. Aforementioned electrical properties are readily examined by graphene field effect transistor (FET) structure. The fundamentals of graphene FET are introduced in the following section.

## 2.3  Graphene FET

Graphene FET is a powerful platform to characterize the electrical properties of graphene described in the previous section. From an engineering perspective, the truly 2-dimensional structure of graphene is suitable for MEMS fabrication processes. Therefore, graphene FETs can be readily fabricated in micrometer scale with cost efficient batch processes. In addition, graphene can be integrated with complementary metal oxide semiconductors (CMOS) circuits as an alternative for silicon [44]. In this section, a typical graphene FET device structure, the fabrication process, and the fundamental properties are described.

### 2.3.1  Device structure and fabrication process

Figure 2.4 illustrates a typical graphene FET structure which consists of graphene, gate oxide, back gate (G), source (S), drain (D), and inner electrodes (A, B, A', B'), where A' and B' can be used for the Hall measurement or as spare inner electrodes. In general, a constant current, $I_{SD}$, is supplied between the source and the drain, and a voltage across the two inner electrodes, $V_{AB}$, is measured. The gate voltage, $V_G$, may be applied if required. One of the graphene FET designs used in this dissertation is shown in Fig. 2.5 with the specific dimensions (Figs. 2.5**a&b**) and the actual photomask images (Figs. 2.5**c&d**).

In this dissertation, the same device fabrication process is used for pristine graphene FETs described as follows: Commercially available graphene wafers (monolayer graphene on $SiO_2$/Si (300 nm/500 $\mu$m), 10 mm × 10 mm in area, Graphenea) via chemical vapor deposition (CVD) are used as the starting wafer (Fig. 2.6**a**). The metal contacts, Au/Pd (50 nm/25 nm) are patterned on the graphene wafer by a lift-off process (Figs. 2.6**b-d**). Afterwards, the graphene channels (e.g., 100 $\mu$m in width and 500 $\mu$m in length) are defined by an oxygen plasma etching process with the 50 W RF power for 7-10 s (Figs. 2.6**e-g**). Figure 2.7 shows microscope images of the representative fabrication steps: **a** Au/Pd (50 nm/25 nm) deposited on the entire wafer; **b** Metal contacts formed via a lift-off process; **c** Photoresist etching mask for an oxygen plasma etching process; and **d** Defined graphene channel. The fabricated devices are generally strongly p-type doped (the majority carriers are hole). The major factors contributing to this p-type doping effect are considered to be the impurities such as poly(methyl methacrylate) and $H_2O$ which may be introduced in the graphene transfer process [45]. When a device is strongly p-type doped, the charge neutrality point of the graphene FET may not be measured as it is outside of the gate voltage window. In order to solve this issue, polyethylenimine (PEI) has been often used as an n-type counter doping material for nanomaterials [46, 47]. In this study, ~20 wt% polyethylenimine (PEI)

solution was applied to the graphene and left for two hours for the n-type counter doping process (Fig. 2.8). The PEI solution was then washed away by soaking in DI water and the charge neutrality point was shifted to within $\pm 10$ V gate voltage.

## 2.3.2 Fundamentals of graphene FET

As mentioned earlier, graphene FETs fabricated via photolithography process are generally p-type doped (the majority carriers are hole), i.e., the Fermi level $E_F$ is lower than the Dirac points (so it is within the valence band). The initial carrier concentration is estimated to be [48]

$$n_0 = \frac{c_g}{e}V_{NP} \tag{2.24}$$

where $c_g$ is the gate capacitance per unit area given by $c_g = \varepsilon_0 \varepsilon_{SiO_2}/t_{ox} \approx 1.15 \times 10^{-8}$ C/(V· cm$^2$) (where $\varepsilon_0 = 8.854 \times 10^{-14}$ C/(V· cm), $\varepsilon_{SiO_2} = 3.9$, $t_{ox} = 3 \times 10^{-5}$ cm), $e$ is the elementary charge, $1.602 \times 10^{-19}$ C, $V_{NP}$ is the gate voltage at the charge neutrality point (NP) where the conductivity $\sigma$ $1/\Omega$ becomes its minimum value $\sigma = \sigma_0$. The carrier concentration of graphene FET can be modulated by applying the gate voltage $V_G$ [48]

$$n_{e/h}(V_G) = \begin{cases} \frac{c_g}{e}(V_G - V_{NP}) & \text{for } V_G > V_{NP} \text{ electron branch} \\ \frac{c_g}{e}(V_{NP} - V_G) & \text{for } V_G < V_{NP} \text{ hole branch} \\ 0 & \text{for } V_G = V_{NP} \end{cases} \tag{2.25}$$
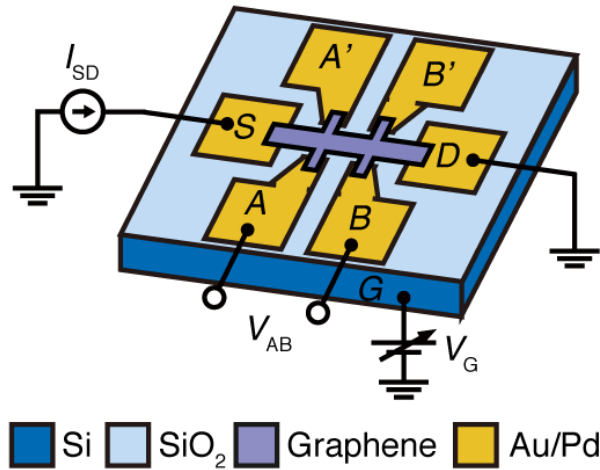


Figure 2.4: Schematic of a graphene FET and its electrical configuration. An electrical current is supplied between S and D. The voltage across A and B is measured. A' and B' may be used for the Hall measurement or as spare inner electrodes.
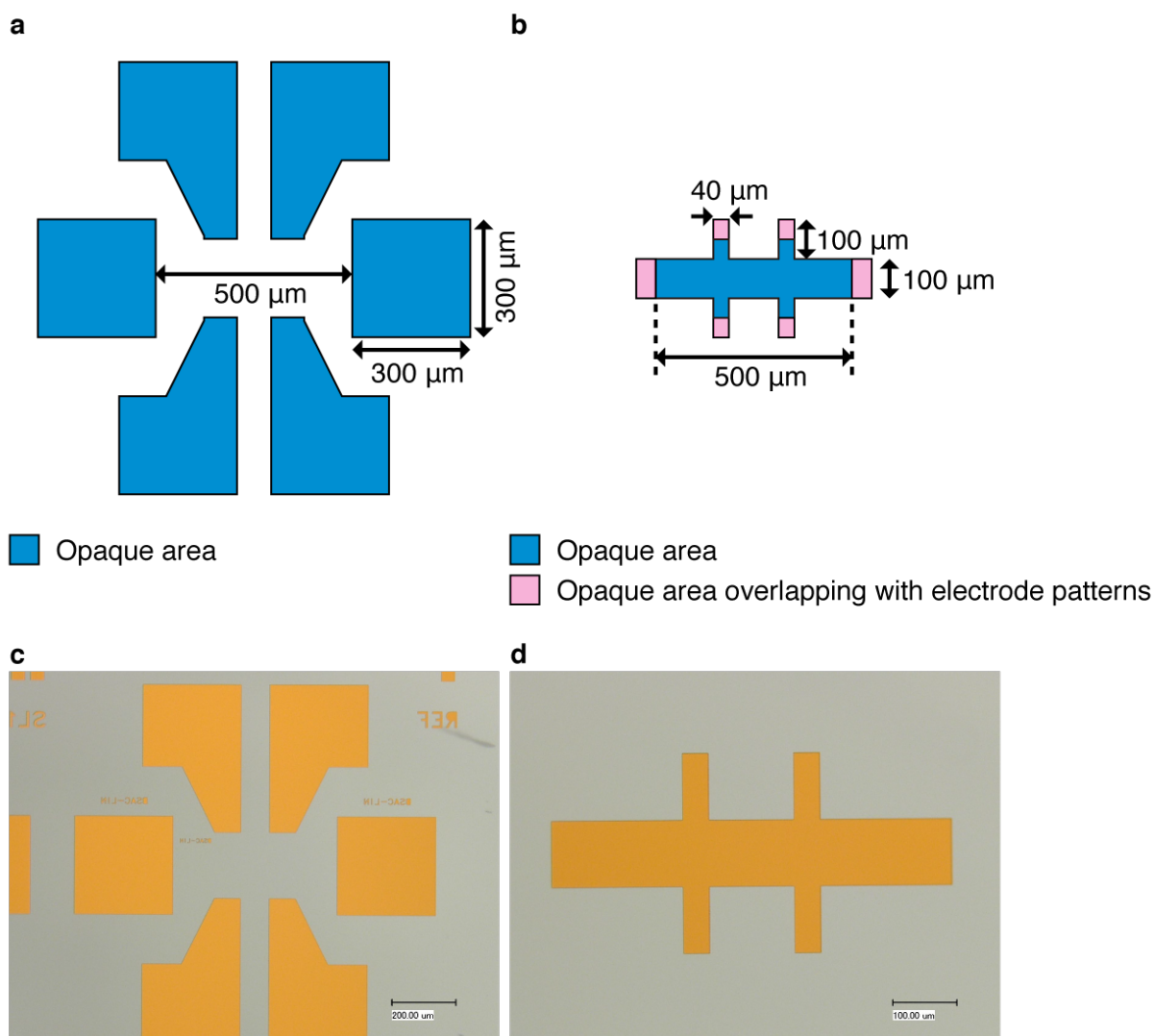
Figure 2.5: Design of graphene FET and microscope images of the photomasks. **a**: Electrode design. **b**: Graphene channel design. The pink color areas overlap with the electrode patterns. **c**: Microscope image of the photomask for the electrodes. **d**: Microscope image of the photomask for the graphene channel.
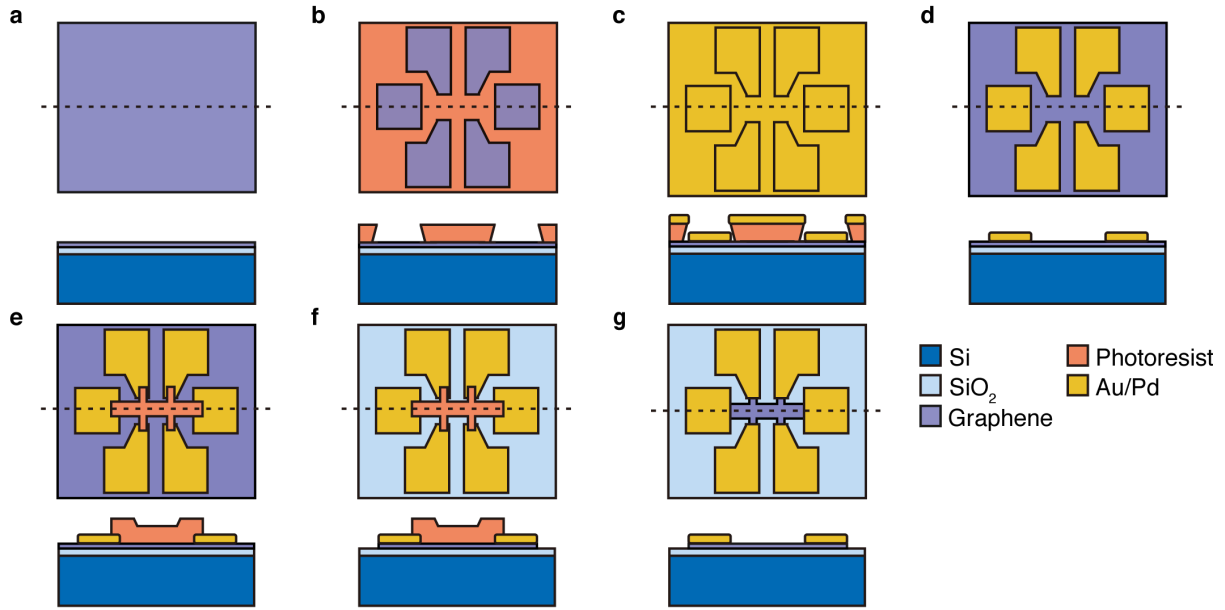
Figure 2.6: Schematic of the fabrication process of graphene FET. **a**: A pre-transferred monolayer graphene on a $SiO_2/Si$ (300 nm/500 $\mu$m) wafer. **b**: Photoresist patterning for metal contact pads. **c**: Au/Pd (50 nm/25 nm) deposition. **d**: Metal contact pads are patterned by a lift-off process. **e**: Photoresist patterning for graphene channel. **f**: The graphene layer is patterned by oxygen plasma etching. **g**: Removal of the photoresist.

Hence, the conductivity profile versus the gate voltage $\sigma(V_G)$ may be written as [48]

$$\sigma_{e/h}(V_G) = n_{e/h}(V_G)e\mu_{e/h} + \sigma_0 \tag{2.26}$$

where $\mu_{e/h}$ is the carrier mobility. The carrier concentration can be expressed in another way [41]

$$
\begin{aligned}
n_{e/h} &= \frac{N}{A} \\
&= \frac{\pi k_F^2}{(2\pi)^2} \times 2 \times 2 \\
&= \frac{k_F^2}{\pi} \\
&= \frac{E_F^2}{\pi\hbar^2 v_F^2}
\end{aligned}
\tag{2.27}
$$

Hence, together with Eq. (2.25), the Fermi level $E_F$ may be written as a function of the gate voltage $V_G - V_{NP}$

$$E_F(V_G - V_{NP}) = \pm\alpha\sqrt{|V_G - V_{NP}|}, \quad \alpha \equiv \hbar v_F\sqrt{\frac{\pi c_g}{e}} \tag{2.28}$$
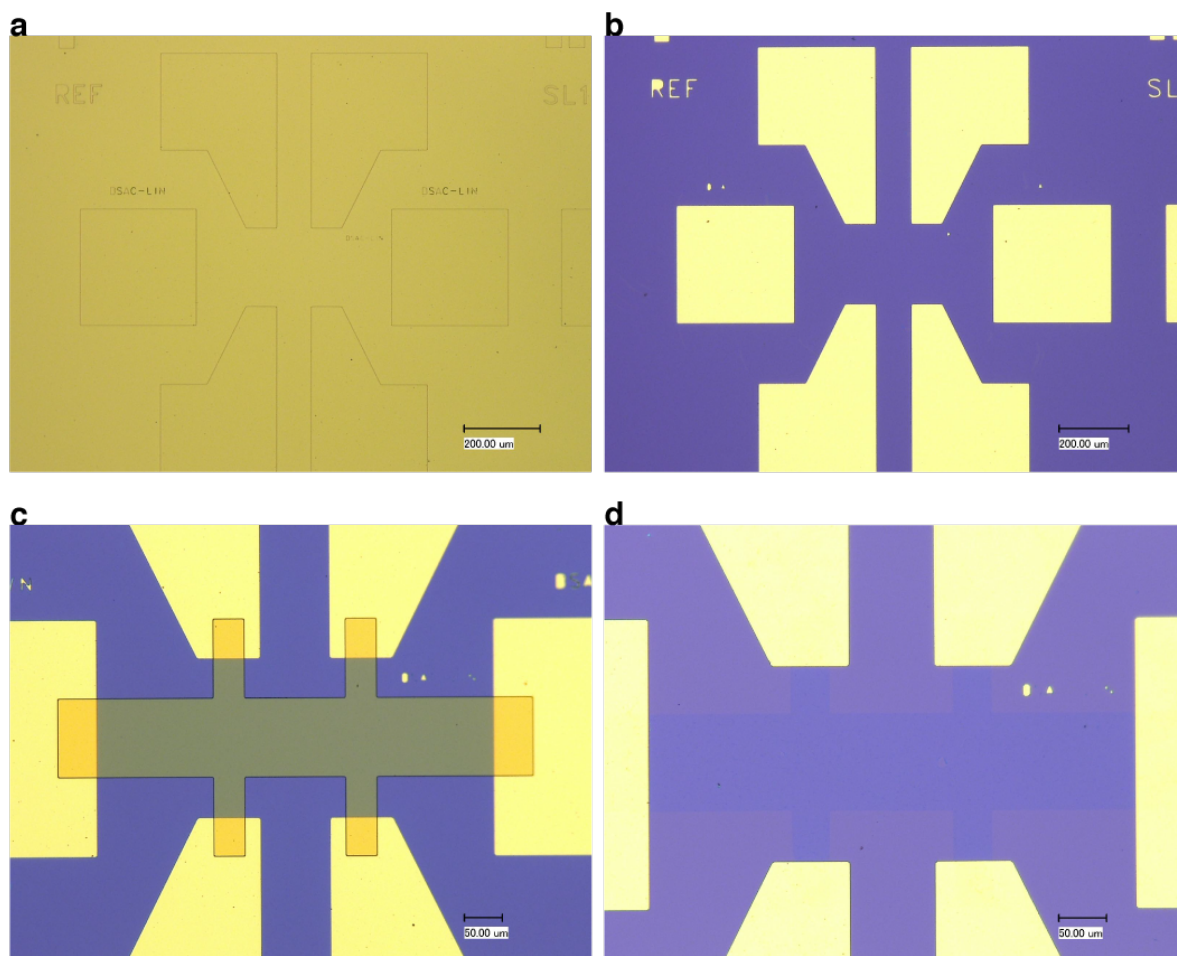
Figure 2.7: Microscope images of the representative fabrication steps. **a**: Au/Pd (50 nm/25 nm) deposited on the entire wafer. **b**: Metal contacts formed via a lift-off process. **c**: Photoresist etching mask for an oxygen plasma etching process. **d**: Defined graphene channel.



Figure 2.8: Photographic image of n-type counter doping by PEI solution.
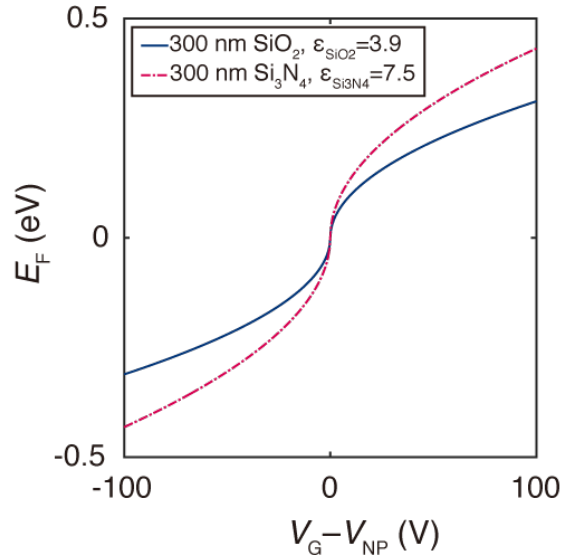
Figure 2.9: Fermi level $E_F$ as a function of the gate voltage $V_G - V_{NP}$.

where the minus sign applies to the negative gate voltage $V_G - V_{NP} < 0$. As shown in Fig. 2.9, the Fermi level $E_F$ does not reach $\pm 0.5$ eV even under $\pm 100$ V of the gate voltage. In order to enlarge the accessible $E_F$ level, either larger dielectric constant $\varepsilon_r$ or thinner gate oxide thickness $t_{ox}$ is required. Due to the fact that a too large gate voltage is not convenient for practical applications, the accessible $E_F$ is roughly limited to within $\pm 0.5$ eV as mentioned earlier.

A typical conductivity profile of graphene FET is shown in Fig. 2.10**a**. One of the possible reasons for the non-zero minimum conductivity at the charge neutrality point is the existence of residual carriers which may form inhomogeneous charged puddles due to non-uniformly distributed charged impurities as illustrated in Fig. 2.10**b**. In fact, it has been reported that the electrical transport of graphene can be explained well by scattering from charged impurities [48, 49]. Different scattering mechanisms may be predominant depending on the carrier concentration which determines the strength of the screening effect. At low carrier concentration regime where the screening effect is weak, i.e. near the Dirac point, the electrical transport is dominated by Coulomb scattering. On the other hand, at high carrier concentration regime where the screening effect is strong, the electrical transport is dominated by short range scattering. The electrical conductivity and the mobility in terms
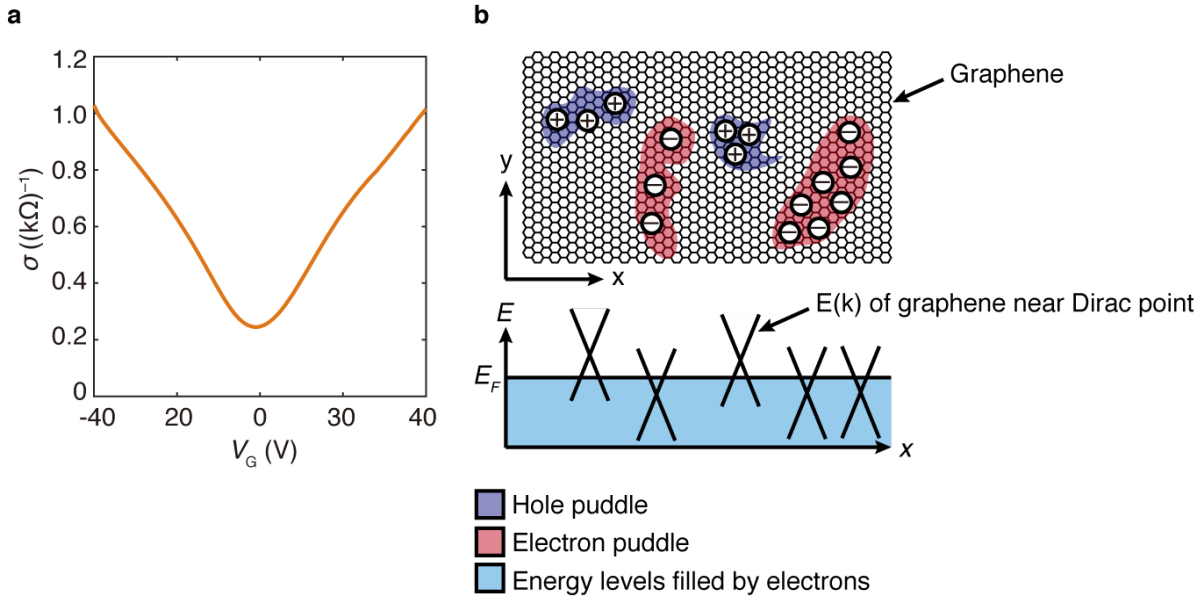
Figure 2.10: **a**: Typical conductivity profile of graphene FET. **b**: Schematic of inhomogeneous charged puddles and the corresponding energy band diagram.

of the charged impurities concentration may be written as [49]

$$\sigma(n - \bar{n}) = \begin{cases} \dfrac{20e^2}{h} \dfrac{n^*}{n_{imp}} & \text{for } n - \bar{n} < n^* \\[2mm] \dfrac{20e^2}{h} \dfrac{n}{n_{imp}} & \text{for } n - \bar{n} > n^* \end{cases} \tag{2.29}$$

$$\frac{\mu}{\mu_0} \approx 50 \frac{n_0}{n_{imp}} \tag{2.30}$$

where $\bar{n}$ is the average concentration of the inhomogeneous carriers given by $\bar{n} = n_{imp}^2/(4n^*)$, $h$ is Planck constant given by $h = 4.135 \times 10^{-15}$ eV·s, $n^*$ is the residual carrier concentration, $n_{imp}$ is the charged impurities concentration, $\mu_0 = 10^4$ cm$^2$/(V·s), and $n_0 = 10^{10}$ 1/cm$^2$ [49]. Equations (2.29) and (2.30) indicate that the conductivity $\sigma(n - \bar{n})$ is linearly proportional to the carrier concentration and the mobility $\mu$ is constant, respectively.

As described above, the electrical properties of graphene FET is modulated not only by the gate voltage (active doping), but also by the charged impurities (passive doping). In the ambient conditions, environmental factors such as temperature, humidity, and chemical species can also affect the electrical properties. The influence of the environmental factors will be discussed in Chapter 3.

## 2.4 Graphene as a Chemical-to-Electrical Transducer

Graphene can serve as a chemical-to-electrical transducer. In order for chemical information being converted into electrical signals, the analytes must interact with the transducer. When graphene FETs are used as gas sensors, the interactions between gas molecules and graphene can be divided into three major phenomena: (1) gas adsorption and desorption, (2) charge transfer between gas molecules and graphene, and (3) electron-charged impurity scattering. Therefore, in this section, these three phenomena are reviewed.

### 2.4.1 Gas adsorption

When gas molecules come into contact with a surface of solids, both attractive force and repulsive force are applied between them depending on the distance. The interaction via the attractive force is called the van der Waals interaction (also called the London interaction). The van der Waals interaction is weaker compared with other intermolecular forces such as hydrogen bonding and ionic bonding. The origins of the attractive force include instantaneous dipoles, permanent dipoles, and induced dipoles, i.e., non-uniformly distributed charges in space, of molecules or atoms. The repulsive force is mainly due to the Pauli exclusion principle which states that two electrons cannot have all the same quantum numbers. The total potential energy due to the van der Waals interaction and the Pauli exclusion principle can be represented by the Lennard-Jones potential [50]

$$U(r) = 4\varepsilon \left[ \left( \frac{r_0}{r} \right)^{12} - \left( \frac{r_0}{r} \right)^{6} \right] \tag{2.31}$$

where $r$ is the distance between gas molecules and a surface of a solid in this case, $\varepsilon$ is the depth of the well, and $r_0$ is the distance at which $U = 0$. As shown in Fig. 2.11**a**, the long range attractive force (the van der Waals force) is first applied between the gas molecules and the surface of the solid, and then the short range repulsive force (due to the Pauli exclusion principle) is applied. As a result, the gas molecules with lower thermal energies will eventually reach the equilibrium distance $r_e = 2^{1/6} r_0$. Gas adsorption due to the weak, long range van der Waals interaction is called physisorption (an abbreviation of physical adsorption). The typical enthalpy change associated with physisorption is about $\Delta H = -20$ kJ/mol. On the other hand, gas molecules may stick to a surface by forming a strong chemical bond. In this case, the gas adsorption is called chemisorption (an abbreviation of chemical adsorption). The typical enthalpy change associated with chemisorption is about $\Delta H = -200$ kJ/mol, which is much larger than that of physisorption [50]. Figures 2.11**b&c** illustrate the potential energies for chemisorption including the precursor states (physisorption states). In the potential energy shown in Fig. 2.11**b**, the gas molecules my be transferred from the precursor (physisorption) state to the chemisorption state, after overcoming the small potential barrier. This chemisorption may happen without activation as the potential energy (barrier) between the precursor state and the chemisorption state is smaller than the energy faraway
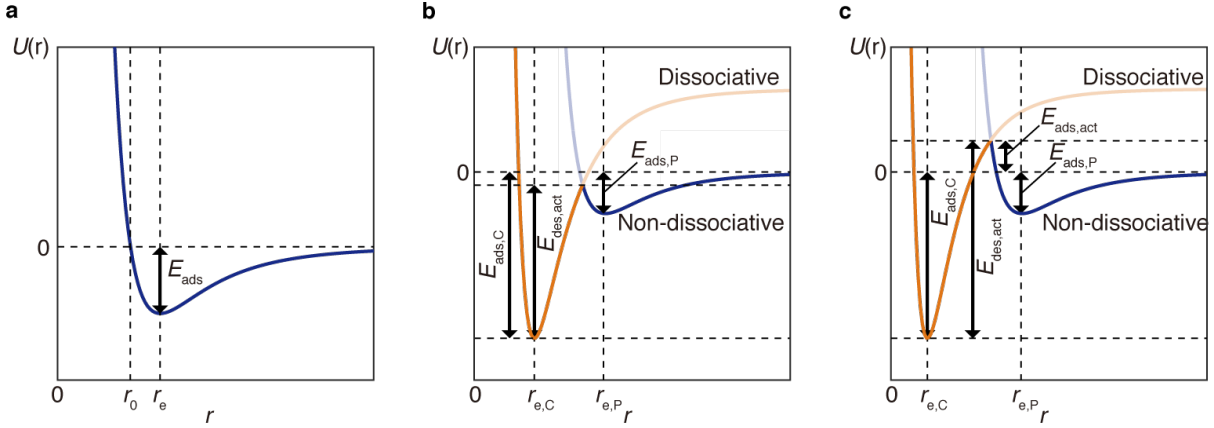
Figure 2.11: Potential energy of gas molecule on a surface of solid as a function of distance from the surface. **a**: The Lennard-Jones potential. **b**: Potential energy for non-activated adsorption. The orange and blue lines represent the potential energy for dissociative chemisorption and non-dissociative physisorption, respectively. $E_{ads,P}$ is the released energy associated with physisorption. $E_{ads,C}$ is the released energy associated with chemisorption. $E_{des,act}$ is the required energy for a gas molecule to be desorbed. $r_{e,P}$ is the equilibrium distance for physisorption. $r_{e,C}$ is the equilibrium distance for chemisorption. **c**: Potential energy for activated adsorption. The orange and blue lines represent the potential energy for dissociative chemisorption and non-dissociative physisorption, respectively. $E_{ads,P}$ is the released energy associated with physisorption. $E_{ads,C}$ is the released energy associated with chemisorption. $E_{ads,act}$ is the required energy for a gas molecule to be adsorbed. $E_{des,act}$ is the required energy for a gas molecule to be desorbed. $r_{e,P}$ is the equilibrium distance for physisorption. $r_{e,C}$ is the equilibrium distance for chemisorption.

from the surface. This type of adsorption is called non-activated chemisorption. On the other hand, in the potential energy shown in Fig. 2.11**c**, activation anergy $E_{act}$ is required to transfer the gas molecules from the precursor state to the chemisorption state. Hence, this type of adsorption is called activated chemisorption. The nature of gas adsorption may be physisorption-like or chemisorption-like depending on the gas molecules (adsorbate), the surface of solids (adsorbent), and the temperature. Specific cases with graphene FETs will be discussed in Chapter 3.

In general, gas sensors are expected to be capable of quantifying the gas concentration of specific target gases. For chemical resistor (chemiresistor) type gas sensors, the electrical signals are directly related to the surface coverage of target gases. Hence, the surface coverage must be expressed in terms of some physical quantities which can be converted to gas concentration. The gas concentration of specific gas $A$ may be expressed as

$$C_A = \frac{P_A}{P_{tot}} = \frac{V_A}{V_{tot}} \tag{2.32}$$

where $P_A$ is the partial pressure of gas $A$, $P_{tot}$ is the total pressure of gas mixture, $V_A$ is the partial volume of gas $A$, and $V_{tot}$ is the total volume of gas mixture. Therefore, either the partial pressure or the partial volume of target gases should be related to the surface coverage. Here, we derive the surface coverage of gas $A$ as a function of the partial pressure and temperature starting with the following assumptions for the sake of simplicity [50]:

- Adsorption cannot proceed beyond monolayer coverage.

- All adsorption sites are equivalent and the surface is uniform.

- There is no adsorbate-adsorbate interactions.

- Adsorbed molecules are immobile.

Under the dynamic equilibrium [50]

$$A(\text{gas}) + B(\text{surface}) \rightleftharpoons AB(\text{surface}) \tag{2.33}$$

The rate of change of surface coverage due to adsorption may be written as [50, 51]

$$\frac{d\theta}{dt} = k_{ads} P N (1 - \theta)$$

$$k_{ads} P = (\text{sticking probability})(\text{flux})(\text{probability to overcome energy barrier}) \tag{2.34}$$

$$= \frac{sP}{\sqrt{2\pi m k_B T}} \exp\left(-\frac{E_{ads,act}}{k_B T}\right)$$

where $\theta$ is the surface coverage, $k_{ads}$ is the rate constant for adsorption, $P$ is the pressure of gas $A$, $N$ is the total number of available adsorption sites, $s$ is the sticking probability, $m$ is the mass of the gas molecule, $k_B$ is the Boltzmann constant given by $k_B = 8.617 \times 10^{-5}$ eV/K, $T$ is the absolute temperature, and $E_{ads,act}$ is the required activation energy for the gas molecules to be adsorbed (if there are any energy barriers). As described above, $E_{ads,act}$ is zero for physisorption and non-activated chemisorption, i.e., the probability to overcome the energy barrier becomes 100% in those cases. The rate of change of surface coverage due to desorption may be written as [50]

$$\frac{d\theta}{dt} = -k_{des} N \theta$$

$$k_{des} = \nu \exp\left(-\frac{E_{des,act}}{k_B T}\right) \tag{2.35}$$

where $k_{des}$ is the rate constant for desorption, $\nu$ is the frequency of the vibration of the bonding between the gas molecules and the surface, and $E_{des,act}$ is the activation energy required for gas molecules to be desorbed. The net rate of change of surface coverage may

be expressed by using Eqs. (2.34) and (2.35)

$$\frac{d\theta}{dt} = k_{ads}PN(1-\theta) - k_{des}N\theta$$

$$\Rightarrow \frac{d\theta}{dt} + (k_{ads}P + k_{des})N\theta = k_{ads}PN \tag{2.36}$$

This is the first order inhomogeneous differential equation. Hence, the solution may be written as

$$\theta(t) = \frac{1}{u(t)}\left[\int u(t)k_{ads}PNdt + C_0\right] \tag{2.37}$$

where

$$u(t) \equiv \exp\left[\int \alpha dt\right]$$

$$\alpha \equiv k_{ads}P + k_{des} \tag{2.38}$$

Thus

$$\theta(t) = \frac{k_{ads}PN}{\alpha} + Ce^{-\alpha t} \tag{2.39}$$

By applying the initial condition $\theta(0) = 0$,

$$\theta(t) = \frac{k_{ads}PN}{k_{ads}P + k_{des}}\left[1 - \exp\{-(k_{ads}P + k_{des})t\}\right] \tag{2.40}$$

At equilibrium [50, 51]

$$\frac{d\theta}{dt}\bigg|_{t=0} = k_{ads}PN(1-\theta) - k_{des}N\theta = 0$$

$$\Rightarrow \theta = \frac{KP}{1+KP} \tag{2.41}$$

where

$$K \equiv \frac{k_{ads}}{k_{des}}$$

$$= \frac{s}{\nu}\frac{1}{\sqrt{2\pi m k_B T}}\exp\left(\frac{E_{des,act} - E_{ads,act}}{k_B T}\right) \tag{2.42}$$

Noting that larger $(E_{des,act} - E_{ads,act})/(k_B T)$ yields larger surface coverage, the magnitude of $K$ reflects how the bonding sticky is. Equation (2.41) is called the Langmuir isotherm. Figures 2.12**a&b** plot the Langmuir isotherm with different temperatures (**a**) and the isobar with different pressure (**b**). In the limit of $KP \ll 1$, Eq. (2.41) can be reduced to

$$\theta \approx KP, \quad KP \ll 1 \tag{2.43}$$

Hence, at thermal equilibrium, the surface coverage is linearly proportional to the pressure in this limit. Eq. (2.43) suggests that the electrical signals of chemiresistor type gas sensors can be linearly proportional to the partial pressure of the target gases in the following cases:
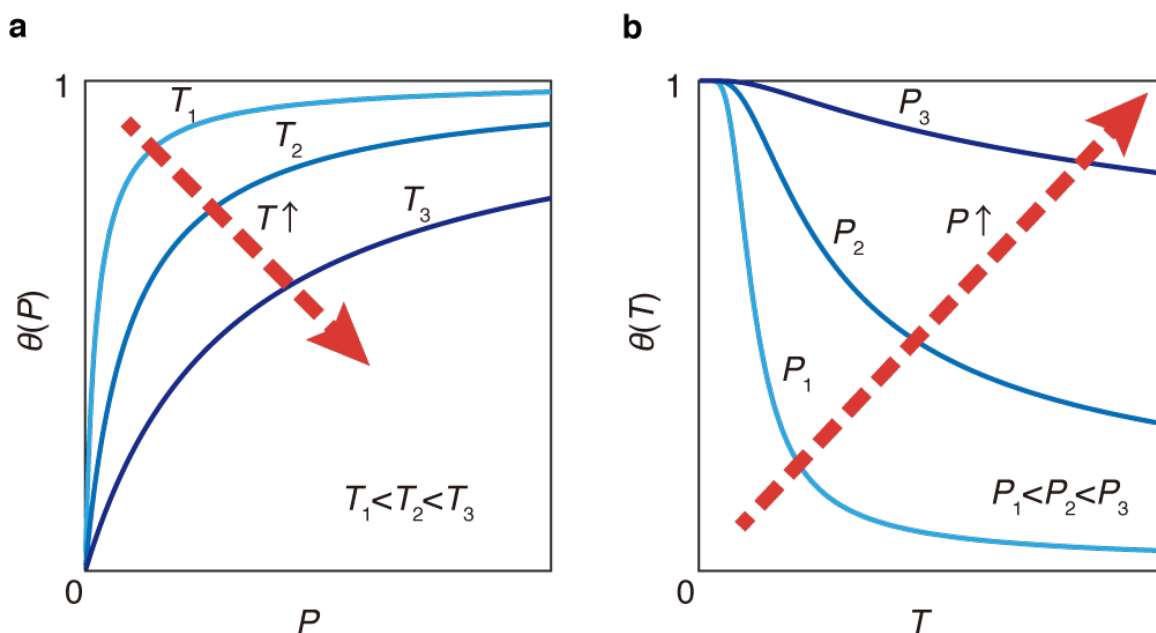
Figure 2.12: Langmuir isotherm and isobar. **a**: Langmuir isotherm with three different temperature in a relationship $T_1 < T_2 < T_3$. **b**: Langmuir isobar with three different pressure in a relationship $P_1 < P_2 < P_3$.

- $K$ is very small, i.e., the bonding strength between the gas molecules and the surface is very weak.

- The partial pressure $P$ of the target gas is very small, i.e., the gas concentration is very low.

- When both of the above conditions are satisfied.

The second condition may be satisfied for most of the realistic gas sensing scenarios as the typical target gas concentration range is in the order of ppm (parts-per-million).

In summary, the nature of gas adsorption may be physisorption-like or chemisorption-like depending on the gas molecules (adsorbate), the surface of solids (adsorbent), and the temperature. For chemiresistor type gas sensors, the gas concentration can be estimated via the surface coverage of a target gas. The surface coverage is a function of both pressure and temperature. Under the limiting cases, the surface coverage is linearly proportional to the gas concentration.
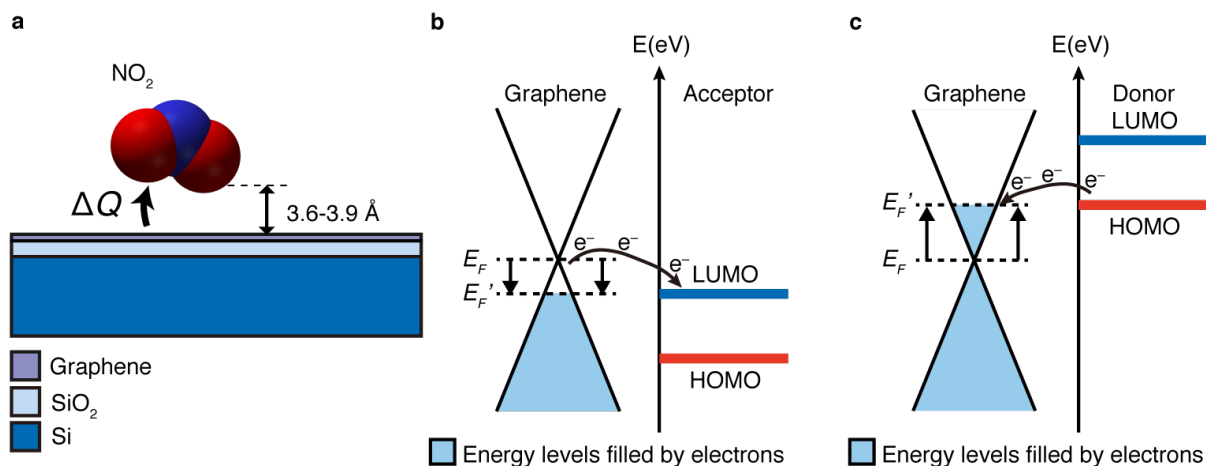
Figure 2.13: Schematic of charge transfer and the electron energy band diagram of graphene and gas molecules. **a**: Schematic of charge transfer between graphene and a gas molecule ($NO_2$ as example). The distance between the $NO_2$ molecule and the graphene is calculated to be $3.6 \sim 3.9$ Å. **b**: The electron energy band diagram of graphene and acceptor-type gas molecule. The initial Fermi level $E_F$ is higher than the LUMO of the gas molecule. Hence, the electrons transfer from graphene to the gas molecule. **c**: The electron energy band diagram of graphene and donor-type gas molecule. The initial Fermi level $E_F$ is lower than the HOMO of the gas molecule. Hence, the electrons transfer from the gas molecule to graphene.

## 2.4.2 Charge transfer

After gas molecules are adsorbed on the surface of graphene, charge transfer may occur between the gas molecules and the graphene. Figure 2.13 illustrates the schematic of charge transfer (**a**) and the electron energy band diagram of graphene and gas molecules (**b&c**). Previous studies have suggested that there are two major charge transfer mechanisms [52–54]:

    (i) Due to the relative position in the DOS of the highest occupied molecular orbital (HOMO) and the lowest unoccupied molecular orbital (LUMO) of the gas molecules.

    (ii) Hybridization of HOMO and LUMO of gas molecules with the graphene orbitals.

In the first mechanism, if the LUMO of the gas molecule is lower than the Fermi level of the graphene, charge will transfer from the graphene to the gas molecule, i.e., the gas molecule is acceptor and causes p-type doping (Fig. 2.13**b**). if the HOMO of the gas molecule is higher than the Fermi level of the graphene, charge will transfer from the gas molecule to the graphene, i.e., the gas molecule is donor and causes n-type doping (Fig. 2.13**c**). In the second mechanism, charge transfer can happen as a result of hybridization of the orbitals.

| Gases | Theory | Experiment | $E_{ads}$ (meV) | $\Delta Q(e)$ |
|-------|--------|-----------|-----------------|---------------|
| $H_2O$ | Acceptor | Acceptor | 47 | $-0.025$ |
| $NH_3$ | Donor | Donor | 31 | 0.027 |
| CO | Donor | Donor | 14 | 0.012 |
| $NO_2$ | Acceptor | Acceptor | 67 | $-0.099$ |

Table 2.1: Charge transfer of representative gas molecules [52]. The minus sign for $\Delta Q$ means charge transfer from graphene to gas molecules, i.e., p-type doping.

Because of the anisotropic distribution of HOMO and LUMO of gas molecules, the strength and the direction of charge transfer are dependent on the orientation of the gas molecules adsorbed on the surface. For example, $H_2O$ can be either donor or acceptor depending on the orientation. The overall doping effect of $H_2O$ on graphene is p-type doping as $H_2O$ becomes acceptor in the most energetically favored orientation. Table 2.1 summarizes the calculated adsorption energy and the charge transfer of representative gas molecules based on density functional theory (DFT) [52]. The minus sign for $\Delta Q$ means charge transfer from graphene to gas molecules, i.e., p-type doping. The theoretical predictions agree well with the experimental results previously reported. In addition to the two major charge transfer mechanisms mentioned above, another type of charge transfer may occur when $O_2$ and $H_2O$ coexist on the surface of graphene. It is believed that electrochemical redox reaction

$$O_2(aq) + 4H^+ + 4e^-(graphene) \rightleftharpoons 2H_2O \tag{2.44}$$
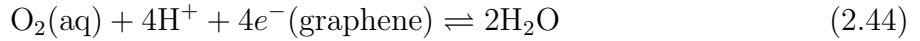
may initiate charge transfer due to the lowered free energy change given by $\Delta G = -0.7$ eV [55, 56].

After charge transfer, the Fermi level $E_F$ of graphene does not match with the Dirac point as shown in Figs. 2.13**b&c**. Therefore, the charge neutrality point will show up somewhere $V_G \neq 0$ in the conductivity profile of graphene FET. The amount of charge induced by gas molecules $\Delta n$ is readily estimated by [20]

$$\Delta n = \frac{c_g}{e} \Delta V_{NP} \tag{2.45}$$

where $\Delta V_{NP}$ is the change in the gate voltage at the charge neutrality point. Given the possible mechanisms of charge transfer, $\Delta n$ should be linearly proportional to the surface coverage, thereby gas concentration, when Eq. (2.43) is valid. Moreover, it is evident that the amount of charge transfer and the directions are different from gas to gas as shown in Table 2.1.

## 2.4.3 Charged impurity scattering

After charge transfer occurs between gas molecules and graphene, charged gas molecules (often called charged impurities) are left at the surface of graphene until they desorb. Previous studies have reported that the charged impurities significantly affect the carrier mobility

of graphene as a result of electron-charged impurity scattering [48, 57, 58]. It has been ubiquitously observed that the carrier mobility of graphene is inversely proportional to the charged impurities concentration, i.e., $\mu \propto 1/n_{imp}$, and so does the electrical conductivity, $\sigma \propto 1/n_{imp}$ as seen in Eq. (2.29) [48, 49, 57, 58]. In addition, as mentioned earlier, Eq. (2.29) suggests that the conductivity is linearly proportional to the carrier concentration, which has been widely observed experimentally. Although there is no unique parameter for electrons nor holes in Eq. (2.29), the conductivity profiles are generally asymmetric when charged impurities exist, i.e., the interactions between the electrons and the charged impurities may differ from that of holes and charged impurities [48, 58, 59]. In order to express the asymmetric conductivity, Eq. (2.29) may be rewritten as [48]

$$\sigma(n) = Ce\left|\frac{n}{n_{imp}}\right| + \sigma_0 \tag{2.46}$$

where $C$ is a constant which depends on carrier-charged impurity scattering, $\sigma_0$ is the minimum conductivity [48]. Previous study has suggested that the constant $C$ is expected to be asymmetry for attractive versus repulsive scattering, i.e., electron versus hole carriers, for Dirac fermions [48, 59]. At the low carrier density regime, i.e., near the charge neutrality point, long range charged impurity scattering (Coulomb scattering) becomes dominant scattering mechanism due to the weaker screening effect by the free carriers. Other scattering mechanisms in graphene include scattering due to short-range disorder and ripples. The dependence of the conductivity on carrier density associated with those scattering mechanisms is expected to be $\sigma \propto n^a$ with $a < 1$. When the conductivities associated with different scattering mechanisms are added in inverse following Matthiessen's rule, short-range and ripple scattering will be dominant scattering mechanism as the carrier concentration $n$ becomes larger. In other words, the long range charged impurity scattering is suppressed by the strong screening effect. There will be a crossover point where the conductivity profile changes from linear to sublinear function of $n$ when $n$ approaches $n_{imp}$ [48, 49]. Therefore, the larger $n_{imp}$ is, the wider linear region of $\sigma(n)$ is [48]. In the linear region, the carrier mobility can be readily calculated by evaluating the slope $\Delta\sigma/\Delta V_G$.

It is important to note that the charged impurities generally pre-exist in the boundary between graphene and gate oxide (e.g., $SiO_2$) which are the predominant scattering centers when no adsorbate exists on the surface of graphene. When charged impurities (gas molecules) and/or dipolar molecules are adsorbed on *the top* of graphene, they may screen the electrical potentials created by the charged impurities pre-existing on *the bottom* of graphene, thereby counteract the charged impurity scattering due to the pre-existing charged impurities [57]. Previous study suggests that charged impurities (gas molecules) tend to have larger effect on the conductivity of graphene than dipolar molecules [57]. Indeed, increased carrier mobilities due to gas exposures have been observed experimentally [58, 60]. Therefore, the interactions between the pre-existing charged impurities on the bottom of graphene and the charged impurities and/or dipolar molecules on the top of graphene have significant influence on the conductivity change in gas sensing.

## 2.4.4   Summary

In this section, the interactions between gas molecules and graphene have been reviewed by dividing them into three major phenomena: (1) gas adsorption and desorption, (2) charge transfer between gas molecules and graphene, and (3) electron-charged impurity scattering. For chemiresistor type gas sensors, which include graphene-based gas sensors, the surface coverage of gas molecules $\theta$ can be interpreted as gas concentration via partial pressure of a target gas. The surface coverage is linearly proportional to the gas concentration under the limiting cases $KP \ll 1$. After gas adsorption, charge transfer can occur between the gas molecules and graphene depending on: (i) the relative position in the DOS of the HOMO/LUMO of gas molecules and the $E_F$ of graphene; and (ii) hybridization of HOMO/LUMO of gas molecules with the graphene orbitals. After charge transfer, the adsorbed gas molecules become charged impurity scattering centers and affect the conductivity change of graphene. The adsorbed charged impurities also interact with pre-existing charged impurities in the boundary between graphene and gate oxide. As a result of these phenomena, the interactions between gas molecules and graphene are reflected to the changes in carrier concentration ($\Delta\sigma$) and the carrier mobility ($\Delta\mu$), both of which are evaluated by graphene FETs. Therefore, graphene can serve as a chemical-to-electrical transducer, i.e., a gas sensor.

# 2.5   Gas Sensing Schemes

As described in the previous section, upon exposure to gas molecules, the carrier concentration ($n$) and the carrier mobility ($\mu$) of graphene change, and so does the conductivity ($\sigma$). In order to interpret the electrical output signals accurately, graphene FETs must be operated properly based on the fundamental properties. It is even possible to enhance some of the sensor performances by applying advanced gas sensing schemes. In this section, two major gas sensing schemes are introduced.

## 2.5.1   Constant gate voltage scheme

The simplest gas sensing scheme for graphene FETs is the constant gate voltage scheme in which the the gate voltage is fixed to a constant value during the measurements. When the gate voltage is set to zero, the device works as a simple chemiresistor type gas sensor. On the other hand, the magnitude and the sign of the gate voltage must be carefully determined considering the initial charge neutrality point $V_{NP}$ and the doping direction due to gas exposure. Figure 2.14 illustrates how the Fermi level $E_F$ and the conductivity of graphene change over time depending on the the applied gate voltage. For p-type doping, the Fermi level $E_F$ is lowered as time goes by (Figs. 2.14**a-c**). When the gate voltage is fixed to $V_{G1}$, $E_F$ is in the valence band, so the conductivity increases as the concentration of the majority carrier (hole) increases (Fig. 2.14**d**). For $V_{G2}$, $E_F$ is very close to the Dirac point,

so the conductivity first decreases, and then increases (Fig. 2.14**e**). The crossover occurs at the charge neutrality point where the majority carrier switches from electron to hole. For $V_{G3}$, $E_F$ is in the conduction band, so the conductivity decreases as the concentration of the majority carrier (electron) decreases (Fig. 2.14**f**). Similarly, the transient conductivity behaves differently depending on the relationship of the applied gate voltage and the initial charge neutrality point for n-type doping. Therefore, the initial conductivity profile should be evaluated before the constant gate voltage scheme is applied to a measurement. For a long term measurement, one should check the charge neutrality point periodically so that the constant gate voltage can be properly adjusted. As such, despite of the simple concept, the constant gate voltage scheme must be performed with considerations on the magnitude and the sign of the gate voltage, the initial charge neutrality point, and the doping direction (p/n-type).

The constant gate voltage scheme is suitable to quantify the concentration of target gases. However, it is important to note that the observed electrical output signals are not necessary to correspond to a specific target gas unless only the target gas exist in the tested space or gas selectivity is achieved by some engineering approaches such as filters.

## 2.5.2  Sweeping gate voltage scheme

In the sweeping gate voltage scheme, the gate voltage is swept with a certain scanning rate, and the conductivity profile versus the gate voltage is obtained for each instance during the measurements. Figure 2.15 illustrates how the $E_F$ and the conductivity profile versus the gate voltage profile of graphene change over time upon exposure to p-type doping gas. If the graphene is charge neutral at time $t_0$, the $E_{F0}$ should align with the Dirac point (Fig. 2.15**a**), and the charge neutrality point $V_{NP0}$ should be at $V_G = 0$ (Fig. 2.15**d**). The minimum and the maximum Fermi levels, $E_{Fi,min}$ and $E_{Fi,max}$ where $i = 0, 1, 2$, are determined by the minimum and the maximum applied gate voltage, $V_{G,min}$ and $V_{G,max}$, through Eq. (2.28). As the p-type doping process proceeds, the $E_{F1}$ ($E_{F2}$) with $V_G = 0$ is lowered (Figs. 2.15**b&c**), thereby the charge neutrality point $V_{NP1}$ ($V_{NP2}$) shifts to the positive side in $V_G$ (Figs. 2.15**e&f**). If once the conductivity profiles are obtained, the carrier concentration and the carrier mobility can be estimated through Eq. (2.24) and Eq. (2.26). It is also possible to estimate the ratio of the residual carrier concentration to the charged impurity concentration, $n^*/n_{imp}$, using Eq. (2.29). While the constant gate voltage scheme yields the transient conductivity profiles $\sigma(t)$ as scalar values in which all physical information is mixed up, the sweeping gate voltage scheme yields the conductivity profiles $\sigma(V_G)$ as vectors which can be decoupled into distinct physical information. Therefore, the sweeping gate voltage scheme is essential to obtain comprehensive information about gas-graphene interactions. In addition, the transient conductivity profiles $\sigma(t)$, which is obtained by using the constant gate voltage scheme, can be extracted from the results of the sweeping gate voltage scheme as long as the time resolution is sufficiently high. Hence, the sweeping gate voltage scheme is consistently used in this dissertation.
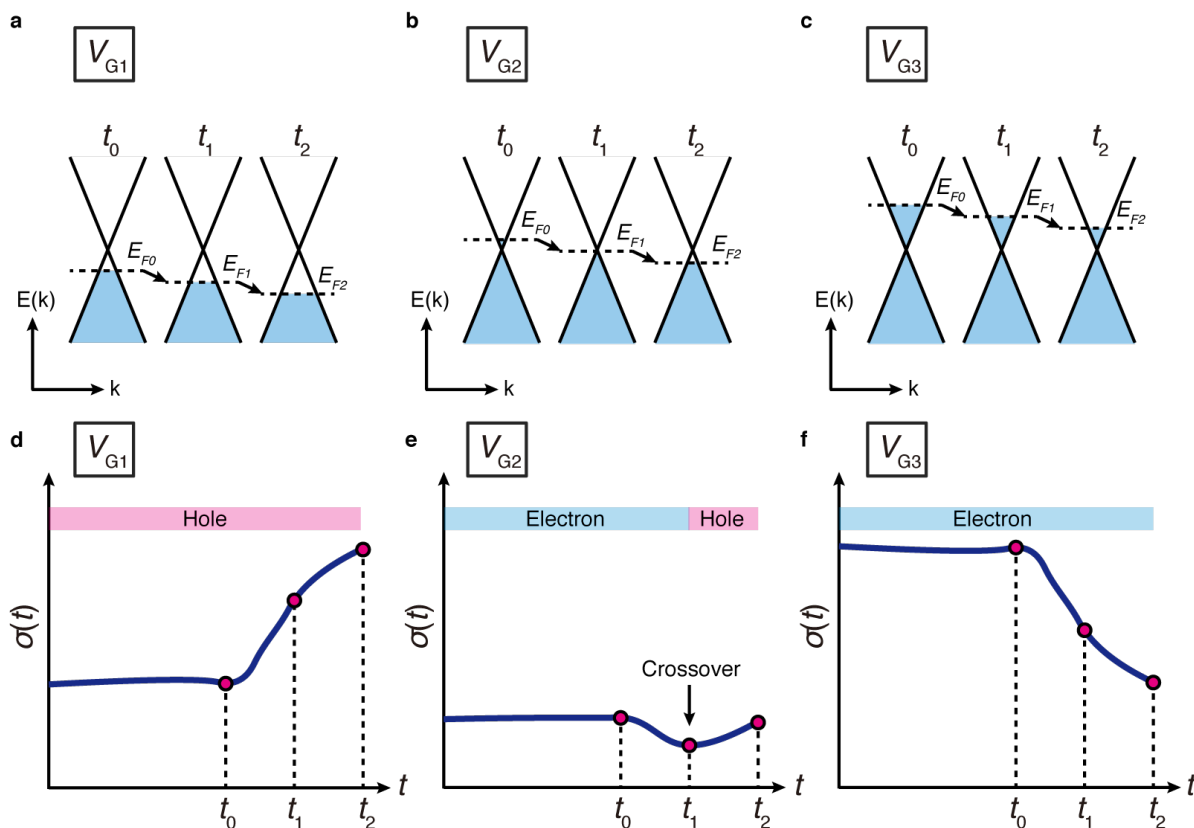
Figure 2.14: Schematic of the energy dispersion of graphene with different constant gate voltage and the corresponding transient conductivity profiles upon exposure to p-type doping gas. **a-b**: Schematic of the energy dispersion of graphene with gate voltage $V_{G1}(\mathbf{a})$, $V_{G2}(\mathbf{b})$, and $V_{G3}(\mathbf{c})$ at time $t_0$, $t_1$, and $t_2$. **d-f**: Transient conductivity profiles over time with gate voltage $V_{G1}(\mathbf{d})$, $V_{G2}(\mathbf{e})$, and $V_{G3}(\mathbf{f})$.
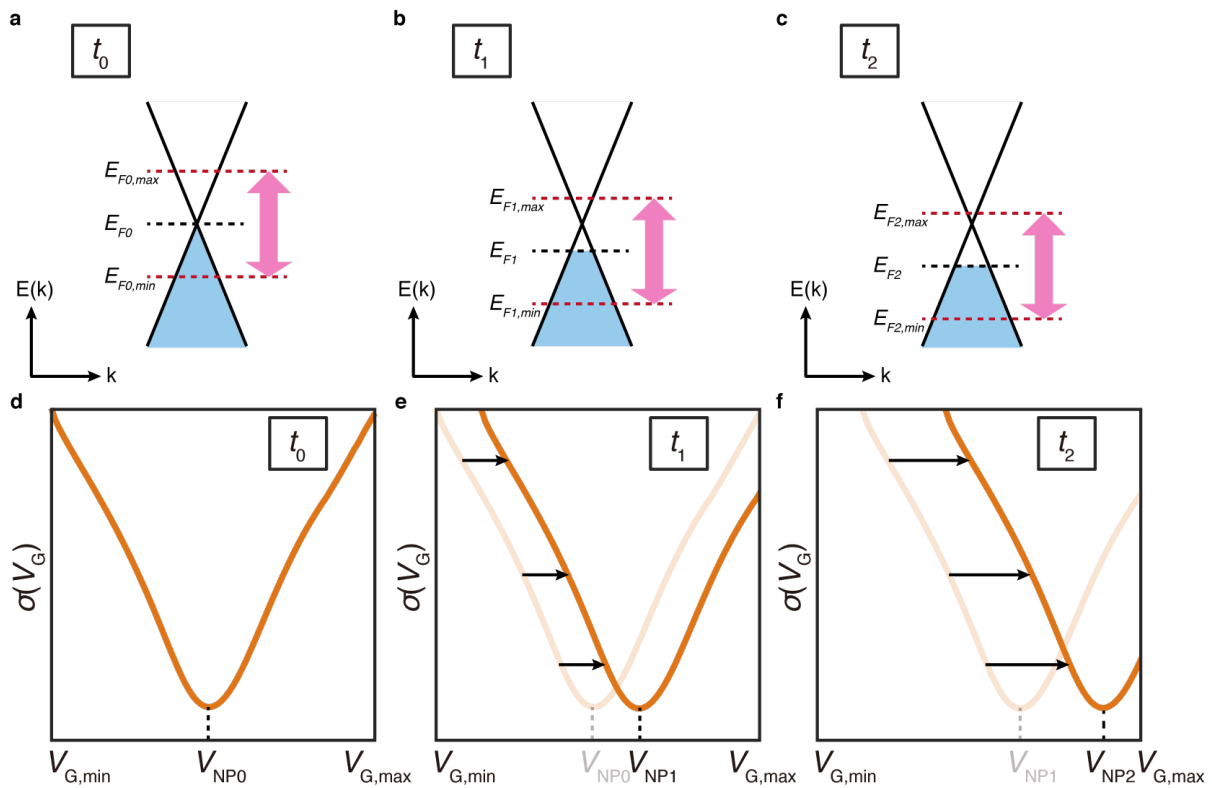
Figure 2.15: Schematic of the energy dispersion with different Fermi levels and the corresponding conductivity profiles versus the gate voltage upon exposure to p-type doping gas. **a-b**: Schematic of the energy dispersion of graphene with the Fermi levels $E_{F0}$(**a**), $E_{F1}$(**b**), and $E_{F2}$(**c**) at time $t_0$, $t_1$, and $t_2$. **d-f**: Conductivity profiles versus the gate voltage at time $t_0$(**d**), $t_1$(**e**), and $t_2$(**f**).

# Chapter 3

# Influence of Environmental Factors

Takeshi Hayasaka, Yoshihiro Kubota, Yumeng Liu, and Liwei Lin

*Berkeley Sensor and Actuator Center and Department of Mechanical Engineering*
*University of California at Berkeley, Berkeley, CA, USA*

## 3.1   Abstract

In this chapter, the influences of temperature, $H_2O$ (humidity), and $O_2$ on the stability of the electrical properties and the gas sensing characteristics of graphene FETs (GFETs) are studied as these environmental factors are often encountered in practical gas sensing applications. Both empirical results and theoretical analyses are characterized for heated GFET-based gas sensors from room temperature to 100 °C under a wide range of applied gate voltages. It is found that at a constant applied gate voltage of $-20$ V with respect to the gate voltage at the charge neutrality point $V_{NP}$, the sensitivity of the device to $H_2O$ decreases; while the sensitivity to $O_2$ decreases first, and increases afterwards as the operation temperature increases. These phenomena are explained by using the physisorption and chemisorption models between the tested gases and the graphene surface. Furthermore, devices operate in the hole regime result in lower sensitivity to $H_2O$ and $O_2$ as compared to those results for the electron regime. As such, this chapter provides foundations to improve the stability of GFET-based gas sensors in practical application environments under the influences of ambient air, temperature, and humidity.

## 3.2 Introduction

As mentioned in section 1.3, one of the most attractive features of graphene-based gas sensors is the high gas sensitivity at room temperature, which leads to the low power consumption, typically in the order of a few tens of $\mu$W, as opposed to the MOX type gas sensors whose typical power consumption is in the order of several tens of mW due to the high operation temperatures. This is a critical difference as power consumption is one of the most important criteria for miniaturized gas sensor applications. Intensive studies on room-temperature operated graphene-based gas sensors [61, 62] have revealed some key obstacles. The first challenge is the influence of temperature due to the temperature-dependent properties of graphene and other peripheral materials such as metals and semiconductors [63, 64]. Another challenge is the influences of $H_2O$ (humidity) and $O_2$ as several studies have reported that graphene-based gas sensors are sensitive to $H_2O$ [65, 66]. Whereas the influences of temperature, $H_2O$, and $O_2$ on MOX type gas sensors have been extensively studied [67, 68], very few studies have been reported for GFETs [65, 69, 70]. Furthermore, there has been no prior study on the influences of these parameters to the gas sensing results of GFETs under different applied gate voltages. In this chapter, we study these factors toward the performances of GFETs for practical applications.

## 3.3 Material and Methods

The fabrication process of the GFETs used in this chapter is described in section 2.3. A scanning electron microscope (SEM) image of the fabricated GFET is shown in Fig. 3.1**a**. The defect states in graphene after fabrication process are evaluated by Raman spectrum (Fig. 3.1**b**) as the information is important for the gas sensitivity and recovery time [71, 72]. The high $I(2D)/I(G)$ ratio ($\sim$3), where $I(2D)$ and $I(G)$ are the intensities of $2D$ and $G$ peaks, agrees with the typical Raman spectrum of a monolayer graphene. The relatively high $I(D)/I(G)$ ratio ( 0.2) implies that some defect states are induced during the fabrication process. The grain size, $L_a$, can be roughly estimated as 20 nm by using a relationship given by $I(D)/I(G) = C(\lambda)/L_a$, where $C(\lambda)$ is $\sim$4.4 nm [73]. This grain size is in the same order of magnitude from the data sheet provided by the vendor [74]. It is noted that the graphene transfer process may introduce impurities such as poly(methyl methacrylate) and $H_2O$ and cause degradation the performance of GFETs, e.g., the carrier mobility [45]. We have confirmed that the degradation due to our fabrication process is small and acceptable in our previous study [75]. The fabricated GFETs are fixed onto ceramic packages by using conductive silver paste. A schematic illustration of the device structure and the electrical configuration is shown in the Fig. 3.1**c**. In this chapter, the sweeping gate voltage scheme is mainly used with either a constant source-drain current $I_{SD} = 100\mu$A or a constant source-drain voltage $V_{SD} = 1$ V and the gate voltage window $\pm$40 V.

Fig. 3.1**d** illustrates the schematic of the gas system and the major components in the chamber. The entire experimental setup is designed to control gas flows and gas concentra-

tions as well as to monitor and control the device operation temperature and the relative humidity (R.H.) level in the chamber. The test chip is placed in the chamber and electrically connected to the power supplies (Keithley 6220 and Agilent 6613C), a semiconductor parameter analyzer (HP 4145B, Hewlett Packard), and a digital multi meter (Agilent 34401A) outside the chamber via feed-through wires. A ceramic heater (18 mm×12 mm×1.2 mm) is fixed to the backside of the chip by mechanical clamps, and two thermocouples are attached to the topside (TC1) and to the backside (TC2), respectively. The heater is controlled by a temperature controller (Digi-sense, Oakton). A commercial humidity sensor (HIH-4000, Honeywell) is placed near the test chip to monitor the R.H. level inside the chamber. Lab-VIEW (National instruments) is used to control the equipment and for the data acquisition. The R.H. level is controlled by the ratio of the flow rates of the two mass flow controllers, MFC1 and MFC2. Saturated water vapor is generated via the vapor source bottle connected to MFC2, and then diluted with the carrier gas, $N_2$, supplied by another line with MFC1. Additional target gas is injected via the third mass flow controller, MFC3. No pump is used in the exhaust line so that the pressure in the chamber is balanced with the atmospheric pressure. The volume of the chamber is about 400 cm$^3$ for these particular experiments and the total flow rate of the gas is maintained at 200 sccm throughout the experiments.

## 3.4   Results and Discussion

### 3.4.1   The influences of temperature in $N_2$

This subsection describes the influence of temperature on the electrical properties of GFETs in $N_2$ atmosphere. Figure 3.2**a** shows that the device operation temperature and the R.H. level which is maintained at a constant level, 4±1%. Figure 3.2**b** shows the recorded results of the source-drain resistance $R_{SD}$ versus the effective gate voltage $V_G - V_{NP0}$ with respect to time, where $V_G$ is the applied gate voltage and $V_{NP0}$ is the gate voltage at the charge neutrality point in the first cycle. The effective gate voltage is used as the label to offset the shifted charge neutrality point due to the initial doping in the graph. The experimental results show that the resistance profiles are affected by the device operation temperature. The resistance profiles versus the gate voltage at different operation temperatures is further characterized in Fig. 3.2**c**. It is observed that the resistance increases nonlinearly as the temperature increases. The analytical investigation starts with the carrier mobility, $\mu$ cm$^2$/(V·s), versus the gate voltage at different operation temperatures as shown in Fig. 3.2**d**. The carrier mobility for a constant source-drain voltage with the geometrical factors is given by

$$\mu_{e/h} = \begin{cases} \dfrac{L}{W}\dfrac{I_{SD}-I_{SD,NP}}{V_{SD}}\dfrac{1}{C_G(V_G-V_{NP})} & \text{for } V_G > V_{NP} \text{ electron branch} \\[2em] \dfrac{L}{W}\dfrac{I_{SD}-I_{SD,NP}}{V_{SD}}\dfrac{1}{C_G(V_{NP}-V_G)} & \text{for } V_G < V_{NP} \text{ hole branch} \end{cases} \tag{3.1}$$
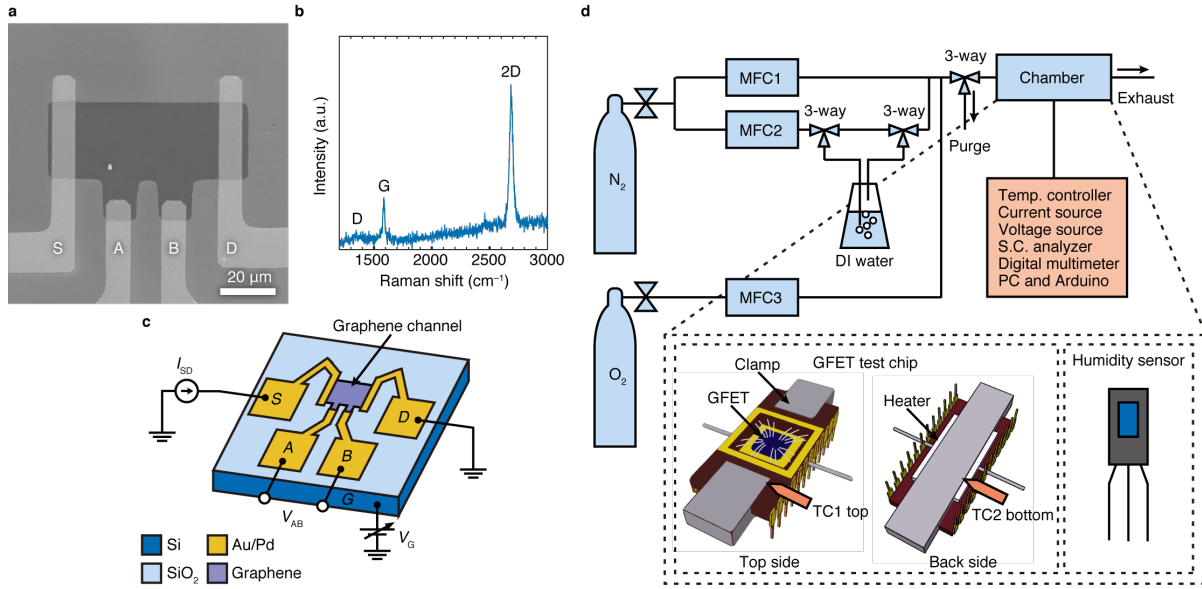
Figure 3.1: Fabricated GFET and the experimental setup. **a** Scanning electron microscope (SEM) image of a fabricated GFET. **b** Raman spectrum of the fabricated GFET. **c** Schematic of a typical electrical configuration for the characterizations. **d** Schematic of the entire experimental setup. The carrier gas, $N_2$, is supplied to the chamber via two mass flow controllers, MFC1 and MFC2. The R.H. level is controlled by the ratio of two flow rates of MFC1 and MFC2. The actual R.H. level is monitored by a commercial R.H. sensor. The device temperature is controlled by a ceramic heater on the back side of the test chip and two thermo couples, TC1 on the top side and TC2 on the back side.

where $\mu_{e/h}$, $L$, $W$, $I_{SD}$, $I_{SD,NP}$, $V_{SD}$, and $c_g \approx 1.15 \times 10^{-8}$ C/(V· cm$^2$) are the mobility of electrons/holes, the length and width of the graphene channel, the source-drain current, the source-drain current at the charge neutrality point, the source-drain voltage, and the gate capacitance per unit area of the GFETs. The abrupt change of $\mu$ at the charge neutrality point is due to the singularity point in the equation. Here, we neglect the calculated $\mu$ near the charge neutrality point as they cannot be evaluated by Eq. (3.1). Instead, we evaluate the $\mu$ away from the charge neutrality point. It is assumed that the Fermi-Dirac distribution does not change drastically in this temperature range (under the same gate voltage) such that the increase in the source-drain resistance can be interpreted as a result of the decrease in the carrier mobility (Fig. 3.2**d**) due to the electron-phonon scattering, or remote interfacial phonon scattering effects [63]. Furthermore, calibration curves with respect to temperature (Fig. 3.2**e**) are fitted by an empirically derived simple monomial equation,

$$\frac{\Delta R}{R_0} \times 100 = aT^k, \quad \Delta R \neq 0 \tag{3.2}$$

where $a$ and $k$ are a factor and an exponent, and the $k$ is given by

$$k = \frac{\log{(\Delta R_2 / R_0)} - \log{(\Delta R_1 / R_0)}}{\log{(T_2)} - \log{(T_1)}} = \frac{\log{(\Delta R_2 / \Delta R_1)}}{\log{(T_2 / T_1)}} \quad (3.3)$$

where $R_0$, $R_1$, $R_2$, $T_1(°C)$, and $T_2(°C)$ are the initial resistance, the resistances at two different temperatures, and the corresponding temperatures, respectively. It is observed that the experimental results are fitted well with ranges of value of $k = 2.16 \sim 2.85$ and $a = 3.3 \times 10^{-5} \sim 8.7 \times 10^{-4}$, respectively, with the coefficient of determinations, $R^2$, ranging from 98.6% to 99.8% (Table 3.1).
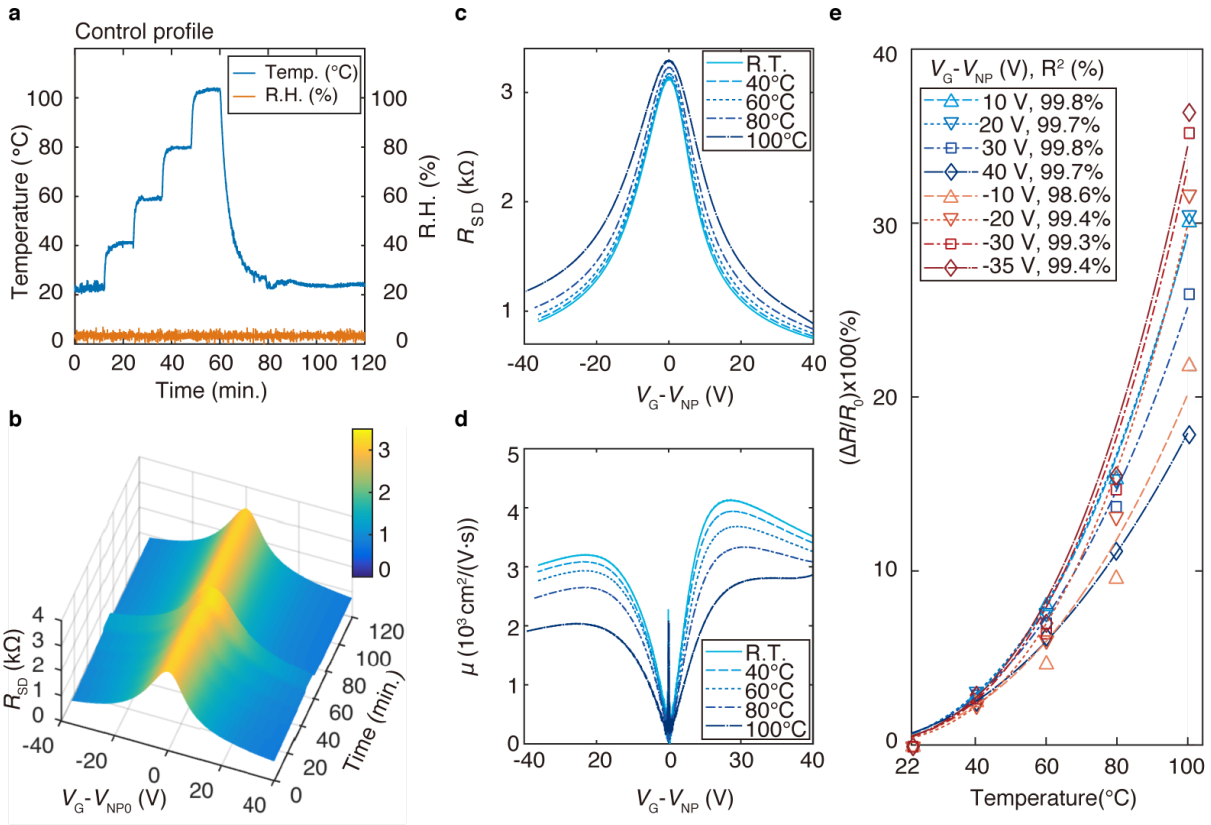


Figure 3.2: Influence of temperature on the electrical properties of GFETs in $N_2$ atmosphere. **a** The temperature control profile with a constant R.H. level in the chamber over time. **b** The source-drain resistance profiles versus the effective gate voltage $V_G - V_{NP0}$ with respect to time. **c** The source-drain resistance and **d** the carrier mobility versus the effective gate voltage $V_G - V_{NP0}$ under various temperatures. **e** Calibration curves with respect to temperature at different effective gate voltages.

The calibration curves in Fig. 3.2**e** shift downwards in the electron regime as the applied gate voltage increases, i.e., as the carrier concentration increases, while those in the hole

| $V_G - V_{NP}$(V) | $a$ | $k$ | $R^2(\%)$ |
|---|---|---|---|
| $-35$ | $9.32 \times 10^{-5}$ | 2.78 | 99.4 |
| $-30$ | $7.98 \times 10^{-5}$ | 2.81 | 99.3 |
| $-20$ | $5.85 \times 10^{-5}$ | 2.85 | 99.4 |
| $-10$ | $3.36 \times 10^{-4}$ | 2.39 | 98.6 |
| $0$ | $3.29 \times 10^{-5}$ | 2.61 | 99.9 |
| $10$ | $2.37 \times 10^{-4}$ | 2.55 | 99.8 |
| $20$ | $2.75 \times 10^{-4}$ | 2.51 | 99.7 |
| $30$ | $2.75 \times 10^{-4}$ | 2.41 | 99.8 |
| $40$ | $8.67 \times 10^{-4}$ | 2.16 | 99.7 |

Table 3.1: Fitting parameters for Eq. (3.2) at different effective gate voltages

regime shift upwards as the magnitude of the applied gate voltage increases. These phenomena suggest that the significant reduction in the hole mobility contributes to the upward trend of $R_{SD}$ in the hole regime as shown in Fig. 3.2**d** ($V_G - V_{NP} < 0$ V) [63]. As such, Eq. (3.2) can be used as the foundations for the source-drain resistance sensing calibrations under different operation temperatures.

## 3.4.2 The influences of $H_2O$ (humidity) in $N_2$ under various temperatures

Fig. 3.3 is the control profile of R.H. with respect to time in which the R.H. level is increased linearly from $4 \pm 1\%$ to $\sim 70\%$ in the first 20 minutes and then linearly decreased to $4 \pm 1\%$ in the next 20 minutes, followed by a purge cycle (at $4 \pm 1\%$) in the last 20 minutes. Figs. 3.4**a-j** show the source-drain resistance (**a-e**) and the carrier mobility (**f-j**) profiles versus the effective gate voltages $V_G - V_{NP0}$ with respect to time at different operation temperature. In these results, the adsorption processes are reversible, suggesting that the adsorption of $H_2O$ on graphene is physisorption-like process (non-covalent binding). It is also observed that the changes in the carrier mobility are reduced as the temperature increases. The sensitivity (resistance change divided by the initial resistance) and the hole concentration with respect to time are calculated under representative applied gate voltages $V_G - V_{NP} = 10$ V and $-10$ V as shown in Figs. 3.3**k-o**. These results indicate that the responses of GFETs to $H_2O$ depend not only on the operation temperature, but also on the applied gate voltage. As the device temperature increases from room temperature to 100°C, the sensitivity to $H_2O$ in the electron regime ($V_G - V_{NP} = 10$ V) reduces from $\sim 70\%$ to less than 20%, while in the hole regime ($V_G - V_{NP} = -10$ V), the sensitivity remains within 15% either at room temperature or 100°C. The sensitivity's relatively large variations in the electron regime when compared with those in the hole regime at various applied gate voltages are also seen at other gate voltages (Figs. 3.3**p-t**). A simple and important conclusion here is that the

sensitivity to $H_2O$ decreases as the temperature increases, which is more clearly seen in the electron regime. This temperature dependency will be further discussed in subsection 3.4.4.
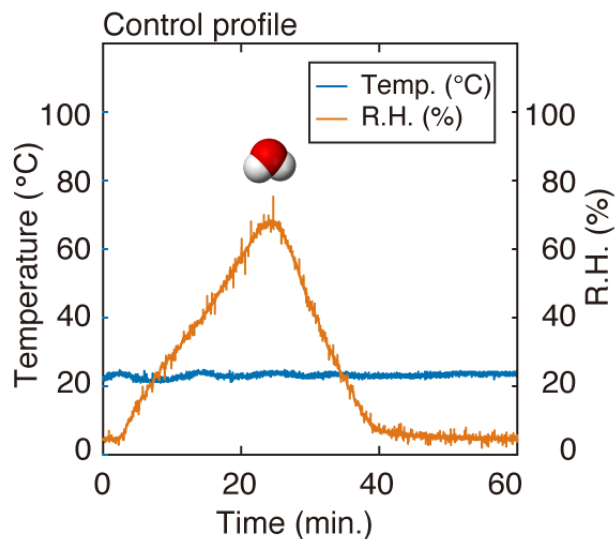


Figure 3.3: The R.H. control profile with a constant temperature in the chamber.
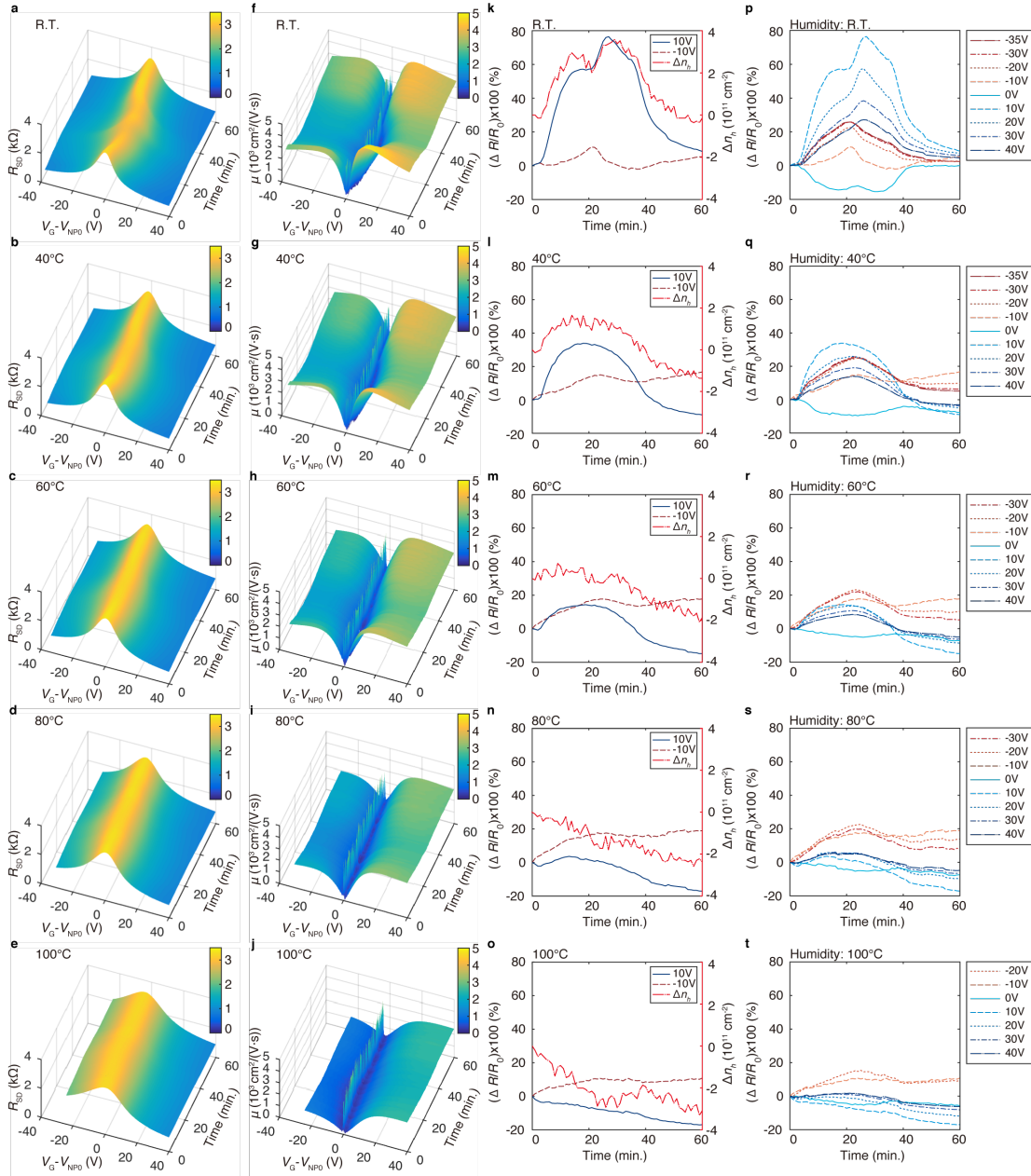
Figure 3.4: The influence of $H_2O$ (humidity) on the electrical properties of GFET in the $N_2$ atmosphere under various temperatures. **a-e** The source-drain resistance profiles versus the effective gate voltage $V_G - V_{NP0}$ with respect to time at different operation temperatures. **f-j** The carrier mobility profiles versus the effective gate voltage $V_G - V_{NP0}$ with respect to time at different operation temperatures. **k-o** Calculated sensitivity (resistance change divided by the initial resistance) and the hole concentration over time at representative applied gate voltages (**p-t**: for other gate voltages).

### 3.4.3 The influences of $O_2$ in $N_2$ under various temperatures

Fig. 3.5 illustrates the control profile of $O_2$ concentration with respect to time under a fixed temperature in which the concentration of $O_2$ is linearly increased from $0\%$ to $\sim 30\%$ in the first 20 minutes, and then linearly decreased to $0\%$ in the next 20 minutes, followed by a purge cycle at $0\%$ in the last 20 minutes. Figs. 3.6**a-j** show the source-drain resistance (**a-e**) and the carrier mobility (**f-j**) profiles versus the effective gate voltages $V_G - V_{NP0}$ with respect to time at different operation temperature. In the low temperature regime, the resistance (and the carrier mobility) profiles barely recover after the p-type doping process upon exposure to $O_2$. These results indicate that the desorption process of $O_2$ is very slow in the low temperature regime. On the other hand, faster recovery process is observed in the high temperature regime. These trends indicate that the interactions between $O_2$ and graphene is chemisorption-like (covalent binding). The sensitivity to $O_2$ and the hole concentration with respect to time at representative applied gate voltages of $V_G - V_{NP} = 20$ V and $-40$ V are shown in Figs. 3.6**k-o**. It is found that the sensitivity to $O_2$ varies depending on both temperature and the applied gate voltage. For example, at $V_G - V_{NP} = 20$ V (chosen due to high sensitivity), the sensitivity decreases from $\sim 160\%$ (at room temperature) to $\sim 60\%$ (60°C) and increases to $\sim 130\%$ at 100°C. This transition can be attributed to a competing effect of increased desorption rate and chemisorption rate [51]. On the other hand, at $V_G - V_{NP} = -40$ V, the sensitivity remains within $\sim 30\%$. Similar to the testing results for $H_2O$, the electron regime tends to be more sensitive to $O_2$ as compared with those in the hole regime (Figs. 3.6**p-t**).
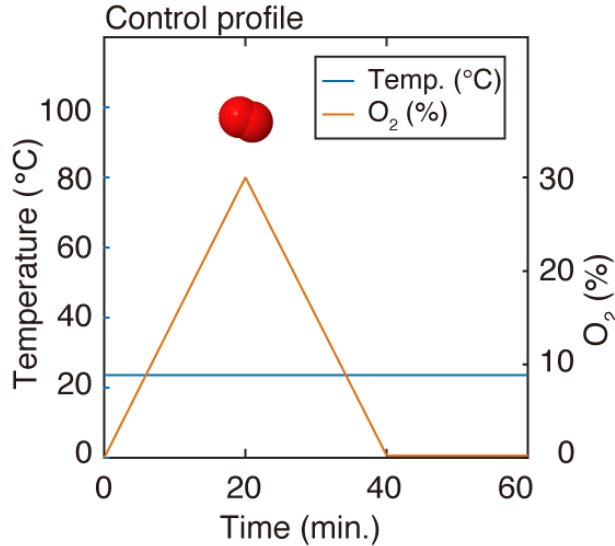


Figure 3.5: The $O_2$ concentration control profile with a constant temperature in the chamber.
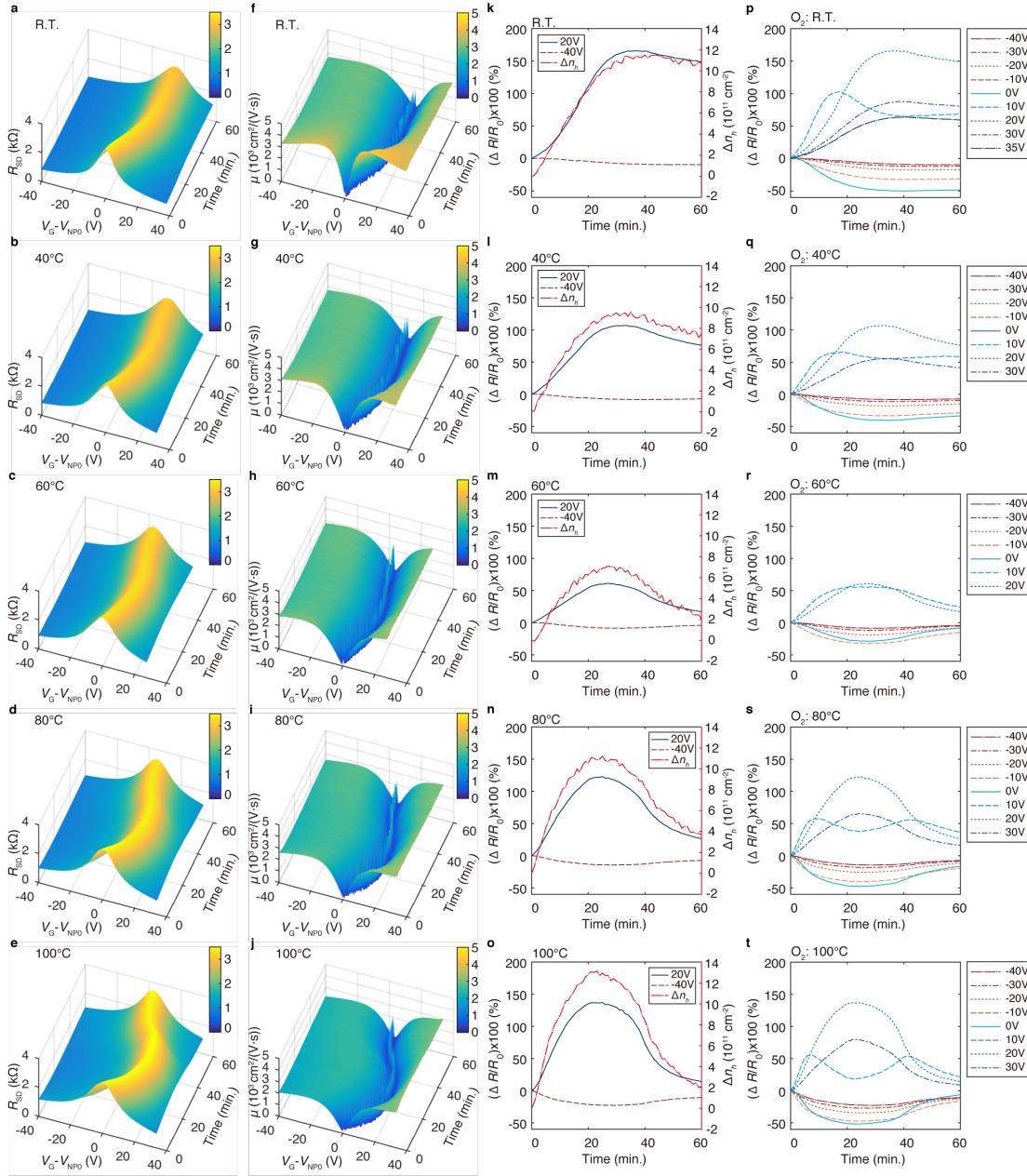
Figure 3.6: The influence of $O_2$ on the electrical properties of GFET in the $N_2$ atmosphere under various temperatures. **a-e** The source-drain resistance profiles versus the effective gate voltage $V_G - V_{NP0}$ with respect to time at different operation temperatures. **f-j** The carrier mobility profiles versus the effective gate voltage $V_G - V_{NP0}$ with respect to time at different operation temperatures. **k-o** Calculated sensitivity (resistance change divided by the initial resistance) and the hole concentration over time at representative applied gate voltages (**p-t**: for other gate voltages).

### 3.4.4 The analyses on the temperature dependent sensitivity to $H_2O$ (humidity) and $O_2$

In order to understand the fundamental mechanisms underlying the temperature dependent sensitivity to $H_2O$ (humidity) and $O_2$ of GFETs, further investigations are performed with a constant gate voltage scheme. Figures 3.7**a&c** show the changes in the source-drain resistance with respect to time upon exposure to $H_2O$, the R.H. is 40% (**a**), and 20% of $O_2$ (**c**) at various device operation temperatures with a constant applied gate voltage, $-3$ V, corresponding to $V_G - V_{NP} \sim -20$ V. This particular applied gate voltage is chosen to realize a stable response, however, with less sensitivity as it is seen in the previous subsections. Figure 3.7**b** shows the extracted sensitivity to $H_2O$ with respect to temperature, where the circle markers and the line are the experimental data and the fitting curve, respectively. The resistance change, $\Delta R_{AV}$, is defined as the average resistance between 75-minute and 90-minute, and is normalized by the initial resistance, $R_0$, to define the sensitivity, $(-\Delta R_{AV}/R_0) \times 100(\%)$. As mentioned in subsection 3.4.2, the reversible sensor response and the temperature dependence indicate that the adsorption process of $H_2O$ on graphene can be explained by physisorption. As mentioned earlier in section 2.4, the potential energy profile for physisorption can be represented by a single Lennard-Jones potential, where the equilibrium distance between gas molecules and a surface of solid increases as the temperature increases due to the higher kinetic energy of the gas molecules. Therefore, a higher device operation temperature results in a higher desorption rate for the gas molecules. Assuming the flux of the incident gas molecules is independent of the device operation temperature, the sensitivity to $H_2O$, $S_{H_2O}(T)$, is considered to be inversely proportional to the rate constant of desorption

$$S_{H_2O}(T) \sim k_{des}^{-1} = A \exp\left(\frac{E_{des,act}}{k_B T}\right) \tag{3.4}$$

where $A$ is a factor related to the inverse of the frequency of the vibration of the bonding. Based on this consideration, the experimental data in Fig. 3.7**b** are fitted by Eq. (3.4), labeled as *Fitting 1*. The fitting curve reasonably agrees with the experimental data with a relatively high correlation, 91.8% of $R^2$. This agreement suggests that the interaction between $H_2O$ and the surface of GFETs may be modeled by a physisorption model. As such, the sensitivity to $H_2O$ is considered to decay exponentially as the device operation temperature increases following Eq. (3.4).

Figure 3.7**d** shows the extracted sensitivity (in logarithmic scale) to $O_2$ with respect to the inverse of temperature. The square markers and the line are the experimental data and the fitting curve. The definitions of the notations are the same as Fig. 3.7**b**. In contrast to the results for $H_2O$, the sensitivity to $O_2$ increases as the temperature increases in the given temperature range. This phenomenon can be explained in the following way. For chemisorption-like gas molecules, the potential energy at a surface of solid has two local minima as shown in Figs. 2.11**b&c** [50]. At the first local minimum with a longer distance from the surface, the state of gas molecules is in a physisorption state, while at the second local minimum with a shorter distance from the surface, the state of gas molecules is in a

chemisorption state. For a transition from physisorption state to chemisorption state, the gas molecules have to overcome a potential energy barrier with sufficient activation energy, $E_{ads,act}$. Therefore, excessive thermal energy can contribute to overcome the potential energy barrier and/or to increase the rate of desorption. As such, there will be more chemisorbed gas molecules on the surface of graphene as the device operation temperature increases. This trend will prevail up to a certain temperature at which the supplied thermal energy exceeds the activation energy for desorption, $E_{des,act}$. This model suggests that the sensitivity to $O_2$, $S_{O_2}(T)$, may be related to the Arrhenius equation [50]

$$S_{O_2}(T) \sim k_{des} = \nu \exp\left(\frac{E_{des,act}}{k_B T}\right) \tag{3.5}$$

where $\nu$ is the frequency of the vibration of the bonding. This relationship is often described in the Arrhenius plot by taking the natural logarithm of the both sides

$$\ln\left[S_{O_2}(T)\right] \sim \ln(\nu) - \frac{E_{des,act}}{k_B T} \tag{3.6}$$

The obtained experimental data are fitted well by Eq. (3.6) with a high correlation, 97.5% of $R^2$ as shown in Fig. 3.7**d** (*Fitting 2*). This agreement suggests that the adsorption of $O_2$ on the surface of graphene can be modeled by a chemisorption model in the given temperature range. As such, the sensitivity to $O_2$ increases exponentially as the device operation temperature increases. The chemisorption-like behavior in the relatively low temperature regime can be attributed to the dangling bond defects on the grain boundaries of the graphene channel. Previous studies have suggested that the dangling bond defects can serve as chemisorption sites for $O_2$ [76].

A key conclusion here is that the sensitivity to $H_2O$ decreases exponentially as the device operation temperature increases, while the sensitivity to $O_2$ increases exponentially in the given temperature range. These different temperature dependencies can be attributed to the different natures of physisorption and chemisorption associated with the adsorbates. These analyses suggest that the sensitivity to chemisorption-like target gas molecules may be enhanced by increasing the device operation temperature depending on the associated activation energies, while the influence of $H_2O$ may be mitigated. In other words, selectivity to a certain chemisorption-like target gas may be improved by controlling the device operation temperature.
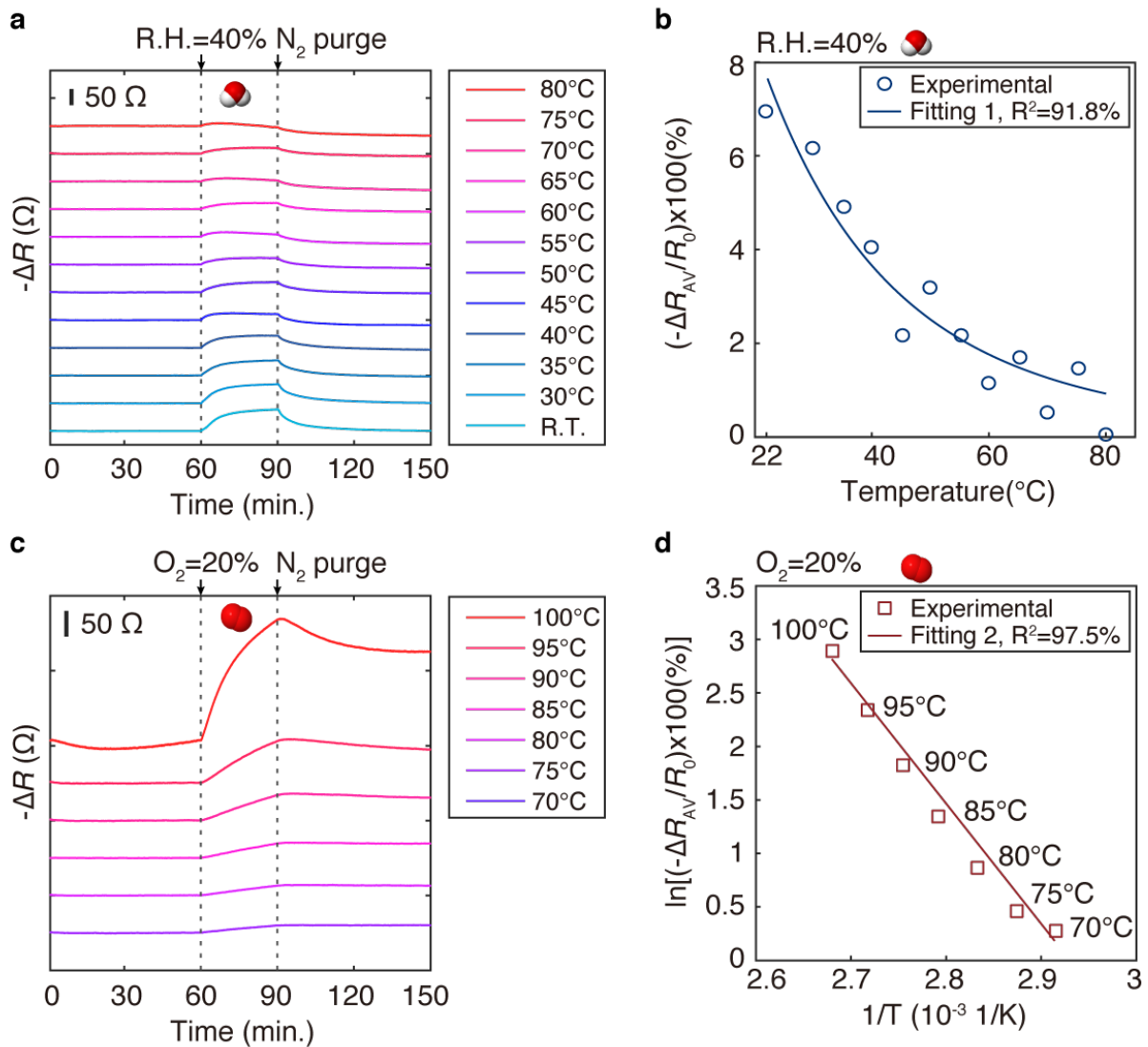
Figure 3.7: Temperature dependence on the sensitivity to $H_2O$ (humidity) and $O_2$. **a&c** Changes in the source-drain resistance with respect to time upon exposure to $H_2O$, the R.H. is 40% (**a**), and 20% of $O_2$ (**c**) at various device operation temperatures with a constant applied gate voltage, $-3$ V, corresponding to $V_G - V_{NP} \sim -20$ V. **b&d** Extracted resistance sensitivity from the results in **a&c**.

## 3.5 Conclusion

In conclusion, this chapter studies the stability of the electrical properties and the gas sensing properties of GFETs under various conditions of temperature, $H_2O$ (humidity), $O_2$, and

applied gate voltage. It is found that the source-drain resistance can be influenced by temperature throughout the range of the applied gate voltages and the empirical equation Eq. (3.2) can be used as the calibration curves for temperature between room temperature to 100°C. The influences of $H_2O$ and $O_2$ are also analyzed at various temperatures and applied gate voltages. It is found that the electrical properties and the gas sensing results can be drastically changed due to the existence of $H_2O$ and $O_2$ as well as the combination of the operation temperature and the applied gate voltages. Specifically, in the electron regime ($V_G - V_{NP} > 0$ V), GFETs are very sensitive to both $H_2O$ and $O_2$ at low device operation temperatures. As the device operation temperature increases, the sensitivity to $H_2O$ decreases, while that of $O_2$ decreases first, and then increases. These different temperature dependencies are explained well by the physisorption and the chemisorption models. On the other hand, in the hole regime ($V_G - V_{NP} < 0$ V), the sensitivity against both $H_2O$ and $O_2$ are much smaller than that in the electron regime. As such, at higher device operation temperatures, the sensitivity to $H_2O$ can be reduced regardless of the applied gate voltage, while the sensitivity to $O_2$ can be increased. The analyses further suggest that the selectivity to chemisorption-like target gases can be improved by controlling the device operation temperature. The experimental results and the analyses in this chapter provides fundamental information to manipulate or compensate the influences of temperature, $H_2O$, and $O_2$ to the GFET-based gas sensing applications.

## 3.6 Acknowledgements

# Chapter 4

# Chemical Functionalization via ALD

Takeshi Hayasaka[1], Vernalyn C. Copa[1,2,3], Lorenzo P. Lopez Jr.[1,2,3], Regine A. Loberternos[1,2,3], Laureen Ida M. Ballesteros[1,2,3], Albert Lin[1], Yoshihiro Kubota[1], Huiliang Liu[1,4], Arnel A. Salvador[2,3], and Liwei Lin[1,4]

[1]*Berkeley Sensor and Actuator Center and Department of Mechanical Engineering*
*University of California at Berkeley, Berkeley, CA, USA*
[2]*Materials Science and Engineering Program, College of Science*
*University of the Philippines Diliman, PHILIPPINES*
[3]*National Institute of Physics, College of Science*
*University of the Philippines Diliman, PHILIPPINES*
[4]*Tsinghua-Berkeley Shenzhen Institute, Tsinghua University, CHINA*

## 4.1   Abstract

In this chapter, unique graphene-catalyst hybrid structure is proposed to realize both high gas sensitivity and reproducibility. The proposed device structure is readily realized by standard MEMS fabrication process. For the catalytic layer, atomic layer deposition (ALD) RuO$_2$ is used. Here, our interest is not only to improve the sensitivity, but also the selectivity. Therefore, the gas sensing properties of a pristine-GFET and a ALD-RuO$_2$ functionalized GFET are compared using unique gas sensing scheme. The unique gas sensing is introduced in this chapter, and further discussed in chapter 5. Compared with the state-of-the-art, three

distinctive advancements have been achieved: (1) enhanced sensitivity using the scheme of electron mobility characterizations by a hybrid structure of graphene and ALD-RuO$_2$ base layer; (2) first demonstration of gas sensing by means of the 4-dimentional (4D) physical properties vectors of graphene FETs; and (3) using the 16-dimensional (16D) characteristic gas sensing pattern to distinguish water vapor and methanol. As such, the proposed unique device structure and the measurement scheme could offer enhanced sensitivity as well as selectivity.

## 4.2   Introduction

In the past decade, graphene-based gas sensors have been extensively studied due to the superior gas sensing capability at room temperature for a wide variety of gas species [20, 61, 77, 78]. At the same time, however, pristine graphene-based gas sensors have relatively low sensitivity when compared with the heated, MOX type gas sensors due to the smaller number of chemisorption sites [79]. On the other hand, gas sensors based on graphene-based hybrids have been proposed with significant enhancements of the gas sensing sensitivities [79, 80]. However, most of these techniques are limited with irreproducible fabrication processes and poor selectivity. Most of the conventional gas sensors have relied on chemical functionalization to improve the selectivity but they generally face issues such as cross-sensitivities. Specifically, as long as scalar-valued output signals are used for gas sensing, the ideal transducers are expected to have selective gas adsorption sites to offer selectivity. However, in general, it is challenging to realize such selective adsorption sites with scalable techniques. As such, these issues have severely constrained the practicality of graphene-based gas sensors. In this chapter, we propose a few new approaches to address the gas sensitivity and the selectivity issues: (1) a hybrid structure of graphene and ALD-RuO$_2$ using a reproducible fabrication process; and (2) a unique gas characterization scheme based on the 4 distinctive physical properties of GFETs.

RuO$_2$ is used as catalyst as previous studies have reported that ruthenium and RuO$_2$ are promising catalyst which enhances the sensitivity toward various gas species including NO$_2$, VOCs, hydrocarbons, CO, H$_2$S, and H$_2$ [81–83]. Although the mechanism behind the enhanced sensitivity is not clear, the observed catalytic effect can be attributed to the adsorption configurations of the gas molecules and their dissociative reactions on the ruthenium sites [82].

## 4.3   Methodology

### 4.3.1   Concept of graphene-ALD-RuO$_2$ hybrid

ALD-RuO$_2$ is used as active catalytic sites based on the following concept: Figure 4.1 illustrates the structural models and the electron energy band diagrams of the ALD-RuO$_2$-GFET.

The surface can be covered with oxygen species before the target gas molecules are adsorbed as showing in Fig. 4.1**a** with the electron energy band diagram shown in Fig. 4.1**b**. Both the electronic and catalytic mechanisms predict that the active catalytic sites can accelerate oxidation or reduction processes [84]. When reducing gases are oxidized as shown in Fig. 4.1**c**, electrons are released to the graphene, thereby the carrier concentration in graphene ca change as shown in Fig. 4.1**d**. As shown in the structural models, the ALD-RuO$_2$ layer is underneath the graphene channel with opening holes. This structure allows gas molecules to interact with both graphene and ALD-RuO$_2$ layer, and it is easily reproduced by standard MEMS fabrication processes.
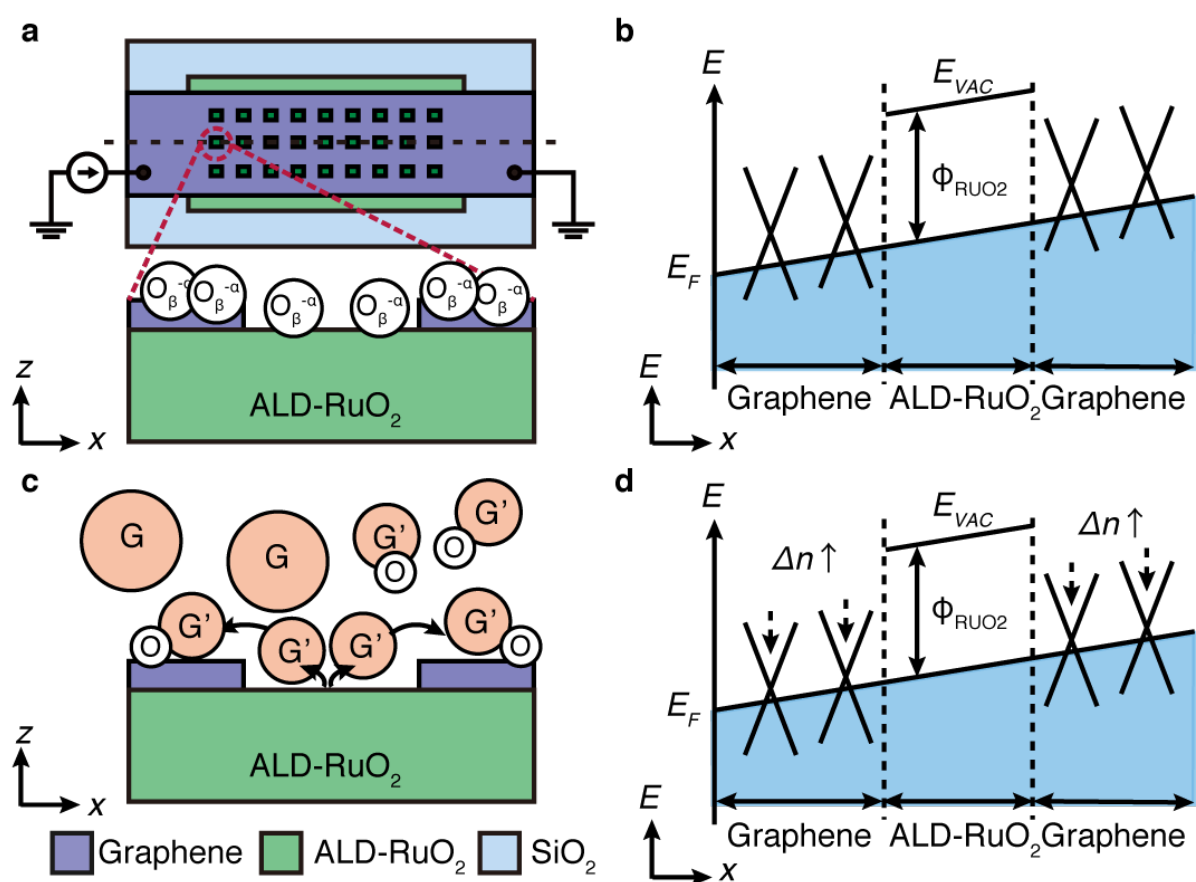


Figure 4.1: Schematic of the structural models and the energy band diagrams of the ALD-RuO$_2$ functionalized GFET gas sensor. **a** Schematic of the top and the cross sectional view of the device before the target gas molecules are adsorbed. The surface is covered with oxygen species. **b** Schematic of the electron energy band diagram of the device before the gas exposure. **c** Absorbed gas molecules can be oxidized or reduced via the ALD-RuO$_2$ catalytic layer. **d** After oxidation or reduction process, either electrons or holes will be released to graphene, thereby the carrier concentration in graphene can increase or decrease.

## 4.3.2   Fabrication process

Figure 4.2 illustrates the fabrication process of ALD-RuO$_2$-GFET. First, the ALD-RuO$_2$ base layer is deposited on a SiO$_2$/Si (300 nm/500 $\mu$m) wafer (Fig. 4.2**a**). The conditions of the ALD process can be found elsewhere [85]. Afterwards, Au/Pd (50 nm/25 nm) contact pads are patterned by a lift-off process (Fig. 4.2**b**). The ALD-RuO$_2$ base layer is then patterned by oxygen plasma etching (Fig. 4.2**c**). Afterwards, a monolayer graphene is transferred onto the substrate (Fig. 4.2**d**). Finally, the graphene layer is patterned by oxygen plasma etching (Fig. 4.2**e**). The close-up view of the graphene-ALD-RuO$_2$ hybrid structure is shown in Fig. 4.2**f**. The ALD-RuO$_2$ base layer is exposed to the surroundings via the opening holes in the graphene channel.
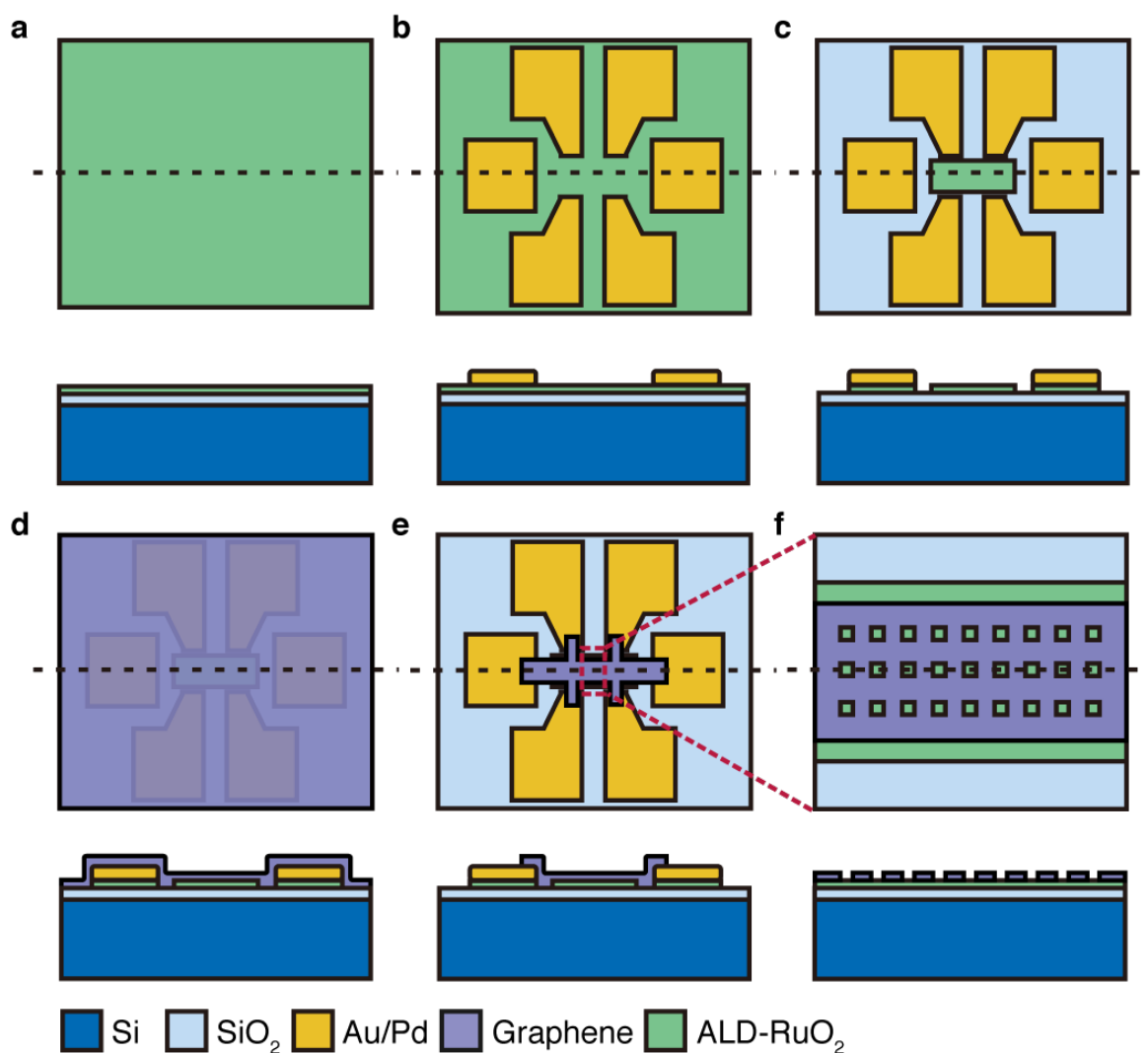
Figure 4.2: Schematic of the fabrication process, the top and cross-sectional views for each step. **a** The ALD-$RuO_2$ base layer is deposited on a $SiO_2$/Si (300 nm/500 $\mu$m) wafer. **b** Au/Pd (50 nm/25 nm) contact pads are patterned by a lift-off process. **c** The ALD-$RuO_2$ base layer is patterned by oxygen plasma etching. **d** A monolayer graphene is transferred onto the substrate. **e** The graphene layer is patterned by oxygen plasma etching. **f** The close-up view of the graphene-ALD-$RuO_2$ hybrid structure: the ALD-$RuO_2$ base layer is exposed to the ambient air via the opening holes in the graphene channel.

### 4.3.3   Characterization scheme

Figure 4.3 illustrates the graphical flow chart of the proposed characterization scheme. First, the conductivity profiles versus the effective gate voltage are collected with the sweeping gate voltage scheme as shown in Fig. 4.3**a**. The measured conductivity profiles are then decoupled into 4 distinctive values: (1) the slope in the positive gate voltage region $\Delta\sigma_e/\Delta V_G$; (2) the absolute gate voltage value at the charge neutrality point $\Delta V_{NP}$; (3) the slope in the negative gate voltage region $\Delta\sigma_h/\Delta V_G$; and (4) the minimum conductivity $\sigma_0$. Afterwards, these values are converted into 4 distinctive physical properties of GFET, i.e., the 4D physical properties vector, $\boldsymbol{q}$, including: $q_1$ as the electron mobility ($\mu_e$); $q_2$ as the carrier concentration ($n$); $q_3$ as the hole mobility ($\mu_h$); and $q_4$ as the ratio of the residual carrier concentration to the charged impurity concentration ($n^*/n_{imp}$), as shown in Fig. 4.3**a** [49]. The obtained 4D physical properties vectors can be projected onto a polar plot such that the characteristics of the two different GFETs can be compared (Fig. 4.3**c**). Since the 4D vectors can be generated for each instance, we are able to use the vectors as 4D output signals for gas sensing.

The normalized vector, $\boldsymbol{q}_n = \boldsymbol{q}(t)/\boldsymbol{q}_0$, and the sensitivity vector, $\boldsymbol{q}_s = 100\times(\boldsymbol{q}(t)-\boldsymbol{q}_0)/\boldsymbol{q}_0$, are defined for gas sensing characteristics, where $\boldsymbol{q}(t)$ is the transient 4D vector and $\boldsymbol{q}_0$ is the initial or reference vector. The former is useful to visualize the transient 4D vectors over time, and the latter is useful for to extract the changes of the 4D vectors induced by the gas exposures. The concept of the sensitivity vector is exactly the same as the definition of the sensitivity which is often used for conventional gas sensors, i.e., a quantity given by $100 \times (R(t) - R_0)/R_0$, where $R$ is resistance, for example. The 4D sensitivity vectors can provide characteristic gas sensing patterns due to the multi dimensionality, whereas the scalar-valued output signals can only provide information related to the gas concentrations. The dimensionality of the physical properties vectors can be effectively extended when multiple graphene FETs are prepared with unique sensing performances. It is noted that the transducers here do not need to have perfectly selective adsorption sites, as long as they exhibit unique sensing characteristics.

## 4.4   Results

Figure 4.4**a** shows the scanning electron microscope (SEM) image of the fabricated ALD-$RuO_2$-GFET. The darker gray colored area corresponds to the graphene channel with opening holes and the lighter gray rectangle area underneath the graphene channel corresponds to the ALD-$RuO_2$ base layer. Figure 4.4**b** shows the X-ray photoelectron spectroscopy (XPS) spectra of the substrate before (blue-line) and after (orange-line) etching the ALD-$RuO_2$ base layer. The absence of the Ru (3p) peaks after the etching process indicates that the ALD-$RuO_2$ base layer is properly etched away.

Figure 4.5 shows the conductivity profiles of pristine-GFET (**a&c**) and ALD-$RuO_2$-GFET (**b&d**) versus the effective gate voltage with respect to time. The devices are exposed to target gases, $H_2O$ (**a&b**) and methanol (**c&d**), with a concentration of 30% between 10-
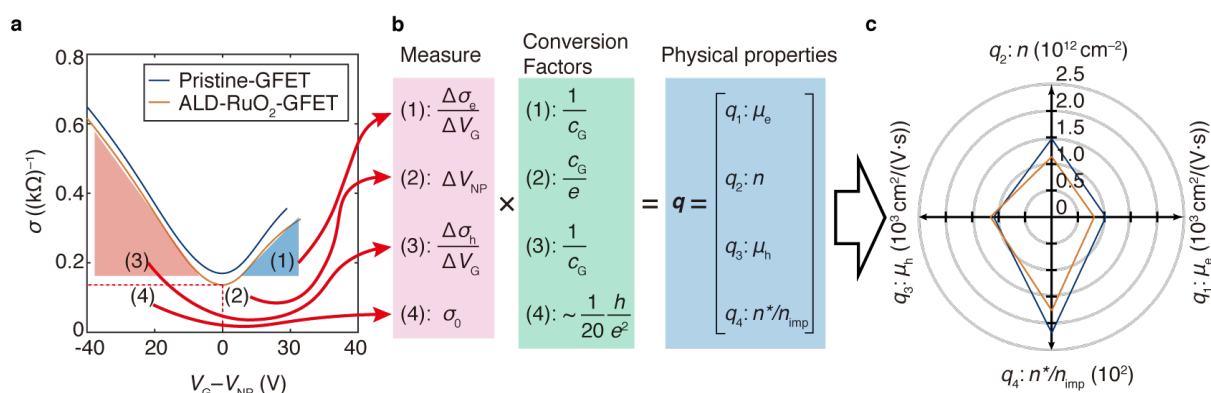
Figure 4.3: Graphical flow chart of the proposed characterization scheme. **a** The conductivity profiles versus the effective gate voltage of the pristine-GFET and the ALD-$RuO_2$-GFET. **b** Conversion of the measured quantities into the 4D physical properties vector. **c** Projected two 4D vectors onto a polar plot which compares the characteristics of the two different GFETs.
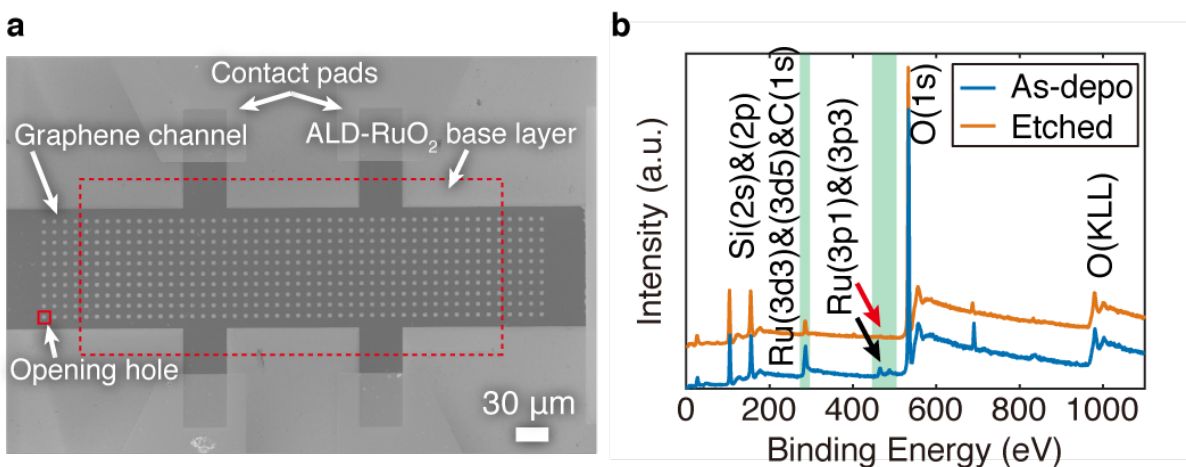


Figure 4.4: Characterizations of the fabricated device. **a** The SEM image of the fabricated device. The darker gray colored area corresponds to the graphene channel with the opening holes and the lighter white rectangle area underneath the graphene channel corresponds to the ALD-$RuO_2$ base layer (enclosed by red dash line). **b** The XPS spectra of the substrate before (blue-line) and after (orange-line) etching the ALD-$RuO_2$ base layer. The Ru (3p) peaks disappear after the etching.

to-20- and 30-to-40-minutes periods. The chamber is purged by dry air when the target gases are not supplied.

From these data, we can extract the 4D physical property vectors with respect to time as mentioned earlier, and they are plotted as shown in Fig. 4.6, for pristine-GFET (**a&c**) and ALD-RuO$_2$-GFET (**b&d**)). Figures 4.6**a&b** and **c&d** show the sensing results for H$_2$O and methanol (MeOH) respectively. The key results here are that: (1) the sensitivity in terms of the electron mobility is enhanced up to $\sim$ 4 times for the ALD-RuO$_2$-graphene FET; (2) the 4D vectors look different between the purge cycles and the gas exposure cycles; (3) the transient vector patterns look different between H$_2$O and MeOH; (4) the transient vector patterns look different between two different devices; and (5) the transient vector patterns look consistent in the gas exposure cycles. These results indicate that the 4D physical properties vectors can generate distinctive gas sensing patterns for H$_2$O and MeOH. In addition, device dependent gas sensing patterns are expected.

Figure 4.7 demonstrates the multi dimensional gas sensing patterns generated by the 4D physical properties vectors. Figures 4.7**a-d** show the normalized vectors projected onto the 4D polar plots: the black lines and the red lines represent the averaged data in the purge cycles and the gas exposure cycles, respectively. Since we are interested in the changes between the purge cycles and the gas exposure cycles, Figs.4.7**e-h** extract the differences by projecting the sensitivity vectors, $\boldsymbol{q}_s$, onto the 8D polar plots. Here, the negative sensitivity changes are projected to $-\boldsymbol{q}_{si}(i:1-4)$ axes for visualization purpose, thereby the dimension of the axes is extended to 8D. These 8D polar plots help to visualize the distinctive gas sensing patters. Figures 4.7**i&j** demonstrate the extended dimensionality of the gas sensing patterns from 8D to 16D, by combining the two sensitivity vectors from the two different GFETs. As these gas sensing patterns are distinctive, they can potentially serve as the fingerprints for the detected gases.

## 4.5   Conclusion

We have demonstrated multi dimensional distinctive gas sensing patterns for H$_2$O and MeOH using pristine-GFET and ALD-RuO$_2$-GFET with a novel characterization scheme. The proposed graphene-ALD-RuO$_2$ hybrid structure enhances the electron mobility sensitivity up to $\sim$ 4 times. This value may be further enhanced by optimizing the geometry of the holes in the graphene channel. The hybrid structure can be applied to various other functionalization materials, e.g., other metal oxides and noble metals, with standard MEMS fabrication processes. The 4D physical properties vectors are unique for different gases and also for different devices. Therefore, the gas sensing patterns can potentially serve as the fingerprints of the detected gases. In addition, the 16D gas sensing patterns indicate that a higher dimensionality of the physical properties vector can be achieved by combining multiple GFETs with unique gas sensing properties, and it will contribute to improve the robustness of the data analysis. As such, this chapter demonstrates a unique approach to realize both enhanced sensitivity and selective gas sensing.
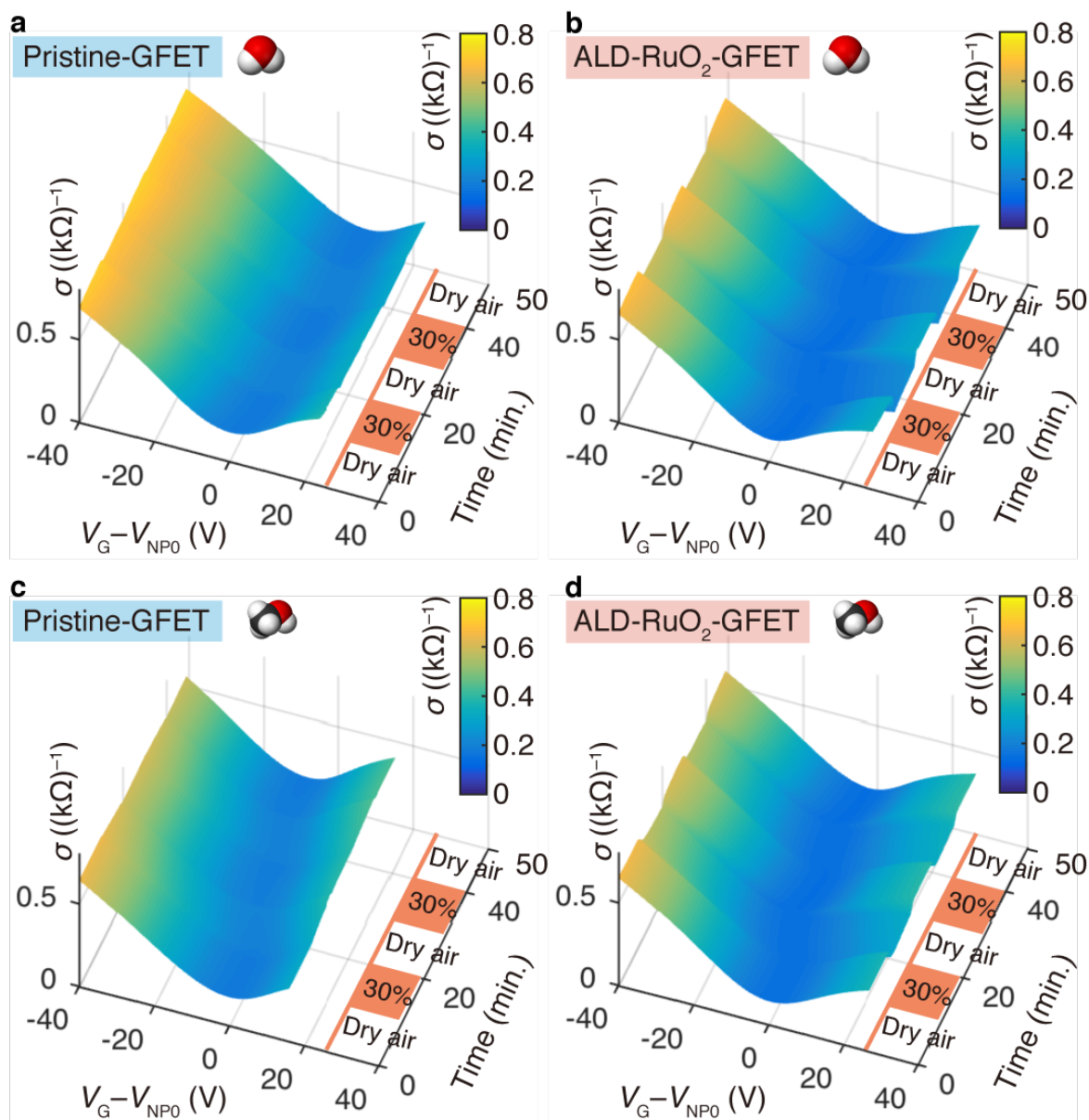
Figure 4.5: Conductivity profiles of pristine-GFET (**a&c**) and ALD-RuO$_2$-GFET (**b&d**) versus the effective gate voltage with respect to time. The devices are exposed to target gases, H$_2$O (**a&b**) and methanol (**c&d**), with a concentration of 30% between 10-to-20- and 30-to-40-minutes periods. Dry air is used as the carrier gas.
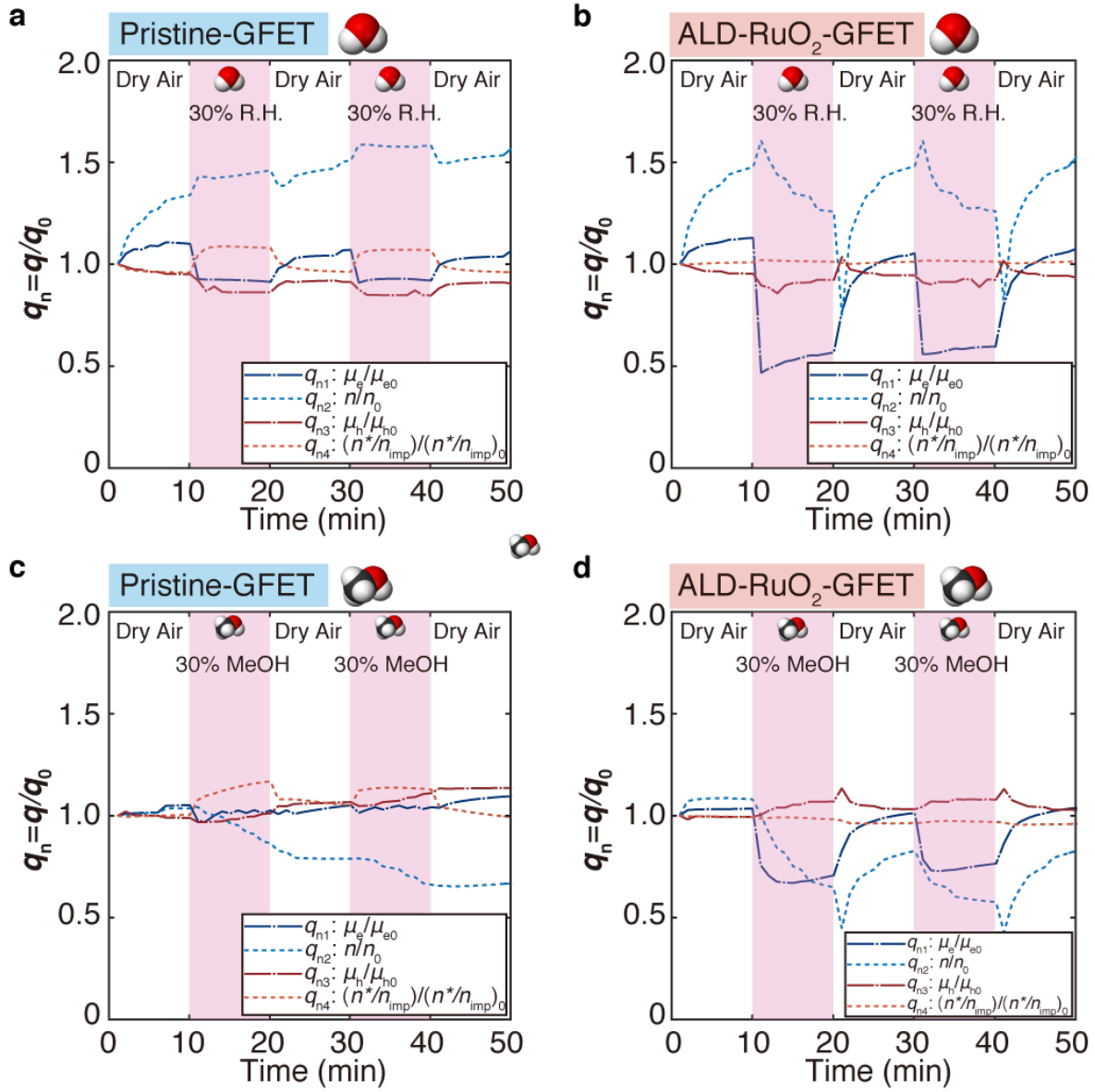
Figure 4.6: Normalized vector, $\boldsymbol{q}_n = \boldsymbol{q}(t)/\boldsymbol{q}_0$, with respect to time of pristine-GFET (**a&c**) and ALD-RuO$_2$-GFET (**b&d**)) upon gas exposures, H$_2$O (**a&b**) and methanol (**c&d**), with a concentration of 30% between 10-to-20- and 30-to-40-minutes periods.
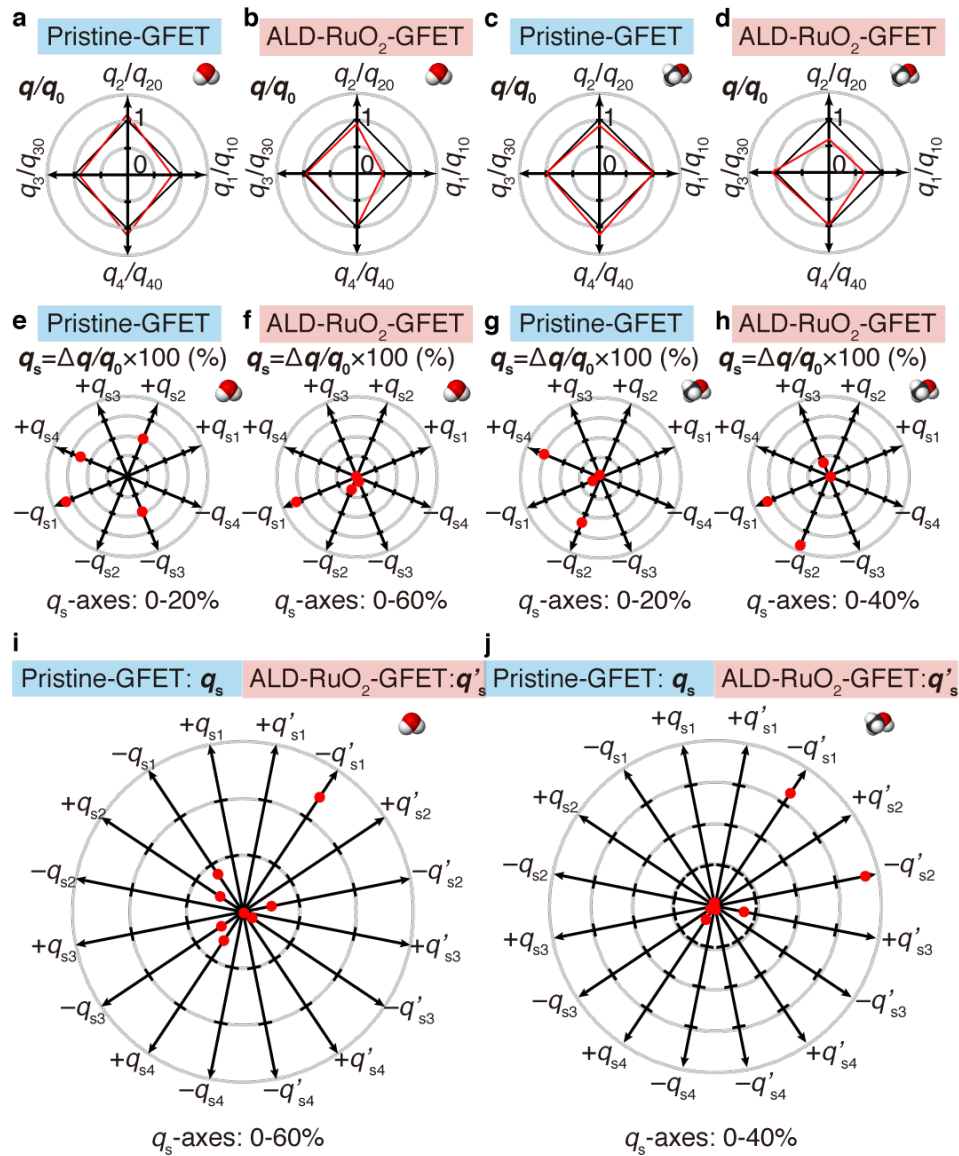
Figure 4.7: The multi dimensional gas sensing patterns generated by the 4D physical properties vectors (**a,c,e,g**: pristine-GFET; **b,d,f,h**: ALD-RuO$_2$-GFET; **a,b,e,f,i**: water vapor; **c,d,g,h,j**: methanol; **i,j**: the data come from both pristine-GFET and ALD-RuO$_2$-GFET). **a-d** The normalized vectors projected onto the 4D polar plots: the black lines and the red lines represent the averaged data in the purge and the gas exposure cycles, respectively. **e-h** The sensitivity vectors projected onto the 8D polar plots. **i&j** The combined sensitivity vectors from two different devices projected onto the 16D polar plots for water vapor (**i**) and methanol (**j**).

## 4.6    Acknowledgement

# Chapter 5

# Electronic Nose Using Single Graphene FET

Takeshi Hayasaka[1], Albert Lin[1], Vernalyn C. Copa[2,3], Lorenzo P. Lopez Jr.[2,3], Regine A. Loberternos[2,3], Laureen Ida M. Ballesteros[2,3], Yoshihiro Kubota[1], Yumeng Liu[1], Arnel A. Salvador[2,3], and Liwei Lin[1]

[1]*Berkeley Sensor and Actuator Center and Department of Mechanical Engineering*
*University of California at Berkeley, Berkeley, CA, USA*
[2]*Materials Science and Engineering Program, College of Science*
*University of the Philippines Diliman, PHILIPPINES*
[3]*National Institute of Physics, College of Science*
*University of the Philippines Diliman, PHILIPPINES*

## 5.1    Abstract

The poor gas selectivity problem has been a long-standing issue for miniaturized chemiresistor type gas sensors. The electronic nose (e-nose) was proposed in the 1980's to tackle the selectivity issue, however, it required inefficient top-down chemical functionalization processes to deposit multiple functional materials. In this chapter, we develop an e-nose system based on a single GFET to achieve selectivity, miniaturization, low cost, and low power consumption. Instead of using multiple functional materials, the gas sensing conductivity profiles of a GFET are recorded and decoupled into four distinctive physical properties and

projected onto a feature space as 4D output vectors and classified to differentiated target gases by using machine learning analyses. Our single-GFET approach coupled with trained pattern recognition algorithms was able to classify water, methanol, and ethanol vapors with high accuracy quantitatively. Furthermore, the gas sensing patterns of methanol were qualitatively distinguished form that of water vapor in a binary mixture condition, suggesting that the proposed scheme is capable of differentiating a gas in the realistic scenario of ambient environment with background humidity. As such, this work offers a new class of e-nose sensing scheme using a single GFET without multiple functional materials towards practical gas sensing applications.

## 5.2 Introduction

As mentioned earlier in chapter 1, MOX type gas sensors have suffered from the poor gas selectivity issue. The poor gas selectivity issue is a common, long-standing issue for most of the chemiresistor type gas sensors. In general, the selectivity of chemiresistor type gas sensors are improved through chemical functionalization process. When multiple gas sensors are functionalized with different materials, e.g., different noble metals, the gas sensors may exhibit different sensitivity against the same gas. Some of the gas sensors may show stronger sensitivity against a particular gas compared with other gases. In this case, the gas sensors may be used to detect the gas with the strong response as the target gas. When the sensitivity to the target gas is defined as $S_{\text{target}}$, the selectivity to other gases, say gas $A$, may be expressed as $S_{\text{target}}/S_{\text{A}}$. This definition of selectivity may be called *relative selectivity*, while the wavelength specific selectivity of optical type gas sensors may be called *absolute selectivity*. Most of the existing chemiresistor type gas sensors, including MOX type, rely on the relative selectivity to distinguish a particular target gas. The concept is straightforward; however, the gas sensors relying on the relative selectivity have a critical potential issue. The issue is that, as long as the gas sensors have non-zero sensitivity to non-target gases, the detected gas cannot be identified. For example, low concentration of a target gas and high concentration of a non-target gas may end up with more or less the same output signals. Therefore, in order to identify the detected gas using the gas sensors based on the relative selectivity, we have to obtain additional information. In addition, it is hard to predict how the chemical functionalization process modulates the sensitivity to various non-target gases. Hence, chemical funcitoanlization processes tend to involve a lot of trial and errors, thereby they tend to be inefficient development processes. From a point of view of signal processing, the core issue of the gas sensors relying on the relative selectivity is tied with the scalar valued output signals. In general, scalar value itself cannot hold any physical information of the detected gases except the gas concentration. Hence, the selectivity is inherently limited.

On the other hand, the key concept of e-nose is the multi dimensional vector valued output signals which allow us to extract some characteristic features associated with the detected gases. The gas selectivity realized by e-nose approach may be called *analytical selectivity* in this dissertation as the concept clearly differs from relative/absolute selectivity.

As mentioned in section 1.4, various e-nose have been developed in the past, while majority of them are with more or less the same strategy. Most of the early-stage e-nose have been made by assembling multiple commercial MOX type gas sensors. Therefore, they tend to be bulky and power-hungry. Later, miniaturized MOX type gas sensor arrays integrated with micro hotplates were developed by utilizing MEMS fabrication technologies; however, it is challenging to implement the chemical functionalization processes into the batch fabrication process. Hence, the remaining challenge of e-nose is to establish a scheme to obtain multi dimensional vector valued output signals in a cost efficient and reproducible manner.

Here, we propose a novel e-nose by using a single GFET aiming to achieve analytical selectivity, miniaturization, low cost, and low power consumption. While the dimensionality of the vector valued output signals of the conventional e-nose are limited by the number of chemicals which sensitize the sensor elements, that of the proposed e-nose is determined by the physical properties of GFET. The proposed scheme is described below.

As introduced in section 2.3, the conductivity of GFETs can be modulated by applying the gate voltage, and the characteristic V-shaped profile can be obtained (Fig. 2.7). The measured conductivity profiles are associated with the physical properties of graphene, the carrier concentration $n_{e/h}$, the carrier mobility $\mu_{e/h}$, and the residual carrier concentration $n^*$, via Eq. (2.25), Eq. (2.26), and Eq. (2.29). Given that the asymmetric carrier mobility $\mu_e \neq \mu_h$ [48, 58, 59] as mentioned earlier in subsection 2.4.3, the relationships may be re-written as

$$\mu_e = \frac{1}{c_g} \frac{\Delta \sigma_e}{\Delta V_G} \tag{5.1}$$

$$n_{e/h} = \frac{c_g}{e} |V_{NP}| \tag{5.2}$$

$$\mu_h = \frac{1}{c_g} \frac{|\Delta \sigma_h|}{\Delta V_G} \tag{5.3}$$

$$\frac{n^*}{n_{imp}} \approx \frac{1}{20} \frac{h}{e^2} \sigma_0 \tag{5.4}$$

where $c_g$ is the gate capacitance per unit area given by $c_g = \varepsilon_0 \varepsilon_{SiO_2}/t_{ox} \approx 1.15 \times 10^{-8}$ C/(V· cm$^2$) (where $\varepsilon_0 = 8.854 \times 10^{-14}$ C/(V· cm), $\varepsilon_{SiO_2} = 3.9$, $t_{ox} = 3 \times 10^{-5}$ cm), $e$ is the elementary charge, $1.602 \times 10^{-19}$ C, $V_{NP}$ is the gate voltage at the charge neutrality point (NP) where the conductivity $\sigma$ $1/\Omega$ becomes its minimum value $\sigma = \sigma_0$, $h$ is Planck constant given by $h = 4.135 \times 10^{-15}$ eV·s, $n^*$ is the residual carrier concentration, and $n_{imp}$ is the charged impurities concentration. These four equations suggest that the measurable quantities appearing on the right hand side may be converted to the four distinctive physical properties of GFETs on the left hand side. These physical properties are influenced by the gas molecules on the surface of graphene [48, 49, 57] with holding gas-specific information, such as the charge magnitude and/or dipole moment of gas molecules [57, 59].

Figure 5.1 illustrates the measurable quantities in a conductivity profile versus the gate voltage of a GFET and the corresponding physical phenomena on the graphene channel. When gas molecules approach the graphene, positive or negative charge transfer can occur

between the gas molecules and graphene depending on the relationship of the electron energy level as explained in subsection 2.4.2, which shifts the lateral position of the charge neutrality point (Fig. 5.1**a**). After that, gas molecules can generate the Coulomb potential to cause hole-gas interactions and modulated hole mobility to induce the slope change in the hole-branch of the conductivity profile (Fig. 5.1**b**). Similarly, the carrier mobility may be modulated by the attractive Coulomb force to induce the slope change in the electron-branch of the conductivity profile (Fig. 5.1**c**). Near the charge neutrality point, the residual carriers and/or charged impurities can be influenced by the charged gas molecules such that the ratio, $n^*/n_{imp}$, may be modulated to change the minimum conductivity at the charge neutrality point (Fig. 5.1**d**). Our scheme is to utilize the four distinctive physical properties of a GFET as the four elements of multi dimensional vector valued output signals, i.e., 4-dimensional (4D) output vectors, say $\boldsymbol{q}$, defined as: $\boldsymbol{q}_1$ - the electron mobility $\mu_e$; $\boldsymbol{q}_2$ - the carrier concentration $n$; $\boldsymbol{q}_3$ - the hole mobility $\mu_h$; and $\boldsymbol{q}_4$ - the ratio of the residual carrier concentration to the charged impurity concentration $n^*/n_{imp}$. As such, the gas-specific information can be characterized on a 4D feature space and resolved with pattern recognition algorithms for selective gas sensing without multiple functional materials. In fact, the physical properties have been previously studied for gas sensing without using the 4D vector concept and machine learning scheme [48, 86].

We experimentally investigated the 4D vectors for $H_2O$ (humidity), methanol (MeOH), and ethanol (EtOH) to validate the analytical selectivity of the proposed scheme. By using a large number of data, our machine learning algorithm was able to classify the 4D vectors for different gases with high consistency and distinguish gas sensing patterns in different binary mixture conditions of $H_2O$ and other target gases.
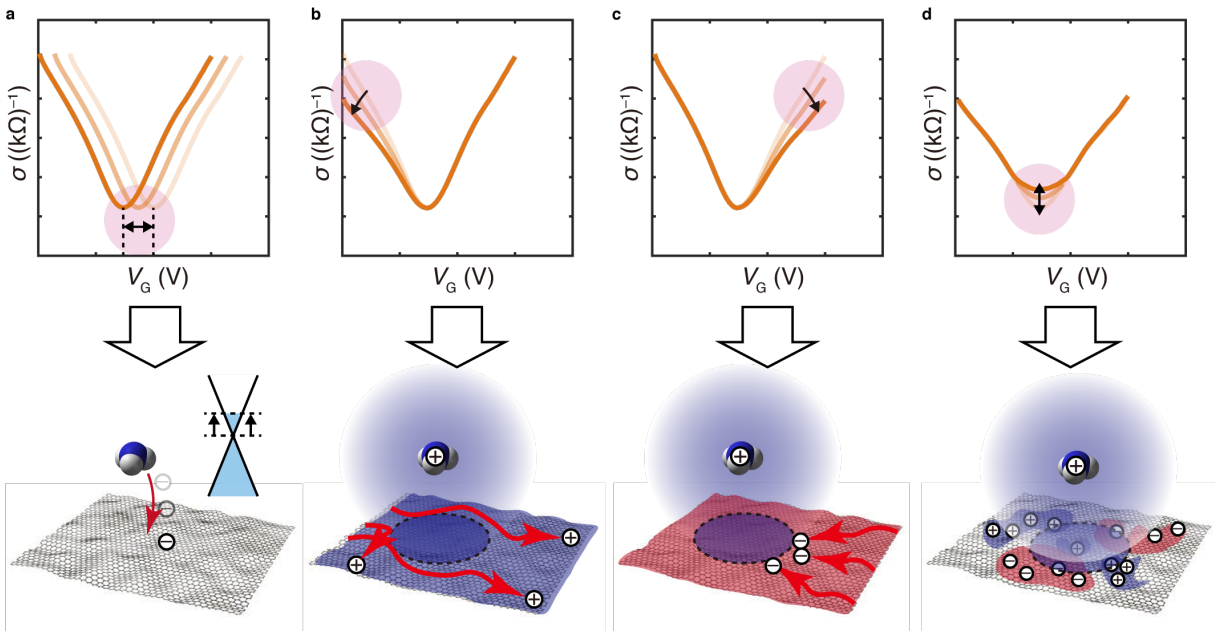
Figure 5.1: Schematic illustrations of the conductivity profiles versus the applied gate voltage and the corresponding physical phenomena over a GFET. (**a**, top) The gas molecule can cause the lateral movement of the conductivity profile and the movement of the charge neutral point; (**a**, bottom) the physical phenomenon of the charge transfer between a gas molecule and graphene and the carrier concentration change in the band diagram. (**b**, top) The slope in the hole branch can be altered due to the gas molecule; (**b**, bottom) the Coulomb interactions between the gas molecule and the holes. (**c**, top) The slope in the electron branch can be altered due to the gas molecule; (**c**, bottom) the Coulomb interactions between the gas molecule and the electrons. (**d**, top) The height of the charge neutral point is changed due to the gas molecule; (**d**, bottom) the modulated residual carrier concentration in the graphene.

## 5.3   Results

### 5.3.1   Measurement setup and experimental conditions

We prepared two different GFETs, a pristine-GFET and an atomic layer deposition (ALD) $RuO_2$ functionalized GFET (ALD-$RuO_2$-GFET) (details about the fabrication processes can be found in subsection 2.3.1 and 4.3.2 for pristine-GFET and ALD-$RuO_2$-GFET, respectively) for three different experiments using three types of gases: $H_2O$ (humidity), methanol (MeOH), and ethanol (EtOH). The two different types of GFETs are used to extend the dimension of the feature space from 4D to 8D to illustrate that the accuracy of the gas

classification results can be further improved with higher dimensionality. It is noted that the role of the functionalized GFET is to multiply the dimension of the output signals of a single GFET to $4 \times N$, where $N$ is the total number of the used GFETs. Hence, when the analytical selectivity is achieved by a single GFET, the functionalized GFET is not necessary. However, it is still worth to have more than two devices as the pattern recognition algorithm tends to be more robust at higher dimensionality. The dependence of the dimension on the gas classification accuracy will be discussed later. The fabricated pristine-GFET, the electrical configuration, and the characterization results are shown in Fig. 5.2. In the SEM image, the darker rectangle structure in the center is the graphene channel connected to the Au/Pd electrodes Fig. 5.2**a**. The electrical configuration is as the same as the one we used in previous chapters Fig. 5.2**b**. The conductivity profile versus the gate voltage (Fig. 5.2**c**) is converted to the initial four physical properties as shown in Fig. 5.2**d**. Three experimental setups, $A$ (Fig. 5.4**a**), $B$ (Fig. 5.6**a**), and $C$ (Fig. 5.11**a**) were conducted to study the repeatability of the classification algorithms (for setups $A$ and $B$) and the applicability of the scheme to binary mixtures (setup $C$), respectively. Throughout the study, we define the local repeatability as the repeatability within a single experimental data set (one measurement) and the global repeatability as the repeatability within multiple experimental data sets (multiple measurement). The specific gas type can be used as the variable, while the other parameters, e.g., the concentration and the process to produce the vapors are kept as the same. The same measurement setup (Fig. 5.3) and other common parameters were the same (see section 3.3) such that the variables are either the tested devices and/or the gas types.
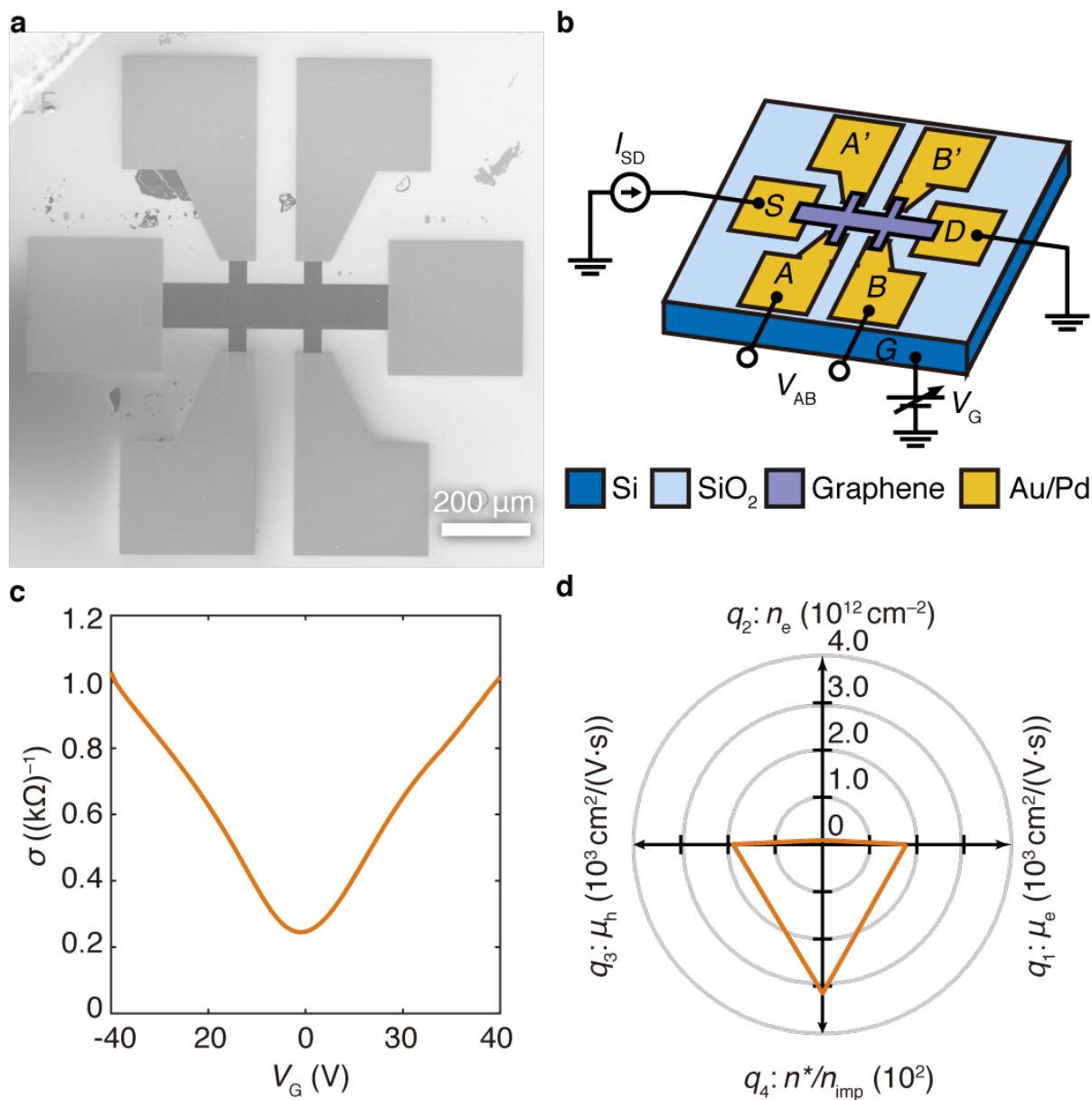
Figure 5.2: Characterization of the fabricated pristine-GFET. **a** SEM image of the fabricated pristine-GFET. **b** A typical electrical configuration of a GFET: $I_{SD}$ as a constant source-drain current $V_{AB}$ as the voltage across the two inner electrodes, $V_G$ as the gate voltage. **c** A conductivity profile versus gate voltage of the fabricated pristine-GFET in dry air. **d** The converted four physical properties from the conductivity profile (**c**).
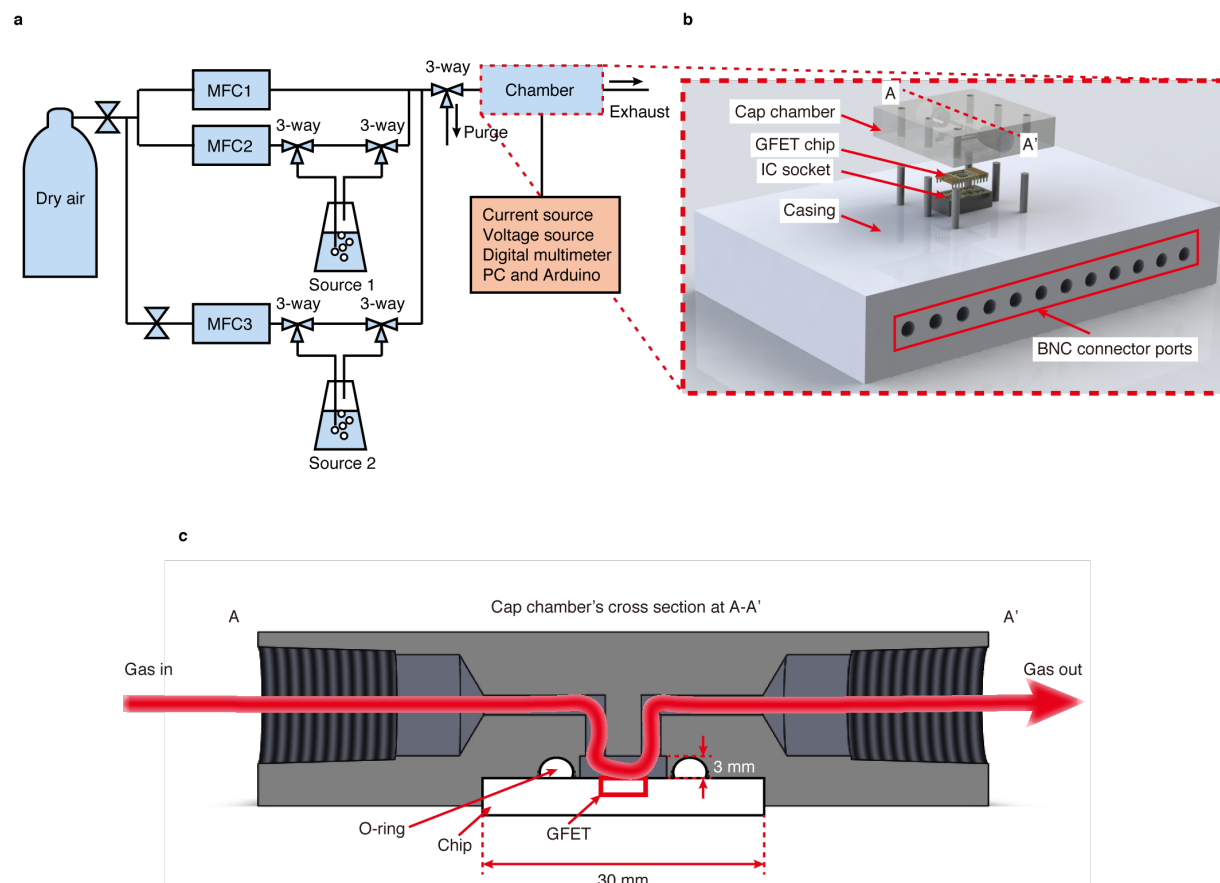
Figure 5.3: Schematic of the experiment setup of gas sensing. **a** Schematic of the gas control system comprising a dry air gas cylinder, three mass flow controller (MFC1, MFC2, and MFC3), two vapor sources, a gas chamber, power sources, and a control and data acquisition system. **b** Schematic of the gas chamber configuration comprising a cap chamber, a GFET test chip, an IC socket, a casing, and BNC connector ports. **c** Schematic of the cross sectional view of the cap chamber mounted on a GFET test chip, sealed with an O-ring.

## 5.3.2  Measurement results and the converted 4D and 3D vectors

The conductivity profiles versus gate voltage with respect to time on a pristine-GFET are recorded as shown in Figs. 5.4**b-d** for $H_2O$, MeOH, and EtOH, respectively. It is observed that the responses of the sensor to EtOH is small, while the responses to $H_2O$ and MeOH are relatively large and clear. These conductivity profiles were converted to 4D and 3D vectors (Figs. 5.4**e-j**) based on the proposed scheme with the relevant equations (Eqs. 5.1-5.4) and the vectors are normalized such that one can focus on the relative changes. Specifically, the 3D vectors (Figs. 5.4**h-j**) excluded the carrier concentration change in the 4D vectors in order to visualize the results in a 3D feature space. Furthermore, it is useful to define the

sensitivity vector, i.e., the gas sensing pattern, $\boldsymbol{q}_s(t) = 100 \times (\boldsymbol{q}(t) - \boldsymbol{q}_0)/\boldsymbol{q}_0$ (%), where $\boldsymbol{q}(t)$ is a 4D or 3D vector, and $\boldsymbol{q}_0$ is an initial or reference vector by using the conductivity profiles at the time right before the first gas exposure cycle starts. Similarly, the measurement results of the pristine-GFET for the setup $B$, the ALD-RuO$_2$-GFET for the setup $A$ and $B$ is shown in Fig. 5.5, Fig. 5.6, and Fig. 5.7, respectively.
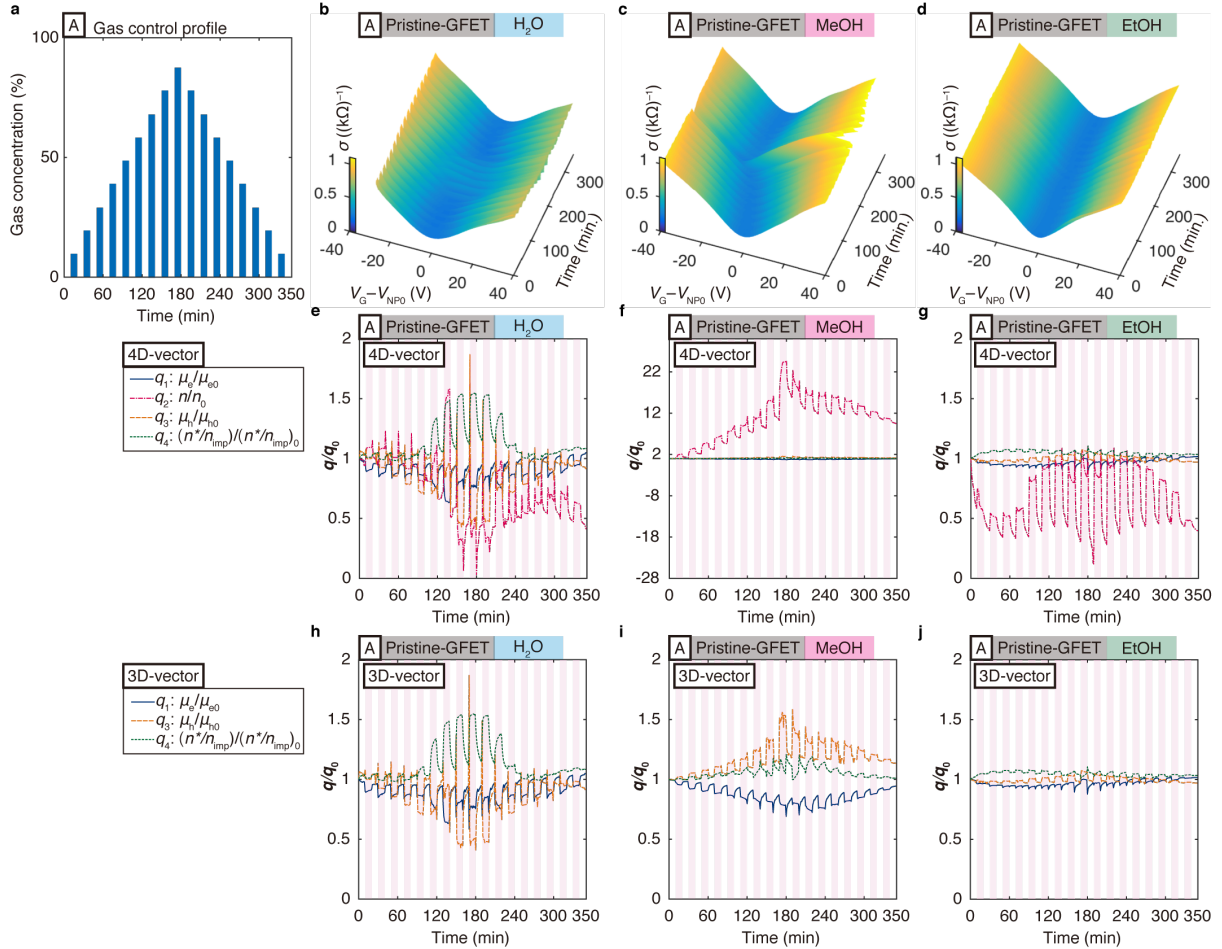


Figure 5.4: Measurement results and the converted transient 4D and 3D vectors using setup $A$ with the pristine-GFET. **a** Gas concentration profile in test setup $A$. **b-d** Transient conductivity profiles versus gate voltage with respect to time for H$_2$O (humidity), methanol (MeOH), and ethanol (EtOH). **e-g** Relative magnitude of the converted 4D vectors versus time. **h-j** Relative magnitude of the 3D vectors by removing the carrier concentration vector in the 4D vectors.
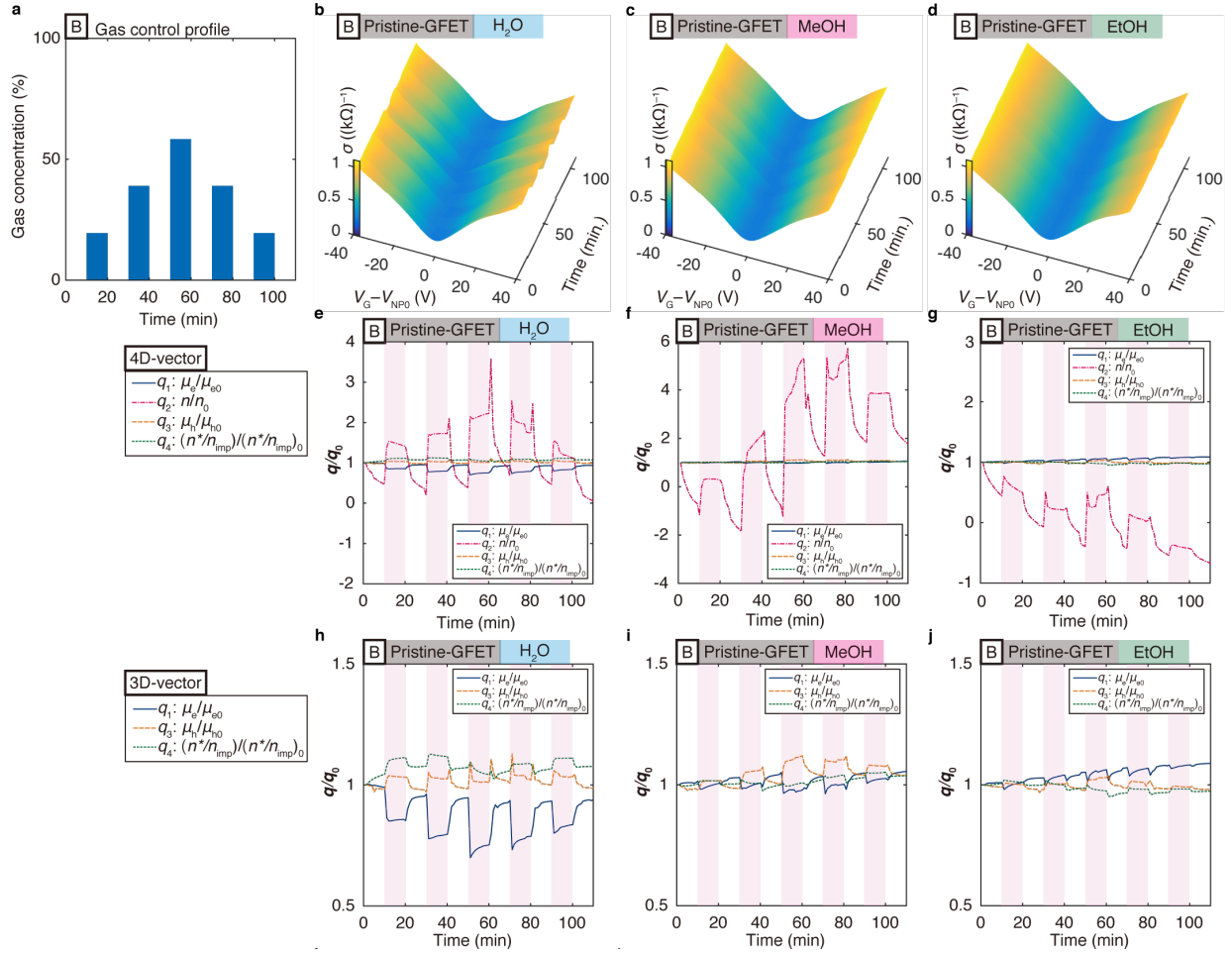
Figure 5.5: Measurement results and the converted transient 4D and 3D vectors using setup $B$ with the pristine-GFET. **a** Gas concentration profile in test setup $B$. **b-d** Transient conductivity profiles versus gate voltage with respect to time for $H_2O$ (humidity), methanol (MeOH), and ethanol (EtOH). **e-g** Relative magnitude of the converted 4D vectors versus time. **h-j** Relative magnitude of the 3D vectors by removing the carrier concentration vector in the 4D vectors.
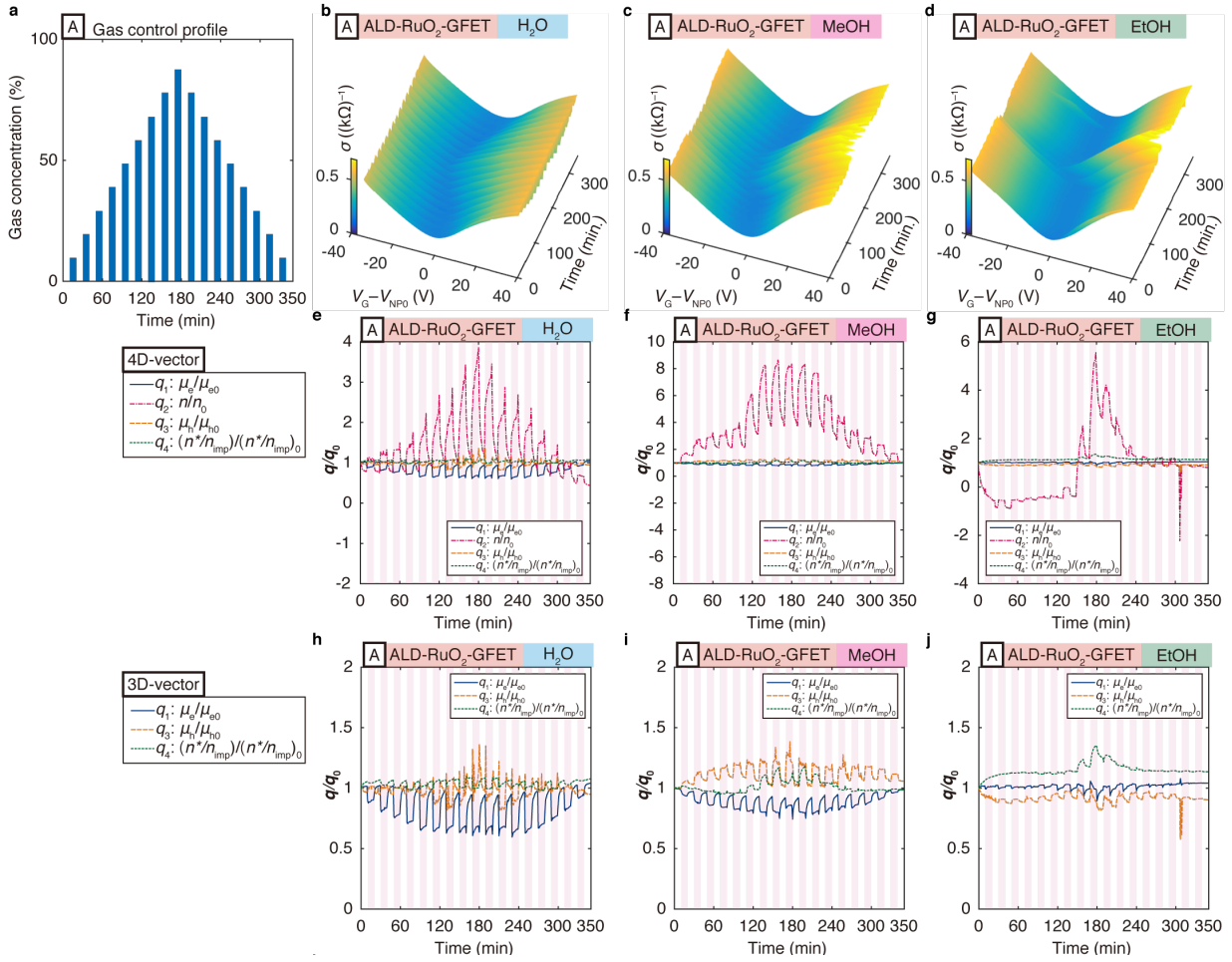
Figure 5.6: Measurement results and the converted transient 4D and 3D vectors using setup $A$ with the ALD-RuO$_2$-GFET. **a** Gas concentration profile in test setup $A$. **b-d** Transient conductivity profiles versus gate voltage with respect to time for H$_2$O (humidity), methanol (MeOH), and ethanol (EtOH). **e-g** Relative magnitude of the converted 4D vectors versus time. **h-j** Relative magnitude of the 3D vectors by removing the carrier concentration vector in the 4D vectors.
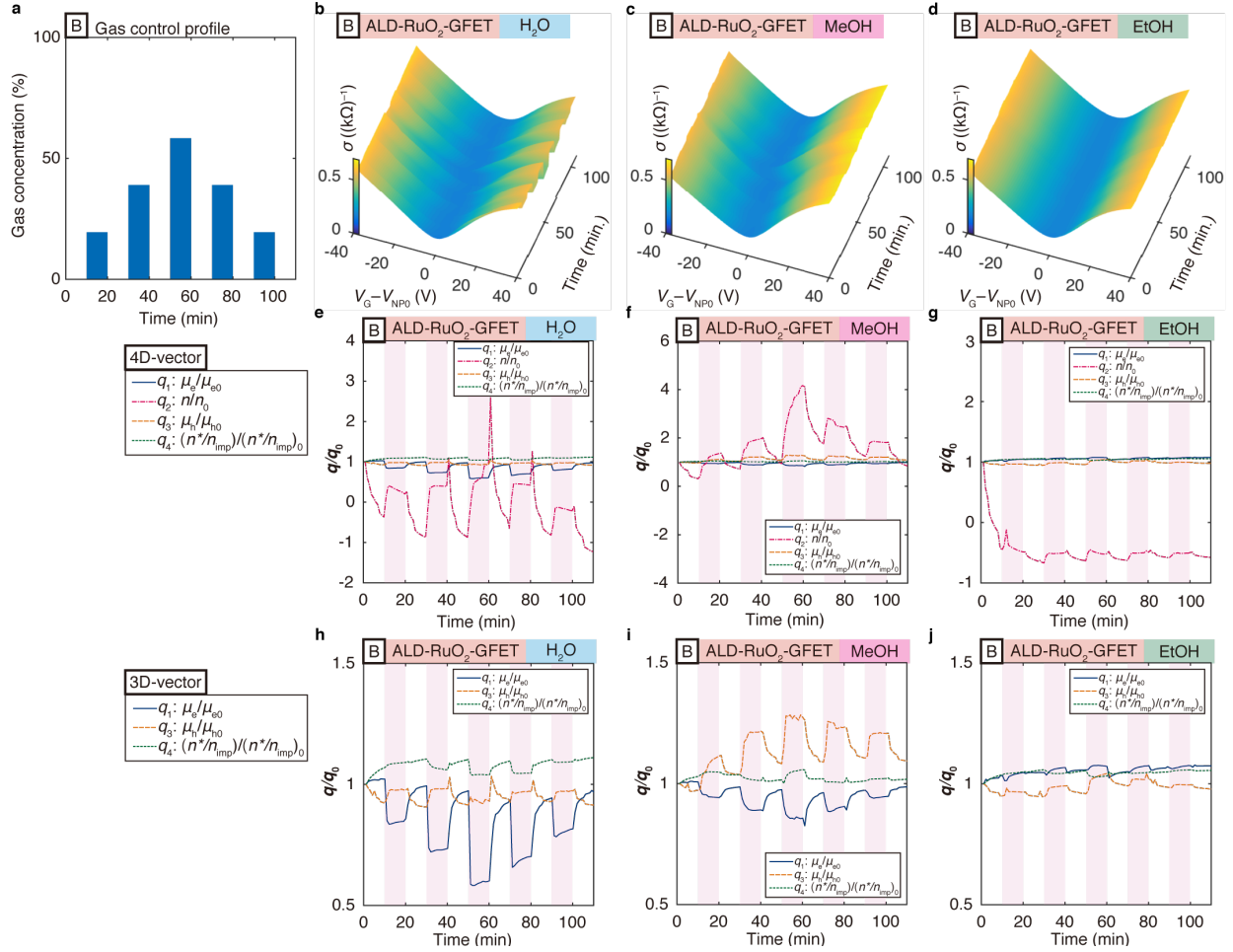
Figure 5.7: Measurement results and the converted transient 4D and 3D vectors using setup $B$ with the ALD-RuO$_2$-GFET. **a** Gas concentration profile in test setup $B$. **b-d** Transient conductivity profiles versus gate voltage with respect to time for H$_2$O (humidity), methanol (MeOH), and ethanol (EtOH). **e-g** Relative magnitude of the converted 4D vectors versus time. **h-j** Relative magnitude of the 3D vectors by removing the carrier concentration vector in the 4D vectors.

Two different 3D gas sensing patterns were generated and characterized: (1) gas sensing patterns representing only the ascending cycles in which the gas concentration increases from 10% to 90%; (2) gas sensing patterns enclosed by triangulated boundaries representing both the ascending and the descending (from 80% to 10%) cycles. The first pattern is utilized to examine and validate the raw data points and the second pattern is to visualize the distinctive regions for different gases. The representative 2D planes for the pristine-GFET are shown in Figs. 5.8**a-c** for the first patterns and Figs. 5.8**d-f** for the second patterns. Figures 5.8**a-c** show that the gas sensing patterns have consistent trends with good local repeatability. Figures 5.8**d-f** indicate that the gas sensing patterns are distinctive in terms

of their locations in the 3D feature space. These qualitative analyses agree with the results from the setup $B$ (Figs. 5.8**g-i**) and the results using the ALD-$RuO_2$-GFET (Fig. 5.9), implying the high global repeatability. These results suggest that the tested gas types can be classified qualitatively by using the gas sensing patterns.
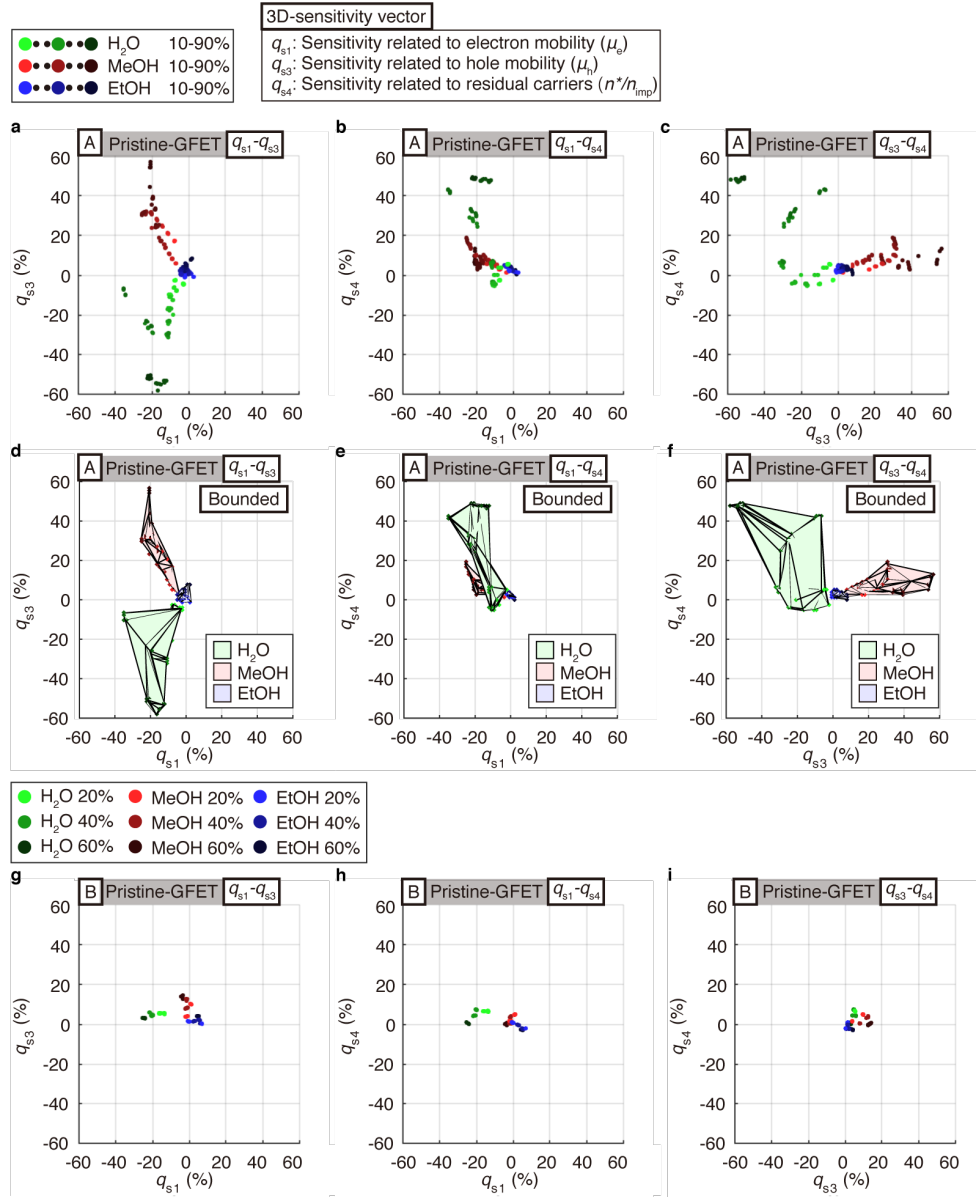
Figure 5.8: 3D gas sensing patterns for the pristine-GFET projected onto 2D planes. **a-c** 3D gas sensing patterns for the ascending (from 10% to 90%) cycles projected onto three representative 2D planes for setup $A$. **d-f** 3D gas sensing patterns enclosed by triangulated boundaries for both the ascending (from 10% to 90%) and the descending (from 80% to 10%) cycles projected onto three representative 2D planes for setup $A$. **g-i** 3D gas sensing patterns for the ascending (from 20% to 60%) cycles projected onto three representative 2D planes for setup $B$.
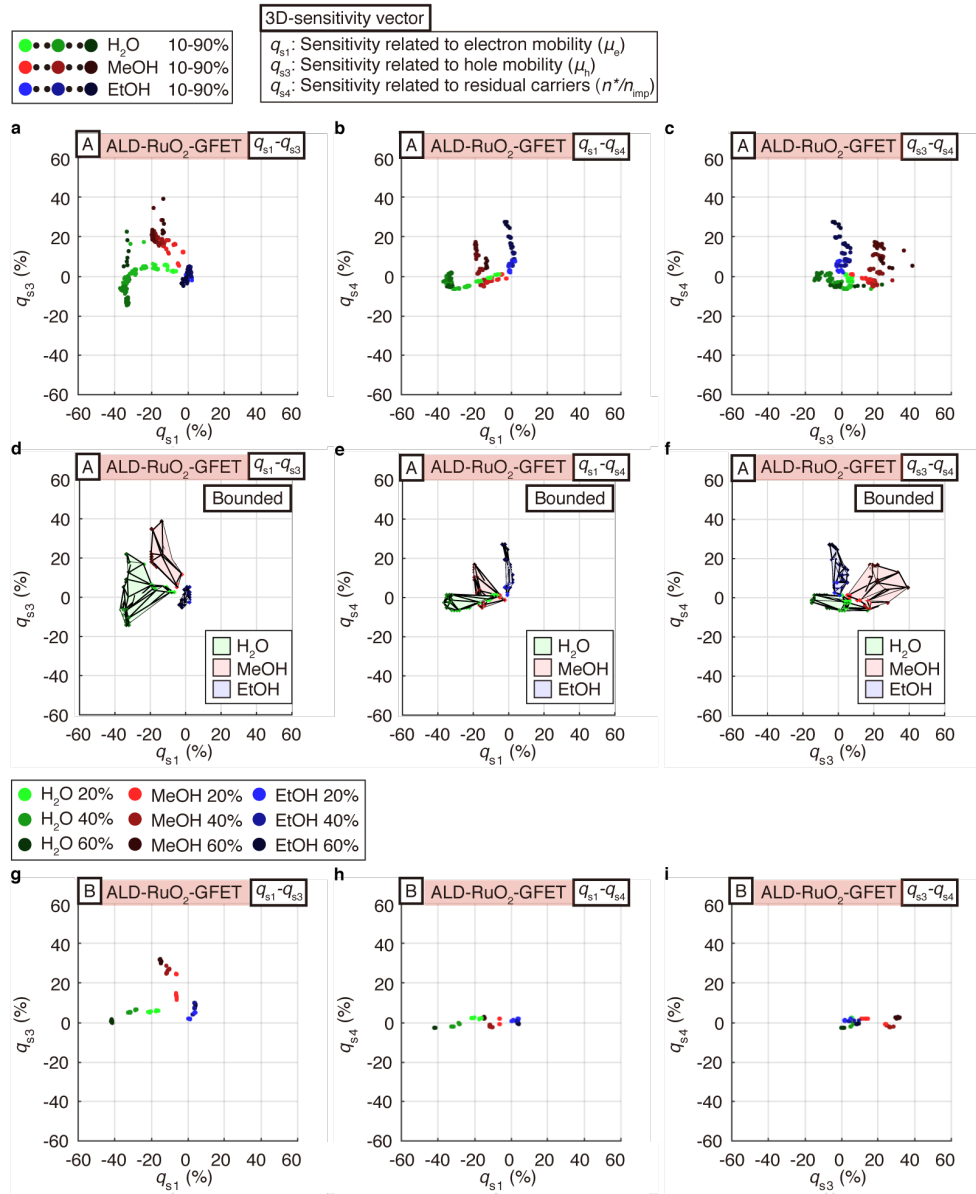
Figure 5.9: 3D gas sensing patterns for the ALD-RuO$_2$-GFET projected onto 2D planes. **a-c** 3D gas sensing patterns for the ascending (from 10% to 90%) cycles projected onto three representative 2D planes for setup $A$. **d-f** 3D gas sensing patterns enclosed by triangulated boundaries for both the ascending (from 10% to 90%) and the descending (from 80% to 10%) cycles projected onto three representative 2D planes for setup $A$. **g-i** 3D gas sensing patterns for the ascending (from 20% to 60%) cycles projected onto three representative 2D planes for setup $B$.

The gas concentration dependence on the decoupled physical properties is summarized in Fig. 5.10. While most results show nearly linear relationships, some of them are non-linear. Theoretically, the field effect mobility should be inversely proportional to the gas concentration, while the carrier concentration should have linear dependency. The non-linear behavior of the carrier concentration change, pronouncedly observed in the EtOH results, may be related to the interactions between EtOH and the pre-existing charged impurities. Despite the non-linearity of the gas concentration dependence, the gas sensing patterns are qualitatively distinguishable as their locations in the feature space are different from each other. These results suggest that the gas concentration may be better obtained by using another GFET with the constant gate voltage scheme, while the selectivity can be readily achieved by the proposed scheme. The gas classification capability is discussed further in a later section.
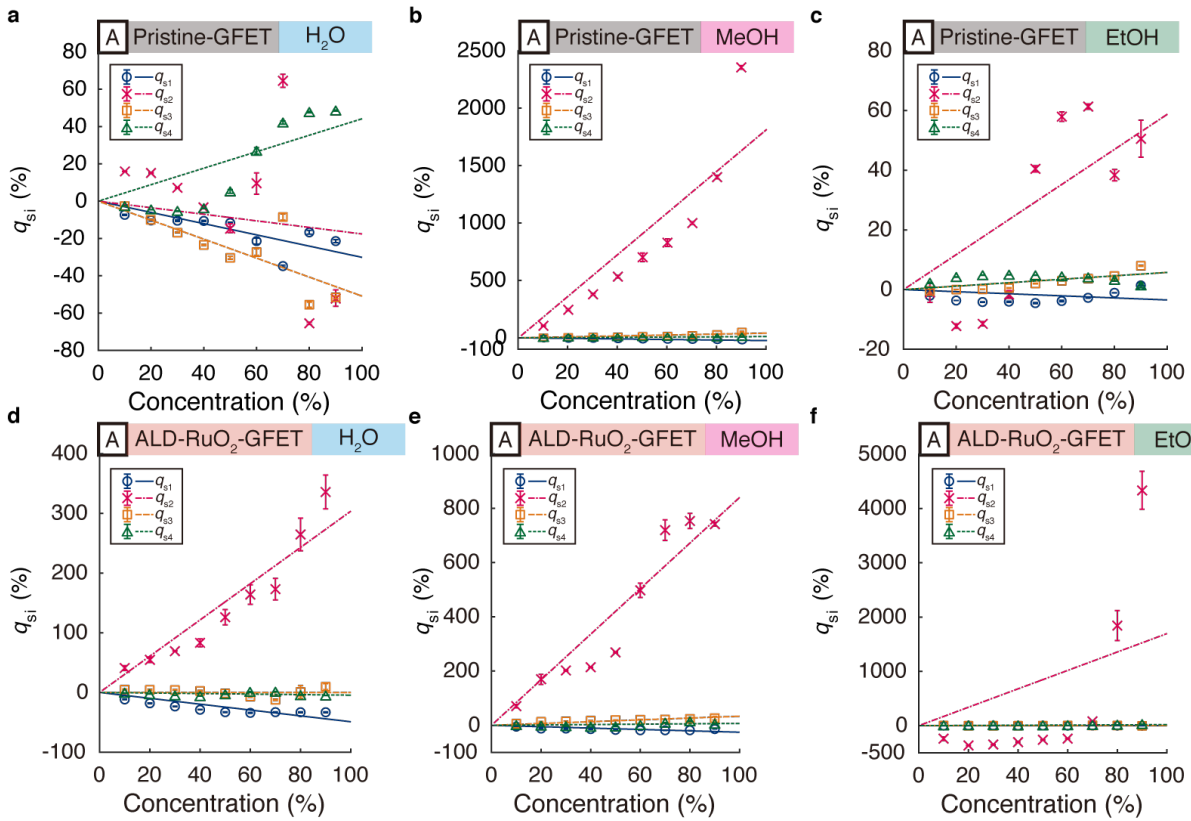


Figure 5.10: Gas concentration dependence on each physical property in setup $A$. **a-c** Gas concentration dependence of pristine-GFET for $H_2O$ (humidity), methanol (MeOH), and ethanol (EtOH). **d-f** Gas concentration dependence of ALD-RuO$_2$-GFET for $H_2O$ (humidity), methanol (MeOH), and ethanol (EtOH).

### 5.3.3 Gas sensing patterns of binary gas mixtures

We are interested in distinguishing the gas sensing patterns from the ambient air with background humidity as humidity can be a problem for GFET-based gas sensors operated at room temperature as discussed in chapter 3. We used setup $C$ (Fig. 5.11**a**) by varying the relative humidity (R.H.) level stepwise (red color bars), 0%, 20%, 40%, and 60%, with three purge-exposure cycles of the carrier gas (blank), MeOH, and EtOH as the target gases (blue color bars) for each R.H. level. The carrier gas was used as a blank target gas, i.e., negative control, which may only cause non-gas related signals. Therefore, the corresponding gas sensing patterns are considered to represent the background humidity level only in this particular setup. As the same as setup $A$ and $B$, the conductivity profiles (Figs. 5.11**b-d**) and the converted 4D and 3D vectors (Figs. 5.11**e-j**) are shown for pristine-GFET. The 3D gas sensing patterns of the three binary gas mixtures of (1) $H_2O$ and the carrier gas (blank), (2) $H_2O$ and MeOH, and (3) $H_2O$ and EtOH were generated for each experiment and merged into a shared 3D feature space represented by green, red and blue color markers, respectively (Figs. 5.11**k-m**). In Fig. 5.11**k**, the gas sensing patterns are grouped by light blue color regions based on the corresponding background R.H. levels. In order to obtain the gas sensing patterns, the reference vector, $q_0$, was defined as the vector at 10 minutes, which is the time right before the first gas exposure cycle starts. All $q(t)$ were taken from the gas exposure cycles (blue color bars) such that the obtained gas sensing patterns reflect the information of both the target gas and the background R.H. level. Results show that the gas sensing patterns, especially for MeOH (red color markers), can be distinguished visually from the one with the background humidity only (green color markers) in Fig. 5.11**k**. In general, the gas sensing patterns for the background humidity shift from the center to the bottom left as the R.H. level increases, while the gas sensing patterns for MeOH shift to the upper side. Interestingly, the trends here qualitatively agree with the results in Fig. 5.8**a**, suggesting that the gas sensing patterns in the binary gas mixture can be related to the superposition of the individual gas sensing patterns which are obtained from separate tests. The similar trends are found for those using the ALD-$RuO_2$-GFET (Fig. 5.12).
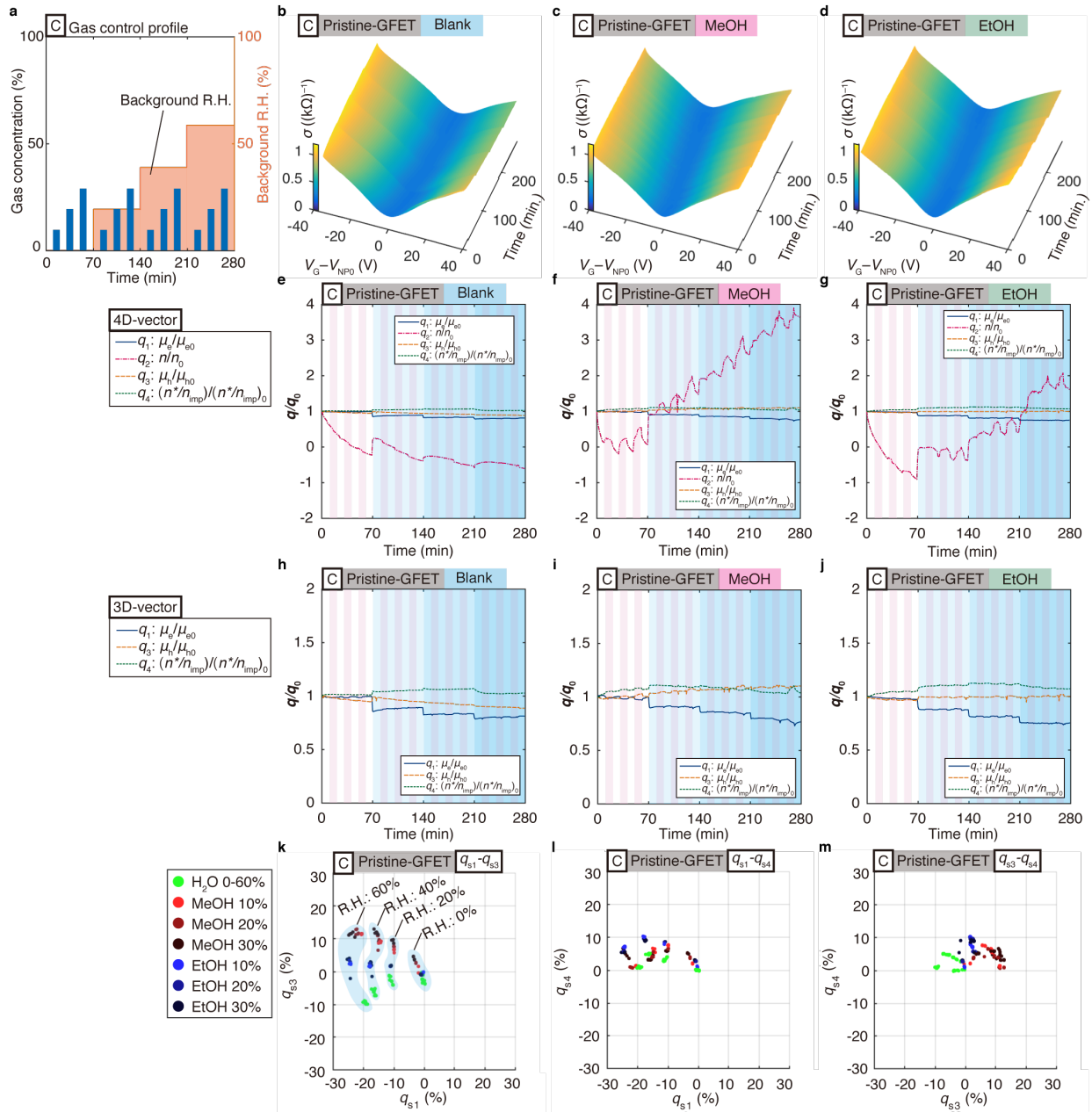
Figure 5.11: Measurement results and the converted transient 4D and 3D vectors and the 3D gas sensing patterns projected onto 2D planes in experiment set $C$ with the pristine-GFET. **a** Gas concentration profiles of the target gases in setup $C$. **b-d** Transient conductivity profiles versus gate voltage with respect to time for blank ($H_2O$ (humidity) background only), methanol (MeOH), and ethanol (EtOH) vapors. **e-g** Relative magnitude of converted 4D vectors versus time; **h-j** and relative magnitude of 3D vectors by removing the carrier concentration vector in the 4D vectors. **k-m** 3D gas sensing patterns projected onto three representative 2D planes.
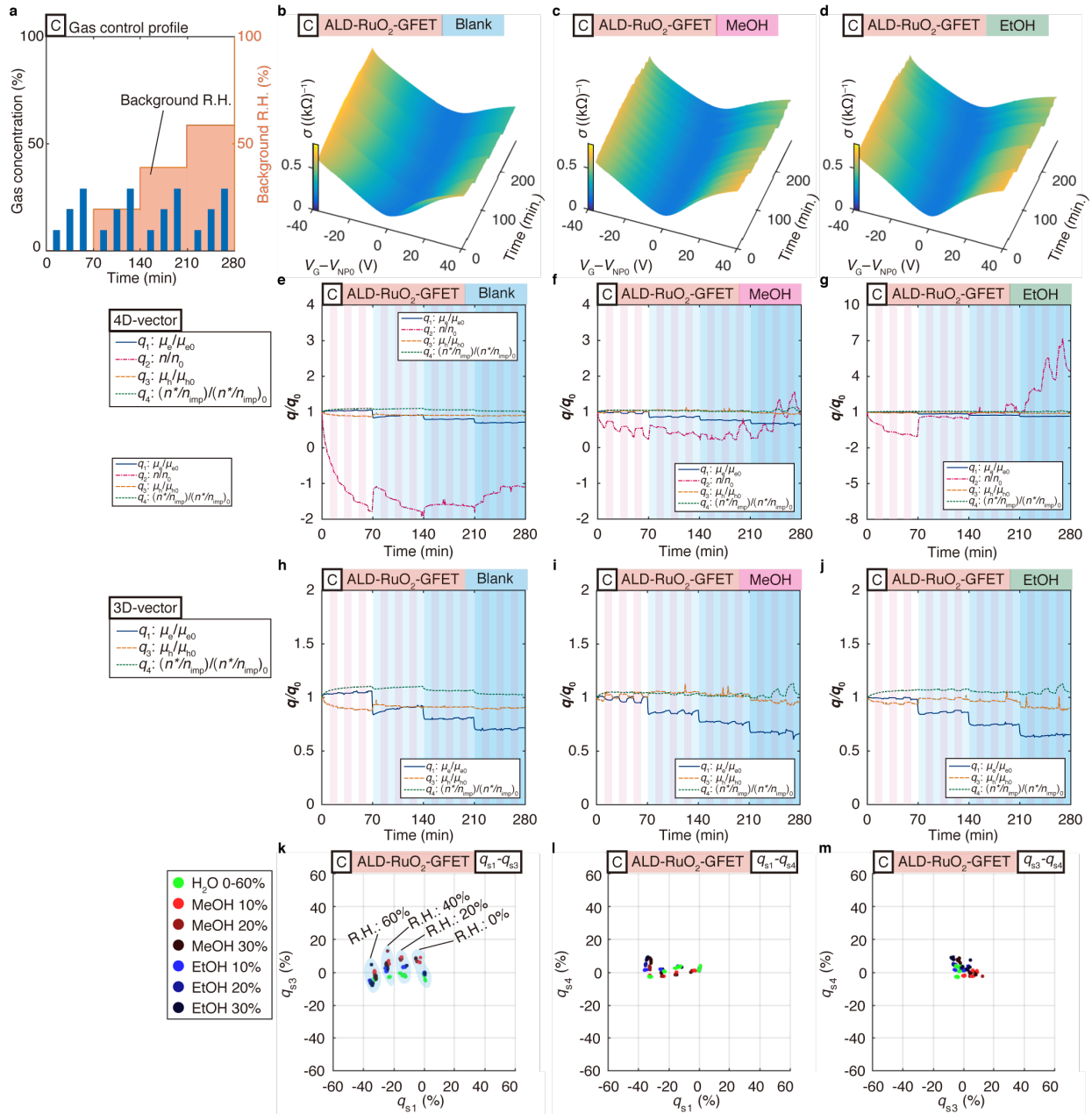
Figure 5.12: Measurement results and the converted transient 4D and 3D vectors and the 3D gas sensing patterns projected onto 2D planes in experiment set $C$ with the ALD-RuO$_2$-GFET. **a** Gas concentration profiles of the target gases in setup $C$. **b-d** Transient conductivity profiles versus gate voltage with respect to time for blank (H$_2$O (humidity) background only), methanol (MeOH), and ethanol (EtOH) vapors. **e-g** Relative magnitude of converted 4D vectors versus time; **h-j** and relative magnitude of 3D vectors by removing the carrier concentration vector in the 4D vectors. **k-m** 3D gas sensing patterns projected onto three representative 2D planes.

### 5.3.4 Classification of the gas sensing patterns by using machine learning analyses.

A supervised machine learning analysis was conducted to classify the gas sensing patterns empirically. In this analysis, we examined both pristine- and ALD-RuO$_2$-GFET with the two setups, $A$ and $B$. The goal is to distinguish three gas types, H$_2$O, MeOH, and EtOH, by adopting a multi-class classification model. A multi-layer perceptron classifier with a feed-forward neural network architecture was implemented and trained by using data from the two GFETs [27]. In order to avoid the overfitting phenomenon, which occurs when a machine learning model undergoes too much training and even fits to random noises such that it fails to capture a generalized trend, a cross-validation test was performed. In general, the entire data were randomly shuffled several ways and separated via a stratified split, of which 20% were reserved as the testing set and the remaining constituted the training set. A stratified split ensures that each target class is adequately represented in either set. Data reserved as the testing set during each shuffle were scored by their corresponding neural network model.

Once the machine learning models were trained, the confusion matrices (Fig. 5.13**a** for pristine-GFET and Fig. 5.13**d** for ALD-RuO$_2$-GFET) compared the predicted labels of the testing data to their true labels. The numbers in the matrices convey the percentages of samples that were distributed among their associated label of prediction. The accuracies of the pristine-GFET device and ALD-RuO$_2$-GFET device were 96.2% and 100%, respectively. The cross-validation results indicated that the pristine-GFET device had a mean accuracy of 95.4% and a standard deviation of 2.5%, while the ALD-RuO$_2$-GFET device had a mean accuracy of 99.6% and a standard deviation of 0.8%. Figs. 5.13**b&e** show the accuracy and cross entropy loss history as the neural networks underwent epochs of training to minimize the loss function. A visible asymptotic state after 40 epochs implies that the model had approached convergence and further training would not significantly improve the performance. The ALD-RuO$_2$-GFET device demonstrated a higher training accuracy than that of the pristine-GFET device, which echoes their difference in classification capability mentioned above. After merely 40 epochs of training, the neural network model trained for samples measured by the ALD-RuO$_2$-GFET device was able to predict 99.1% of the training data and the time required for 40 epochs of training was 0.0519 seconds.

The impact of dimension to the accuracy of the model was evaluated as shown in Figs. 5.13**c&f**. For 2D and 3D models, one can choose any two out of the four features and any three out of four features for analyses, respectively. The 1D model is excluded as the scalar value cannot generate any characteristic feature. For the pristine-GFET (Fig. 5.13**c**) device, different combinations of features could yield high accuracies in either 2D or 3D models as compared with that of the 4D model. For the ALD-RuO$_2$-GFET (Fig. 5.13**f**) results, three out of the four possible combinations in the 3D model yield 100% accuracy. By combining the features of the pristine-GFET and the ALD-RuO$_2$-GFET devices, an 8D model can be constructed. Since the accuracy of the ALD-RuO$_2$-GFET device can reach close to 100% with four features, the pristine-GFET device's 4D feature array was set as the starting point

as more features from the ALD-RuO$_2$-GFET device are added. As shown in Fig. 5.13**c** (red markers), adding more dimensions can result in higher accuracies as compared to that of the 4D model. These results validate the classification capability of the multi-dimensional gas sensing patterns of GFETs and suggest that an improved accuracy can be achieved by expanding the feature space to higher dimensions.

The accuracy variations in lower dimension (2D and 3D) models imply that some features have stronger influences to the classification study. Here, the importance of the eight features (for two GFETs) are investigated by employing the one-way ANOVA (analysis of variance) F-test scheme, which can rank the importance of features [87]. The F-statistic is defined as the ratio of the treatment sum of squares (SST) to the sum of squares error (SSE), scaled by their respective degree of freedoms. For a feature matrix of $q$ rows by $m$ columns, the F-statistic is expressed as

$$F = \frac{\sum_{i=1}^{m} \frac{n_i(\bar{Y}_i - \bar{\bar{Y}})^2}{m-1}}{\sum_{i=1}^{m} \sum_{j=1}^{n_i} \frac{n_i(Y_{ij} - \bar{Y}_i)^2}{m(q-1)}} \tag{5.5}$$

where $n_i$ represents the number of observations within feature $i$; $\bar{Y}_i$ represents the mean of feature I; $\bar{\bar{Y}}$ represents the grand mean of the entire matrix; and $Y_{ij}$ represents the $j$-th entry of feature $i$. Converting the F-statistic to a p-value by referring to the F-distribution, one either accepts or rejects the null hypothesis which argues that any variation observed between features is likely due to randomness. For p-values less than a significance level of $\alpha = 0.05$, the null hypothesis is rejected and the corresponding feature is considered informative. The feature with the smallest p-value was considered most important. Table 5.1 ranks the eight collective features of both sensor devices from best to worst according to the calculated p-values. Figure 5.13**g** qualitatively compares feature importance by taking the negative log on the p-value column in Table 5.1, and then normalizing by the most important feature. According to Table 1, all eight features had p-values less than 0.05, which suggested that all features were in fact statistically informative to the outcome of the classification study. It is evident that the electron field effect mobility ($\mu_e$) of both GFETs are more important than others, while the ratio of the residual carrier concentration to the charged impurity concentration ($n^*/n_{imp}$) of the pristine-GFET is the least important. Therefore, the variations in the dimension dependence on the accuracy in the lower dimensions are indicative of the difference in importance between the tested features.
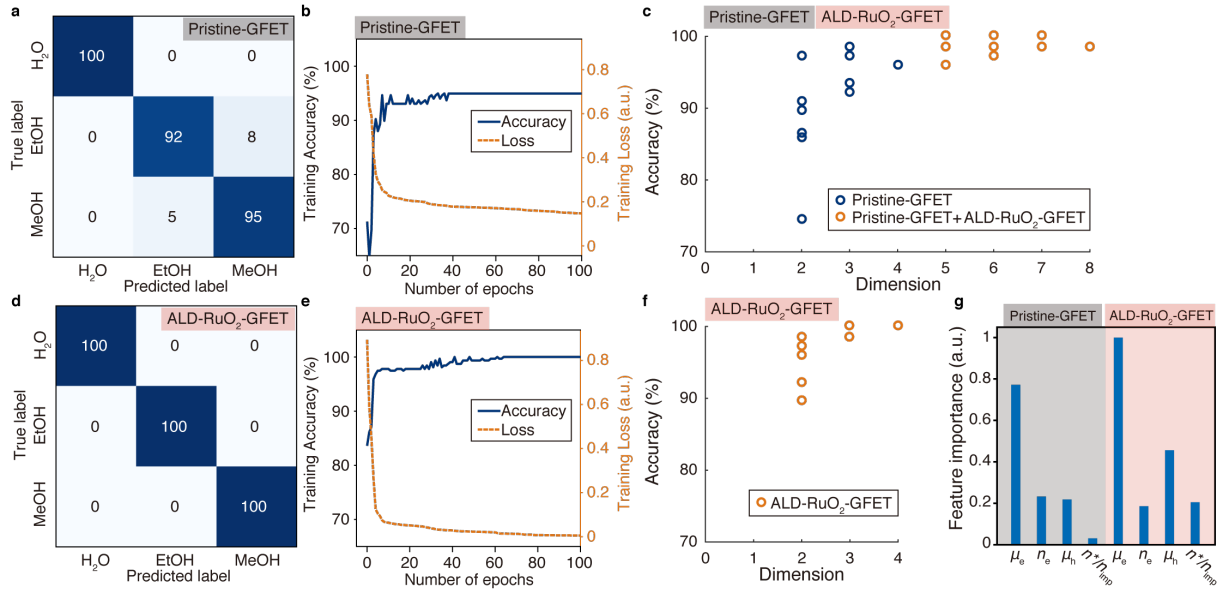
Figure 5.13: Classification of the gas sensing patterns using the machine learning analysis over two different experimental data sets from two different types of GFETs. **a** Confusion matrix of multi-class classification from results using the pristine-GFET. **b** History of the training accuracy and the training loss from results using the pristine-GFET. **c** Dimensionality dependence on the accuracy of the prediction from results using the pristine-GFET for up to four dimensions, with added dimensions from results using the ALD-RuO$_2$-GFET. **d-f** The same analysis as **a-c** from results using the ALD-RuO$_2$-GFET. **g** Normalized feature importance with respect to the tested eight features. The four features on the left correspond to the pristine-GFET and the others on the right correspond to the ALD-RuO$_2$-GFET.

| Importance rank | Feature name | F-statistic | P-value |
|---|---|---|---|
| 1 | Electron mobility ($\mu_e$) of the ALD-RuO$_2$-GFET | 1480.34 | $1.08 \times 10^{-183}$ |
| 2 | Electron mobility ($\mu_e$) of the pristine-GFET | 831.58 | $6.07 \times 10^{-142}$ |
| 3 | Hole mobility ($\mu_h$) of the ALD-RuO$_2$-GFET | 325.78 | $3.78 \times 10^{-84}$ |
| 4 | Carrier concentration ($n$) of the pristine-GFET | 127.35 | $2.31 \times 10^{-43}$ |
| 5 | Hole mobility ($\mu_h$) of the pristine-GFET | 117.56 | $9.59 \times 10^{-41}$ |
| 6 | The ratio ($n^*/n_{imp}$) of the ALD-RuO$_2$-GFET | 108.68 | $2.69 \times 10^{-38}$ |
| 7 | Carrier concentration ($n$) of the ALD-RuO$_2$-GFET | 96.44 | $8.37 \times 10^{-35}$ |
| 8 | The ratio ($n^*/n_{imp}$) of the pristine-GFET | 13.38 | $2.39 \times 10^{-6}$ |

Table 5.1: Summary of one-way ANOVA F-test, ranked in descending order of feature importance

## 5.4   Discussion

Compared to other approaches, such as non-scalable device fabrication, special functional materials, and bulky peripheral optical systems [88–91], this work presents a practical approach to address selectivity, miniaturization, low cost, and low power consumption issues at the same time. Here, we discuss the origin of the unique gas sensing patterns. Previous studies have suggested that the electrical properties of GFETs can be dictated by the charged impurities concentration, $n_{imp}$, through the following relationship (together with Eq. (5.4)) [48]

$$\sigma(n) = Ce\left|\frac{n}{n_{imp}}\right| + \sigma_0 \tag{5.6}$$

$$\mu = C\frac{1}{n_{imp}} \tag{5.7}$$

Eq. (5.6) is the same as Eq. (2.46). where $C$ is a constant; $e$ is the elementary charge; and $\sigma_0$ is the minimum conductivity. The relationship of linear conductivity with respect to carrier concentration (Eq. (5.6)) has been validated with experimental results [48], while there have been some discrepancies in terms of the minimum conductivity (Eq. (5.4)) and the carrier mobility (Eq. (5.7)) [48, 57]. For example, inconsistent results have been observed in previous studies between the mobility and the charged impurities concentration (Eq. (5.7)), and the possible reason has been explained as the compensations of the pre-existing charged impurities on the substrate by the incoming charged functional groups and dipolar molecules on the surface of graphene [57]. Other studies have also suggested that the dipole moment of the $H_2O$ molecules on graphene may have a crucial influence on the energy shift of the impurity bands with an underlying ($SiO_2$) substrate [92]. With the intensive studies in the last decade, it is still challenging to precisely model the impacts of the gas-graphene interactions on the electrical properties.

Nevertheless, several measurable quantities are confirmed to be associated with gas-graphene interactions. For example, the asymmetric field effect mobility in this study, i.e., $\mu_e/\mu_h \neq 1$ (e.g., Figs. 5.4**e-j**), can be explained by the difference in the scattering cross sections due to the attractive and repulsive Coulomb forces between the free carriers and the charged impurities, which may exist on the bottom (i.e., pre-existing charged impurities) and/or top (i.e., gas molecules) of the graphene as described in subsection 2.4.3 [59, 93, 94]. Since the Coulomb potential depends on the magnitude of the charge and/or dipole moment of gas molecules, the ratio of the carrier mobility, $\mu_e/\mu_h$, may possess gas-specific information. Indeed, previous studies suggest that $\mu_e/\mu_h$ may be related to the impurity strength (strength of scattering due to charged impurities), $\alpha$, via following equation [59, 93, 94]

$$\frac{\mu_e}{\mu_h} = \frac{n_i^+ C(-\alpha) + n_i^- C(+\alpha)}{n_i^+ C(+\alpha) + n_i^- C(-\alpha)}, \quad 0 < \alpha < \frac{1}{2} \tag{5.8}$$
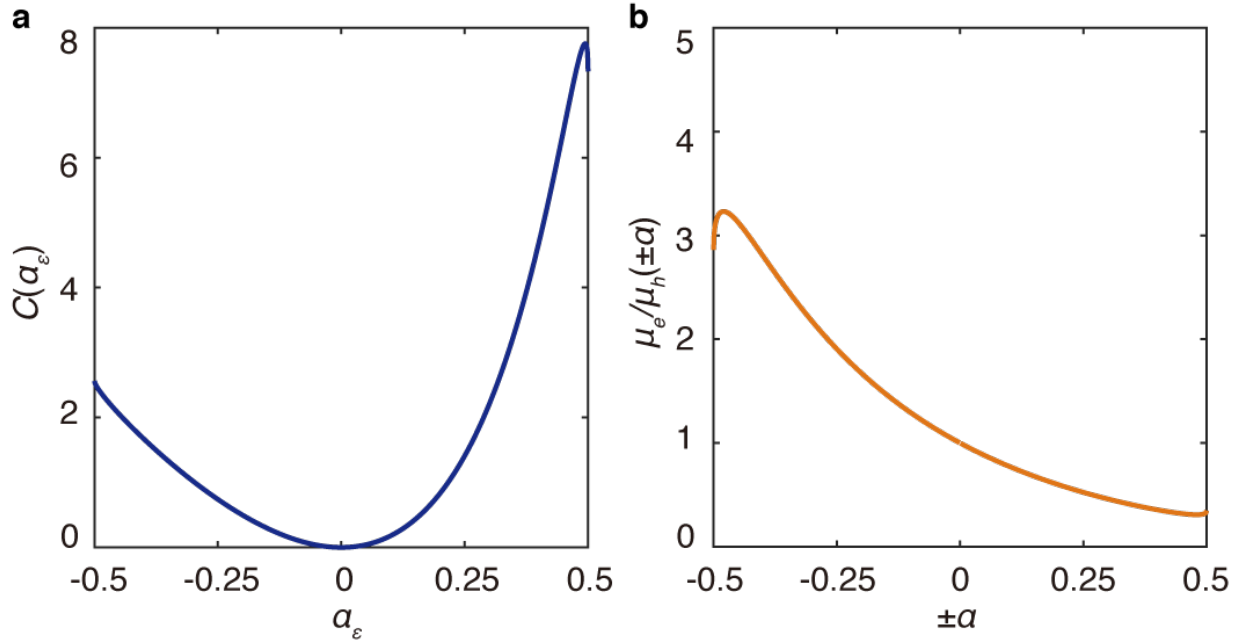
Figure 5.14: The transport cross section (**a**) and the mobility ratio (**b**) with respect to the impurity strength.

where $n_i^{\pm}$ are the concentration of the positively/negatively charged impurities, and $C(\pm\alpha)$ are the transport cross section given by [59, 93, 94]

$$C(\alpha) = \frac{2}{\pi} \sum_{j=1/2}^{\infty} \sin^2(\delta_{j+1} - \delta_j) \qquad (5.9)$$

where $j = 0 + 1/2, \pm 1 + 1/2, \pm 2 + 1/2, \ldots$ is the angular momentum, and $\delta_j$ is the scattering phase shifts given by [59, 93, 94]

$$\delta_j = \frac{1}{2i} \left[ \log \frac{j e^{i\pi(j-\gamma)} \Gamma(1 + \gamma - i\alpha_\varepsilon)}{(\gamma - i\alpha_\varepsilon) \Gamma(1 + \gamma + i\alpha_\varepsilon)} \right] \qquad (5.10)$$

where $\gamma = \sqrt{j^2 - \alpha^2}$, $\alpha_\varepsilon = \alpha \operatorname{sign}(\epsilon)$, and $\epsilon$ represents the quasiparticle energy. Equation (5.8) is reduced to $\mu_e/\mu_h = C(-\alpha)/C(+\alpha)$, or $C(+\alpha)/C(-\alpha)$ when only positively/negatively charged impurities exist. The transport cross section $C(\alpha_\varepsilon)$ and the mobility ratio $\mu_e/\mu_h(\pm\alpha)$ are plotted in Fig. 5.14.

Equation (5.8) allows us to estimate the impurity strength $\alpha$ in our experimental results. The numerically estimated impurity strengths are shown in Fig. 5.15. In all the experimental results, the trend of impurity strength for MeOH and EtOH are qualitatively consistent. The impurity strength of MeOH tends to increase as the gas concentration increases, while

that of EtOH barely changes. On the other hand, the trend of the impurity strengths of $H_2O$ with the pristine-GFET in setup $A$ is inconsistent. This inconsistency may be due to the interactions between the $H_2O$ molecules and the pre-existing charged impurities at the bottom/top of the graphene. When the pre-existing charged impurities are compensated by adsorbed gas molecules, both factors $n_i^+$ and $n_i^-$ in Eq. (5.8) will be modulated, thereby the mobility ratio $\mu_e/\mu_h$.
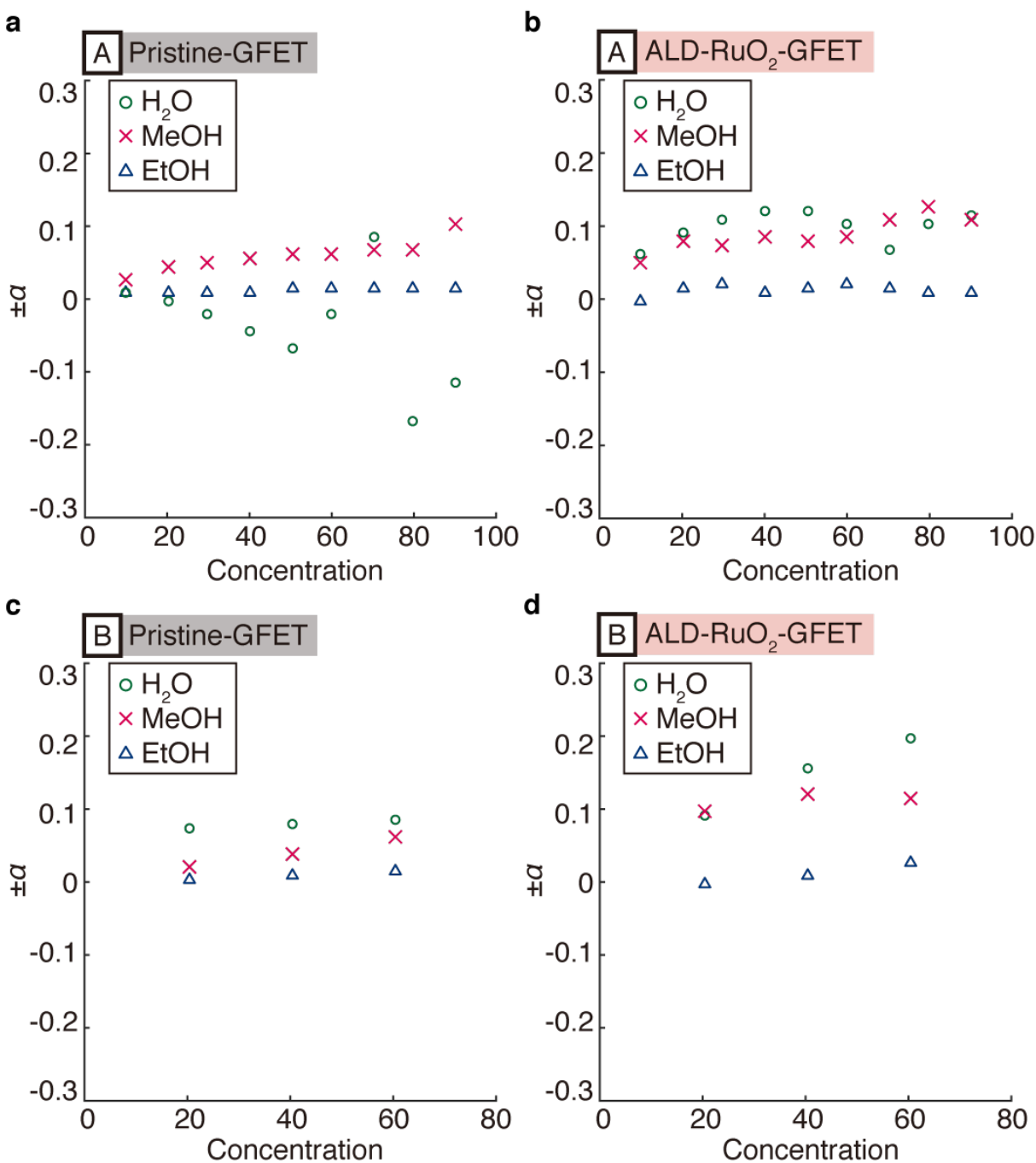
Figure 5.15: The impurity strength with respect to gas concentration for $H_2O$, MeOH, and EtOH with the pristine-GFET in setup $A$ (**a**), the ALD-$RuO_2$-GFET in setup $A$ (**b**), the pristine-GFET in setup $B$ (**c**), and the ALD-$RuO_2$-GFET in setup $B$ (**d**).
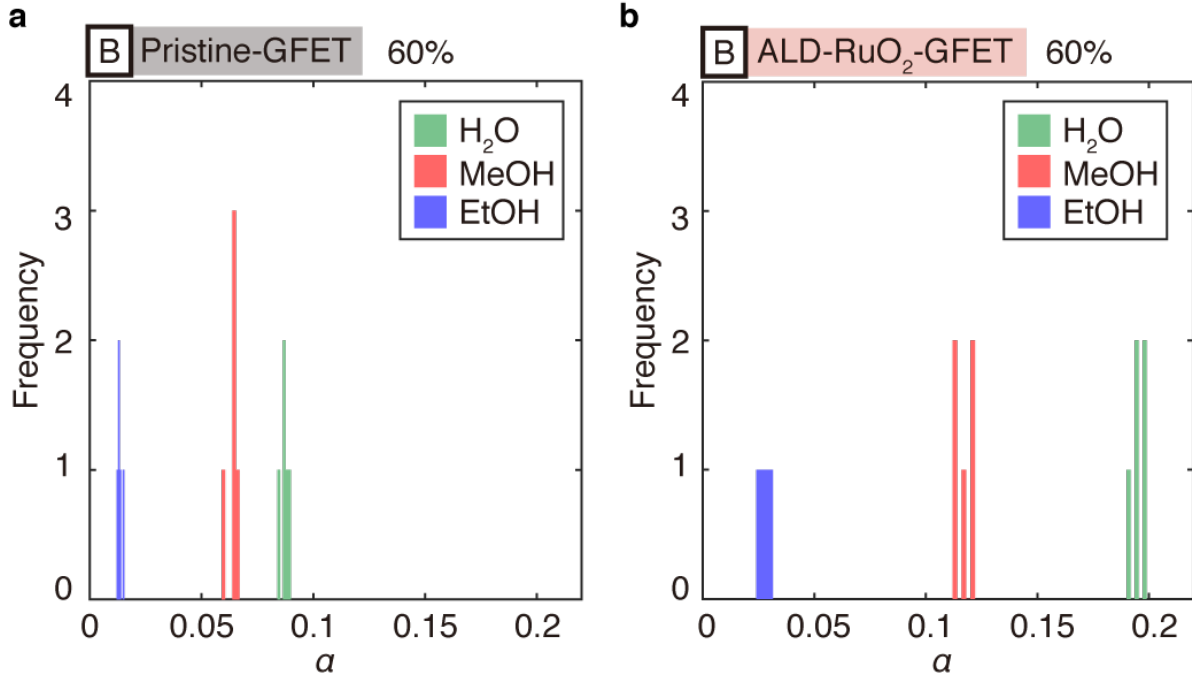
Figure 5.16: The histogram of the impurity strength for 60% of $H_2O$, MeOH, and EtOH with the pristine-GFET in setup $B$ (**a**) and the ALD-RuO$_2$-GFET in setup $B$ (**b**).

In order to see the difference in the impurity strengths for the three types of gases, the histograms for a particular condition (the gas concentration is 60% for all the gases) are provided in Fig. 5.16 form five data points for each gas. The well defined impurity strengths imply that the uniqueness of this quantity contributes to the unique gas sensing patterns.

This speculation qualitatively agrees with the visually distinguishable gas sensing patterns in the $\boldsymbol{q}_{s1}$-$\boldsymbol{q}_{s3}$ plane (e.g., Figs. 5.8**a&d**), which corresponds to $\mu_e$ and $\mu_h$.

In addition to the mobility ratio $\mu_e/\mu_h$, as previously suggested, the term, $\Delta n_{e/h} \Delta \mu_{e/h}$, may be related to gas-specific information [48, 86]. We speculate that $\boldsymbol{q}_{s4}(\sim n^*/n_{imp})$ reflects the interactions between the gas molecules and the pre-existing charged impurities on the substrates. As such, we attribute the origins of the unique gas sensing patterns to the charge and/or dipole moment of the gas molecules and the interactions between the gas molecules and the pre-existing charged impurities on the substrate.

The machine learning analyses allow us to classify the gas sensing patterns in a systematic manner with important statistical information related to the physical properties of the tested GFETs. The one-way ANOVA F-test results indicate that the electron mobility has the highest influences to the gas classification in this study. This type of analysis is possible only when the electrical output signals are decoupled into the physical properties. In addition, the test results suggest that the importance of the features can be modulated by chemical functionalization. Therefore, the contributions of chemical functionalization of GFETs to

selective gas sensing can be systematically evaluated by using the proposed scheme.

The potential limitations of the proposed approach are the required large data collection processes and the intensive computations for the machine learning analyses. The variations in the physical properties of GFET devices warrant a unique machine learning model and training process for each device. From the characterization results of the prototype devices, the accuracy and cross entropy loss history (Figs. 5.13**b&e**) suggest that about 40 epochs of training are enough for a robust neural network model based on the 4D gas sensing patterns. The total time requirement for the training process can be roughly estimated based on the number of epochs, which is almost instantaneous in this study. On the other hand, the time requirement for acquiring one piece of data during the prototype test is one minute, which is currently limited by the specifications of the peripheral measurement system and can be significantly reduced with better instruments. Another key variation is the charged impurity on the substrates (boundary between graphene and $SiO_2$), which can affect the charged impurity states on the substrates. Nonetheless, this issue may be alleviated by improving the quality control of the manufacturing process.

The proposed scheme can be applied to other FET-based gas sensors, such as Si-based FETs, where the threshold voltage and the transconductance may be utilized as key parameters for multi-dimensional vectors. The machine learning approach can be further extended to start with a multiclass model that distinguishes the gas mixture group, and followed by a multi-output regression model to each group for the prediction of concentrations of both the target gas and common humidity values in ambient air. As long as there are sufficiently large training samples with characteristic features, the machine learning scheme should be able to differentiate specific signatures of gas patterns and predict relevant properties.

## 5.5   Conclusion

In conclusion, we have proposed and demonstrated a novel scheme to realize an e-nose using a single GFET by utilizing the distinctive 4D vectors from the results of three tested target gases and the machine learning analysis for gas classifications. As such, by decoupling the electrical output signals from a single GFET, rather than adding multiple chemical functional materials, miniaturization, low power consumption, low cost, and selectivity can be accomplished.

## 5.6   Methods

### 5.6.1   Experimental setup for gas sensing

The gas control system consists of a dry air gas cylinder, three mass flow controller (MFC1, MFC2, and MFC3), two vapor sources, a gas chamber, power sources, and a control and data acquisition system (Fig. 5.3**a**). The gas concentration is determined by the ratio of

two mass flow controllers, and the ratio is controlled over time based on a designated profile (e.g., setups $A$ (Fig. 5.4**a**), $B$ (Fig. 5.6**a**), and $C$ (Fig. 5.11**a**)) through LabVIEW (National instruments). The gas chamber consists of a cap chamber, a GFET test chip, an IC socket, a casing, and BNC connector ports (Fig. 5.3**b**). When the cap chamber is tightened with the screws, the GFET test chip is sealed via the O-ring, and a dome-shaped space with volume of 1 ml is formed. The schematic illustration of the cross section of the cap chamber and the GFET test chip is shown in Fig. 5.3**c**. Throughout all the experiments, the total mass flow rate was fixed at 200 sccm such that pressure dependent false signal is minimized and dry air was used as the carrier gas. The gas control profiles consist of multiple purge (only dry air is injected) cycles and gas exposure cycles of 10 minutes for each test. The conductivity profiles of GFETs were acquired every minute, thereby one gas exposure cycle contains 10 conductivity profiles. In experimental setup $C$, the background relative humidity (R.H.) level was controlled by MFC1 and MFC2, and the target gas concentration was controlled by MFC3.

## 5.6.2   Data preprocessing workflow

A supervised classification study was conducted to substantiate the selectivity of our gas sensor. The task was to train the machine learning (ML) model for each sensor device to distinguish specific target gases with good selectivity. Data preprocessing was performed once raw data was imported to a Jupyter Notebook. During each alternation from a purge cycle to an exposure cycle and vice versa, we removed the first few samples to avoid possibly unstable data between the cycles. Afterwards, a new *label* column was created to denote the target gas species representing each sample's feature vector. Entries in the label column were numerically coded. For a three-class study such as the three different gases tested in this work, each gas type was represented as digit 0, 1, or 2. The next step was to separate the entire data into a training and testing set according to an 80/20 split, respectively. The training set was reserved for the ML model to *learn* about the data and iteratively optimize the classification model, whereas the testing set was served to evaluate the algorithm's performance by giving unforeseen data. All numeric feature values were subsequently normalized by the StandardScaler function in the Scikit-Learn Python library by deducting each numeric entry by their corresponding feature's mean, and then divided by said feature's standard deviation [95, 96]. The purpose of normalization was to prevent features that were numerically greater in value to dictate the outcome of the classification study. To prevent the distribution of the testing set from leaking into the ML model, the mean and standard deviation represented those of the training set only.

## 5.6.3   Multi-Layer Perceptron Model

The ML model that supported multi-class classification to enforce the classification of a sample to one and only one gas type. Various contemporary gas sensor applications such as the e-nose adopted the artificial neural network model because of its ability to model and

predict complex data [33, 34, 97, 98]. The multi-layer perceptron (MLP) classifier, which adopts a feedforward neural network architecture, was implemented for this study. The MLP neural network model contains three components: the input layer, the hidden layer, and the output layer. The hidden layer comprises a set of neurons, which take in a weighted linear combination of the normalized feature values from the input layer plus a bias term, and then pass through an activation function such as rectified linear unit (RELU) [97]. The weight factor $(w(i, j))$ connects the $i$-th entry of the input layer to the $j$-th neuron of the hidden layer. Their outputs are fed to the next hidden layer(s) (should they exist) as the input until reaching the output layer, where the value of each entry correlates to the likelihood of each possible target class. The presence of the hidden layer(s) allows the neural network model to model nonlinear data, and the activation function acts as a means to buffer the noise in data [97]. The neural network model realizes the underlying pattern in data by executing the backpropagation algorithm, which iteratively searches for the optimal weights and biases to minimize the error between the predicted label and the true label. The number of hidden layers and the number of neurons to place within each hidden layer are determined from literary research without yielding a definitive rule of thumb. However, it is ideal to keep the number of hidden layers to 2 and select the number of neurons such that the trained model does not overfit or underfit the data [97]. Scikit-Learn library's API for a MLP classifier object offers plenty of hyperparameters for programmers to modulate [95, 96]. The classifier object was fitted against the training set of each sensor device. Once a stopping criterion of the training process was met, the testing set was then fed to the trained classifier to evaluate the accuracy as well as other pertinent performance metrics.

## 5.6.4 Overfitting and the Cross-Validation Test

Machine learning models face the problem of overfitting, when a model undergoes too much training such that it fits random noise and fails to capture a generalized trend with a significant drop in testing accuracy. Although a testing dataset was explicitly put aside at the onset to evaluate the model's robustness against new data, the concern over whether the testing set constituted a fair representation of all unforeseen likelihoods cannot be ruled out. A cross-validation test is used to detect overfitting for the evaluation of the model performance as a whole. The entire data was randomly shuffled several ways and separated via a stratified split, of which 20% were reserved as the testing set and the remaining constituted the training set. A stratified split ensures that each target class is adequately represented in either set. Data reserved for testing during each shuffle were scored by their corresponding neural network model. By recording the mean and standard deviation of the performance metric (i.e. accuracy), one can interpret whether the ML model is robust against unseen data.

## 5.7 Acknowledgements

## 5.8 Author contributions

T.H. conceived the experiments. T.H. and Y.L. designed the devices. T.H., V.C.C., and L.P.L. fabricated the devices. T.H., L.P.L., Y.K., and Y.L. designed and built up the experiment setup. Y.K. designed and wrote the LabVIEW program. T.H., R.A.L., and L.I.M.B. conducted the experiments. T.H. wrote the MATLAB codes for data processing. A.L. designed and conducted the machine learning analysis. T.H., A.L., and L.L. prepared the manuscript. A.A.S. and L.L. guided the research. All authors contributed to the interpretation of the results and discussions.

# Chapter 6

# Conclusions and Future Directions

## 6.1 Conclusions

This dissertation has reported a series of studies on the three major issues, stability, sensitivity, and selectivity of GFET-based gas sensors. Graphene-based gas sensors are promising miniaturized platforms due to the gas sensing capability at room temperature, unique electrical properties, and the truly two dimensional structure. However, their applications have been severely constrained by the unstable electrical signals in the ambient air, relatively low sensitivity when compared with MOX type gas sensors, and the poor gas selectivity. On the other hand, the concept of e-nose was proposed in the 1980's to tackle the poor gas selectivity issue of chemiresistor type gas sensors; however, the e-nose platforms have encountered various issues including: difficulty of incorporating the assembling process into a batch fabrication process; bulky structure; higher power consumption; and inefficient top-down functionalization process. These challenges motivated us to investigate the possible solutions for the major issues of graphene-based gas sensors with the help of the e-nose concept. The major findings and advancements in this dissertation are concluded in the following subsections.

### 6.1.1 Stability

In chapter 3, the influences of the environmental factors on the stability of the electrical properties and the gas sensing properties of GFETs are studied. The adsorption/desorption dynamics of the ambient gases, $H_2O$ and $O_2$, on the surface of graphene are modeled by physisorption and chemisorption with the help of the discussion in chapter 2. It is found that the influences of $H_2O$ and $O_2$ are drastically changed by the operation temperature. While the sensitivity to $H_2O$ monotonically decreases as the operation temperature increases, that of $O_2$ increases. The analytical results suggest that these behaviors agree well with the physisorption and chemisorption models. These results further imply that the gas sensing performance can be manipulated by the operation temperature. For example, the sensitivity

to a target chemisorption-like gas can be improved, while that of $H_2O$ is reduced. Although the room temperature operation is one of the key advantages of graphene-based gas sensors, the gas sensing performance may be modulated unexpectedly under temperature variations. In addition, the experimental results show that the sensitivity to the ambient gases at the electron regime is significantly higher than that of the hole regime. In other words, the influences of both $H_2O$ and $O_2$ are mitigated in the hole regime, while the operation temperature should be taken into account separately.

These studies strongly suggest that the operation temperature and the gate voltage of GFET-based gas sensors should be properly controlled during the measurements. While higher operation temperature helps to mitigate the influence of $H_2O$, it also leads to higher power consumption. In addition, higher operation temperature may also reduce the sensitivity to a target gas, depending on the required activation energy for the chemisorbed state.

## 6.1.2  Sensitivity

In chapter 4, the sensitivity of GFET-based gas sensor is improved via graphene-ALD-$RuO_2$ hybrid structure. While the gas sensing capability of GFET-based gas sensors is the attractive feature, the sensitivity is relatively low when compared with the heated MOX type gas sensors due to the smaller density of chemisorption sites. Various graphene-based hybrid structures have been proposed with significantly enhanced gas sensing sensitivities; however, most of these techniques are limited with irreproducible fabrication processes. Therefore, we have proposed and demonstrated the reproducible ALD functionalization process. In the proposed device design, the ALD-$RuO_2$ layer is underneath the graphene channel, and gas molecules can still interact with the base ALD-$RuO_2$ layer via the opening holes in the graphene channel. Both electronic and catalytic mechanisms predict that the active catalytic sites of the ALD-$RuO_2$ layer can accelerate either oxidation or reduction process. From a point of view of device fabrication, the advantage of this design is that the graphene channel is not damaged by the functionalization process as the graphene sheet is transferred after the ALD-$RuO_2$ base layer is formed. In addition, this design prevents that the graphene channel is fully covered with the catalytic layer.

In order to evaluate the effect of functionalization, the physical properties of GFETs, e.g., carrier mobility, should be evaluated separately, because the sensitivity based on resistivity/conductivity may vary not only by functionalization, but also depending on the initial doping levels, even for the same pristine-GFET. The decoupled physical properties are also useful to see if there is any unique characteristic feature when they are considered as vectors or patterns. Hence, we have evaluated the gas sensing results in terms of both: (1) whether any of the sensitivities based on the physical properties are enhanced; and (2) whether the vectors composed of the physical properties exhibit characteristic features which may be used for gas classification.

The experimental results show that the ALD-$RuO_2$-GFET tend to have higher sensitivity in terms of the electron mobility, which is up to $\sim 4$ times higher than that of pristine-

GFET. This value may be further enhanced by optimizing the geometry of the holes in the graphene channel. Furthermore, the 4D physical properties vectors provided unique gas sensing patterns for $H_2O$ and MeOH. It is noted that the proposed design allows us to incorporate other materials as the catalytic layer. Hence, the sensitivity may be further enhanced by combining different materials and by optimizing the graphene channel geometry. The gas sensing patterns based on the 4D physical properties vectors are systematically studied in chapter 5.

### 6.1.3 Selectivity

In chapter 5, a novel scheme is proposed and demonstrated to address the poor gas selectivity issue of graphene-based gas sensors. Gas selectivity issue has been one of the most tough challenges in the development of chemiresistor type gas sensors. The poor gas selectivity is especially serious for graphene-based gas sensors as graphene can sense almost any gases including the ambient gases, $H_2O$ and $O_2$, as discussed in chapter 3. The core concept of the proposed scheme is described by the following process flow: (1) the electrical output signals of GFET-based gas sensors are decoupled into four distinctive physical properties of GFET; (2) the four distinctive physical properties serve as 4D vectors; (3) the 4D vectors are modulated upon exposure to the target gases, thereby defined as 4D gas sensing patterns; and (4) the obtained 4D gas sensing patterns are analyzed and classified by machine learning approach. The key advantage of this scheme is that the device does not require chemical functionalization. Therefore, inefficient top down functionalization process is not the limitation of this approach. Since the foot print of the e-nose based on this scheme is identical to the used GFET, a miniaturized e-nose can be realized. The GFET-based e-nose holds all other advantages of GFET-based gas sensors including the low power consumption.

The proposed scheme is experimentally tested by using the pristine-GFET and the ALD-$RuO_2$-GFET with $H_2O$, MeOH, and EtOH as the target gases. The produced 4D gas sensing patterns are first reduced to 3D for visualization purpose by excluding the carrier concentration change. The 3D gas sensing patterns projected to a 3D feature space exhibit consistent trends, rather than randomly distributed. In addition, the gas sensing patterns for each target gas are located in distinctive regions. These results qualitatively suggest that the gas sensing patterns posses unique features. With the help of previous studies, we speculate that the different impurity strengths of the gas molecules contribute to the uniqueness of the gas sensing patterns. The 3D gas sensing patterns show both high local repeatability (consistent within one dataset) and global repeatability (consistent over multiple datasets) for both GFETs.

The proposed scheme is also tested in binary gas mixtures considering a realistic scenario in the ambient air where the R.H. level is generally nonzero. In a series of experiments, the background R.H. level is controlled by varying the $H_2O$ concentration. The target gases, MeOH and EtOH are injected into the test chamber and mixed with the pre-existing $H_2O$, such that binary gas mixtures are composed. The gas sensing patterns for MeOH can be distinguished visually from the one with the background humidity only. The distributions

of each gas sensing patterns for MeOH and $H_2O$ qualitatively agree with the results when they tested separately, suggesting that the gas sensing patterns in the binary gas mixture can be related to the superposition of the individual gas sensing patterns.

The obtained gas sensing patterns are analyzed and classified systematically by using machine learning approach. A multi-layer perceptron classifier with a feed-forward neural network architecture was trained by using 80% of the data, and the rest was used to test the classification algorithm. The trained machine learning models predicted tested gas sensing patterns with high accuracies: a mean accuracy of 95.4% and a standard deviation of 2.5% for the pristine-GFET; and a mean accuracy of 99.6% and a standard deviation of 0.8% for the ALD-$RuO_2$-GFET. It is also found that the accuracy of the model for the pristine-GFET can be further improved by extending the dimension from 4D to 8D by combining the ALD-$RuO_2$-GFET. The one-way ANOVA F-test reveals that the four physical properties have different importance for the gas classification. In this particular study, the electron mobility is the most important feature for both GFETs.

As such, a series of results suggest that the proposed scheme is capable of classifying $H_2O$, MeOH, and EtOH based on the 4D gas sensing patterns in a systematic manner.

## 6.2 Future Directions

The studies in chapter 3 suggest that the operation temperature and the gate voltage of GFET-based gas sensors should be properly controlled during the measurements. The optimum operation temperature should be found through fundamental understanding of gas-graphene interactions for each target gas. Specifically, the adsorption/desorption dynamics of target gases on graphene should be modeled based on the potential energy profiles between the gas molecules and graphene. Temperature control may be also important to accelerate the recovery process. Given that the extremely high surface to volume ratio of graphene, the power consumption of the micro heaters should be much lower than that of conventional MOX type gas sensors. The mechanism of drift may be complex, and many other factors may be involved, e.g., charge/discharge process of charged impurities trapped in the boundaries between graphene and an oxide layer. The mechanism of drift may be further studied through different device structures and fabrication process.

The sensitivity of graphene-based gas sensors may be further improved by using graphene-based hybrid structures. For example, graphene-MOX, graphene-metal, or graphene-2D material junctions may be introduced via micro fabrication techniques. As demonstrated in chapter 4, functionalization process can be performed in a reproducible manner by utilizing standard MEMS fabrication process. The ALD base layer in this study may be replaced by other MOX materials or noble metals as a catalytic layer.

The proposed scheme in chapter 5 should be further studied by modeling gas-graphene interactions. The changes in the physical properties may be theoretically predicted by the model. Given that the conductivity profiles of GFETs are *almost* linear, they are easily simulated via linear algebra when they are linearized. In that case, the gas sensing patterns

may be represented by $4 \times 4$ matrices. The linearization scheme will allow us to study GFET-based gas sensing more quantitatively. Another possible direction is to apply the proposed scheme to other gas sensing technologies, e.g., other FET-based gas sensors, in which the threshold voltage and the transconductance may be utilized as the key parameters.

# Bibliography

[1] *Gas Sensor Market Size and Share, Industry Analysis Report, 2018-2025.* `https://www.grandviewresearch.com/industry-analysis/gas-sensors-market`. Accessed: April 7, 2019.

[2] *Inc, G. M. I. Gas Sensor Market worth over 3 Billion USD by 2024: Global Market Insights, Inc. GlobeNewswire News Room (2018).* `http://www.globenewswire.com/news-release/2018/11/14/1651260/0/en/Gas-Sensor-Market-worth-ove22r-3bn-by-2024-Global-Market-Insights-Inc.html`. Accessed: April 7, 2019.

[3] *Gas Sensors Market worth 1,297.6 Million USD by 2023.* `https://www.marketsandmarkets.com/PressReleases/gas-sensor.asp`. Accessed: April 7, 2019.

[4] S Zampolli et al. "An electronic nose based on solid state sensor arrays for low-cost indoor air quality monitoring applications". In: *Sensors and Actuators B: Chemical* 101.1-2 (2004), pp. 39–46.

[5] Wei Yi et al. "A survey of wireless sensor network based air pollution monitoring systems". In: *Sensors* 15.12 (2015), pp. 31392–31427.

[6] *OSHA Annotated PELs, Occupational Safety and Health Administration.* `https://www.osha.gov/dsg/annotated-pels/index.html`. Accessed: April 7, 2019.

[7] Daniel Rüffer, Felix Hoehne, and Johannes Bühler. "New Digital Metal-Oxide (MOx) Sensor Platform". In: *Sensors* 18.4 (2018), p. 1052.

[8] Antonio Tricoli, Noushin Nasiri, and Sayan De. "Wearable and miniaturized sensor technologies for personalized and preventive medicine". In: *Advanced Functional Materials* 27.15 (2017), p. 1605271.

[9] Xiao Liu et al. "A survey on gas sensing technology". In: *Sensors* 12.7 (2012), pp. 9635–9665.

[10] Manuel Aleixandre and Michel Gerboles. "Review of small commercial sensors for indicative monitoring of ambient gas". In: *Chem. Eng. Trans* 30 (2012).

[11] Naoyoshi Taguchi. *Gas detecting device.* US Patent 3,695,848. Oct. 1972.

[12] Giovanni Neri. "First fifty years of chemoresistive gas sensors". In: *Chemosensors* 3.1 (2015), pp. 1–20.

[13] Noboru Yamazoe and Kengo Shimanoe. "New perspectives of gas sensor technology". In: *Sensors and Actuators B: Chemical* 138.1 (2009), pp. 100–107.

[14] Ghenadii Korotcenkov. *Chemical sensors: Comprehensive Sensor Technologies, Vol. 4: Solid State Devices*. New York: Momentum Press, 2011.

[15] N Barsan, D Koziej, and U Weimar. "Metal oxide-based gas sensor research: How to?" In: *Sensors and Actuators B: Chemical* 121.1 (2007), pp. 18–35.

[16] Joseph R Stetter and Jing Li. "Amperometric gas sensors a review". In: *Chemical reviews* 108.2 (2008), pp. 352–366.

[17] Chengxiang Wang et al. "Metal oxide gas sensors: sensitivity and influencing factors". In: *Sensors* 10.3 (2010), pp. 2088–2106.

[18] Kostya S Novoselov et al. "Electric field effect in atomically thin carbon films". In: *science* 306.5696 (2004), pp. 666–669.

[19] Andre K Geim and Konstantin S Novoselov. "The rise of graphene". In: *Nanoscience and Technology: A Collection of Reviews from Nature Journals*. World Scientific, 2010, pp. 11–19.

[20] Fredrik Schedin et al. "Detection of individual gas molecules adsorbed on graphene". In: *Nature materials* 6.9 (2007), p. 652.

[21] Hai Tan, Deguo Wang, and Yanbao Guo. "Thermal Growth of Graphene: A Review". In: *Coatings* 8.1 (2018).

[22] Frank Röck, Nicolae Barsan, and Udo Weimar. "Electronic nose: current status and future trends". In: *Chemical reviews* 108.2 (2008), pp. 705–725.

[23] Julian W Gardner and Philip N Bartlett. "A brief history of electronic noses". In: *Sensors and Actuators B: Chemical* 18.1-3 (1994), pp. 210–211.

[24] Jessica E Fitzgerald et al. "Artificial nose technology: status and prospects in diagnostics". In: *Trends in biotechnology* 35.1 (2017), pp. 33–42.

[25] *Cyranose Electronic Nose, Sensigent*. `http://www.sensigent.com/products/cyranose.html`. Accessed: June 26, 2019.

[26] *Portable Electronic Nose, Airsense*. `https://airsense.com/en/products/portable-electronic-nose`. Accessed: June 26, 2019.

[27] Andreas Hierlemann and Ricardo Gutierrez-Osuna. "Higher-order chemical sensing". In: *Chemical reviews* 108.2 (2008), pp. 563–613.

[28] Krishna Persaud and George Dodd. "Analysis of discrimination mechanisms in the mammalian olfactory system using a model nose". In: *Nature* 299.5881 (1982), p. 352.

[29] Tetsuo Aishima. "Aroma discrimination by pattern recognition analysis of responses from semiconductor gas sensor array". In: *Journal of Agricultural and food chemistry* 39.4 (1991), pp. 752–756.

[30] Hidetsugu Abe et al. "Automated odor-sensing system based on plural semiconductor gas sensors and computerized pattern recognition techniques". In: *Analytica chimica acta* 194 (1987), pp. 1–9.

[31] HV Shurmer, Jo W Gardner, and P Corcoran. "Intelligent vapour discrimination using a composite 12-element sensor array". In: *Sensors and Actuators B: Chemical* 1.1-6 (1990), pp. 256–260.

[32] Timothy C Pearce et al. "Electronic nose for monitoring the flavour of beers". In: *Analyst* 118.4 (1993), pp. 371–377.

[33] T Nakamoto, A Fukuda, and T Moriizumi. "Perfume and flavour identification by odour-sensing system using quartz-resonator sensor array and neural-network pattern recognition". In: *Sensors and Actuators B: Chemical* 10.2 (1993), pp. 85–90.

[34] F Winquist et al. "Performance of an electronic nose for quality estimation of ground meat". In: *Measurement Science and Technology* 4.12 (1993), p. 1493.

[35] David S Ballantine et al. "Correlation of surface acoustic wave device coating responses with solubility properties and chemical structure using pattern recognition". In: *Analytical Chemistry* 58.14 (1986), pp. 3058–3066.

[36] Yuan Zhao et al. "Novel Gas Sensor Arrays Based on High-Q SAM-Modified Piezotransduced Single-Crystal Silicon Bulk Acoustic Resonators". In: *Sensors* 17.7 (2017), p. 1507.

[37] Frank Zee and Jack W Judy. "Micromachined polymer-based chemical gas sensor array". In: *Sensors and Actuators B: Chemical* 72.2 (2001), pp. 120–128.

[38] Michael Blaschke et al. "MEMS gas-sensor array for monitoring the perceived carcabin air quality". In: *IEEE Sensors Journal* 6.5 (2006), pp. 1298–1308.

[39] AH Castro Neto et al. "The electronic properties of graphene". In: *Reviews of modern physics* 81.1 (2009), p. 109.

[40] Cristina Bena and Gilles Montambaux. "Remarks on the tight-binding model of graphene". In: *New Journal of Physics* 11.9 (2009), p. 095003.

[41] Hideo Aoki and Mildred S Dresselhaus. *Physics of graphene.* Springer Science & Business Media, 2013.

[42] Walter Greiner et al. *Relativistic quantum mechanics.* Vol. 3. Springer, 1990.

[43] Chenming Hu. *Modern semiconductor devices for integrated circuits.* Vol. 2. Prentice Hall Upper Saddle River, NJ, 2010.

[44] Stijn Goossens et al. "Broadband image sensor array based on graphene–CMOS integration". In: *Nature Photonics* 11.6 (2017), p. 366.

[45] A Pirkle et al. "The effect of chemical residues on the physical and electrical properties of chemical vapor deposited graphene transferred to SiO2". In: *Applied Physics Letters* 99.12 (2011), p. 122108.

[46] Yuchen Du et al. "Molecular Doping of Multilayer MoS2 Field-Effect Transistors: Reduction in Sheet and Contact Resistances". In: *IEEE Electron Device Letters* 34.10 (2013), pp. 1328–1330.

[47] Damon B Farmer et al. "Chemical doping and electron- hole conduction asymmetry in graphene devices". In: *Nano letters* 9.1 (2008), pp. 388–392.

[48] J-H Chen et al. "Charged-impurity scattering in graphene". In: *Nature Physics* 4.5 (2008), p. 377.

[49] Shaffique Adam et al. "A self-consistent theory for graphene transport". In: *Proceedings of the National Academy of Sciences* 104.47 (2007), pp. 18392–18397.

[50] P.W. Atkins and J. De Paula. *Atkins' Physical Chemistry*. W.H. Freeman, 2006. ISBN: 9780716771111. URL: https://books.google.com/books?id=Dwv8PAAACAAJ.

[51] Seymour Lowell et al. *Characterization of porous solids and powders: surface area, pore size and density*. Vol. 16. Springer Science & Business Media, 2012.

[52] O Leenaerts, B Partoens, and FM Peeters. "Adsorption of H 2 O, N H 3, CO, N O 2, and NO on graphene: A first-principles study". In: *Physical Review B* 77.12 (2008), p. 125416.

[53] TO Wehling et al. "Molecular doping of graphene". In: *Nano letters* 8.1 (2008), pp. 173–177.

[54] Lingmei Kong et al. "Molecular adsorption on graphene". In: *Journal of Physics: Condensed Matter* 26.44 (2014), p. 443001.

[55] Pierre L Levesque et al. "Probing charge transfer at surfaces using graphene transistors". In: *Nano letters* 11.1 (2010), pp. 132–137.

[56] Yoshiaki Sato, Kazuyuki Takai, and Toshiaki Enoki. "Electrically controlled adsorption of oxygen in bilayer graphene devices". In: *Nano letters* 11.8 (2011), pp. 3468–3475.

[57] Sang-Zi Liang et al. "Screening of charged impurities as a possible mechanism for conductance change in graphene gas sensing". In: *Physical Review B* 90.11 (2014), p. 115410.

[58] EH Hwang, S Adam, and S Das Sarma. "Transport in chemically doped graphene in the presence of adsorbed molecules". In: *Physical Review B* 76.19 (2007), p. 195421.

[59] DS Novikov. "Numbers of donors and acceptors from transport measurements in graphene". In: *Applied Physics Letters* 91.10 (2007), p. 102102.

[60] Gugang Chen, Tereza M Paronyan, and Avetik R Harutyunyan. "Sub-ppt gas detection with pristine graphene". In: *Applied Physics Letters* 101.5 (2012), p. 053119.

[61] Nirav Joshi et al. "A review on chemiresistive room temperature gas sensors based on metal oxide nanostructures, graphene and 2D transition metal dichalcogenides". In: *Microchimica Acta* 185.4 (2018), p. 213.

[62] Yaping Dan et al. "Intrinsic response of graphene vapor sensors". In: *Nano letters* 9.4 (2009), pp. 1472–1475.

[63] Jian-Hao Chen et al. "Intrinsic and extrinsic performance limits of graphene devices on SiO$_2$". In: *Nature nanotechnology* 3.4 (2008), p. 206.

[64] SV Morozov et al. "Giant intrinsic carrier mobilities in graphene and its bilayer". In: *Physical review letters* 100.1 (2008), p. 016602.

[65] Chang-Hee Kim et al. "Effect of Temperature and Humidity on NO$_2$ and NH$_3$ Gas Sensitivity of Bottom-Gate Graphene FETs Prepared by ICP-CVD". In: *IEEE electron device letters* 33.7 (2012), pp. 1084–1086.

[66] Anderson D Smith et al. "Resistive graphene humidity sensors with rapid and direct electrical readout". In: *Nanoscale* 7.45 (2015), pp. 19099–19109.

[67] Ghenadii Korotcenkov. *Chemical Sensors: Comprehensive Sensor Technologies Volume 4: Solid State Devices*. Vol. 4. Momentum Press, 2011.

[68] G Korotcenkov and BK Cho. "Instability of metal oxide-based conductometric gas sensors and approaches to stability improvement (short survey)". In: *Sensors and Actuators B: Chemical* 156.2 (2011), pp. 527–538.

[69] Yeon Hoo Kim et al. "Self-activated transparent all-graphene gas sensor with endurance to humidity and mechanical bending". In: *ACS nano* 9.10 (2015), pp. 10453–10460.

[70] Takeshi Hayasaka et al. "The influences of temperature, humidity, and O2 on electrical properties of graphene FETs". In: *Sensors and Actuators B: Chemical* 285 (2019), pp. 116–122.

[71] Y You et al. "On the mechanism of gas adsorption for pristine, defective and functionalized graphene". In: *Physical Chemistry Chemical Physics* 19.8 (2017), pp. 6051–6056.

[72] Seunghee H Cho et al. "Chemical and biological sensors based on defect-engineered graphene mesh field-effect transistors". In: *Nano Convergence* 3.1 (2016), p. 14.

[73] Andrea C Ferrari and Denis M Basko. "Raman spectroscopy as a versatile tool for studying the properties of graphene". In: *Nature nanotechnology* 8.4 (2013), p. 235.

[74] *Graphenea, Product datasheet of monolayer graphene film on various substrates.* `https://cdn.shopify.com/s/files/1/0191/2296/files/Graphenea_Monolayer_Graphene_on_SiO2_Si_Datasheet_2017-11-23.pdf?15554740513713341332`. Accessed: August 1, 2019.

[75] Yumeng Liu et al. "Defect-Induced Gas Adsorption on Graphene Transistors". In: *Advanced Materials Interfaces* 5.9 (2018), p. 1701640.

[76] Bing Huang et al. "Adsorption of gas molecules on graphene nanoribbons and its implication for nanoscale molecule sensor". In: *The Journal of Physical Chemistry C* 112.35 (2008), pp. 13442–13446.

[77] Yumeng Liu et al. "An AC sensing scheme for minimal baseline drift and fast recovery on graphene FET gas sensor". In: *2017 19th International Conference on Solid-State Sensors, Actuators and Microsystems (TRANSDUCERS)*. IEEE. 2017, pp. 230–233.

[78] Huiliang Liu et al. "AC phase sensing of graphene FETs for chemical vapors with fast recovery and minimal baseline drift". In: *Sensors and Actuators B: Chemical* 263 (2018), pp. 94–102.

[79] Fan-Li Meng, Zheng Guo, and Xing-Jiu Huang. "Graphene-based hybrids for chemiresistive gas sensors". In: *TrAC Trends in Analytical Chemistry* 68 (2015), pp. 37–47.

[80] Shyamasree Gupta Chatterjee et al. "Graphene–metal oxide nanohybrids for toxic gas sensor: a review". In: *Sensors and Actuators B: Chemical* 221 (2015), pp. 1170–1181.

[81] Phung Thi Hong Van et al. "Scalable fabrication of high-performance NO2 gas sensors based on tungsten oxide nanowires by on-chip growth and RuO2-functionalization". In: *ACS applied materials & interfaces* 6.15 (2014), pp. 12022–12030.

[82] RS Niranjan and IS Mulla. "Spin coated tin oxide: a highly sensitive hydrocarbon sensor". In: *Materials Science and Engineering: B* 103.2 (2003), pp. 103–107.

[83] GSV Coles, G Williams, and B Smith. "Selectivity studies on tin oxide-based semiconductor gas sensors". In: *Sensors and Actuators B: Chemical* 3.1 (1991), pp. 7–14.

[84] Kurt E Geckeler and Edward Rosenberg. *Functional nanomaterials*. American Scientific Publishers Valencia, USA, 2006.

[85] Roseanne Warren et al. "Highly active ruthenium oxide coating via ALD and electrochemical activation in supercapacitor applications". In: *Journal of Materials Chemistry A* 3.30 (2015), pp. 15568–15575.

[86] Y Liu, S Lin, and L Lin. "A versatile gas sensor with selectivity using a single graphene transistor". In: *2015 Transducers-2015 18th International Conference on Solid-State Sensors, Actuators and Microsystems (Transducers)*. IEEE. 2015, pp. 961–964.

[87] Nadir Omer Fadl Elssied, Othman Ibrahim, and Ahmed Hamza Osman. "Research Article A Novel Feature Selection Based on One-Way ANOVA F-Test for E-Mail Spam Classification". In: *Research Journal of Applied Sciences, Engineering and Technology* 7.3 (2014), pp. 625–638.

[88] Sergey Rumyantsev et al. "Selective gas sensing with a single pristine graphene transistor". In: *Nano letters* 12.5 (2012), pp. 2294–2298.

[89] Radislav A Potyrailo et al. "Towards outperforming conventional sensor arrays with fabricated individual photonic vapour sensors inspired by Morpho butterflies". In: *Nature communications* 6 (2015), p. 7959.

[90] Eric C Nallon et al. "Chemical discrimination with an unmodified graphene chemical sensor". In: *ACS Sensors* 1.1 (2015), pp. 26–31.

[91]   Hai Hu et al. "Gas identification with graphene plasmons". In: *Nature communications* 10.1 (2019), p. 1131.

[92]   O Leenaerts, B Partoens, and FM Peeters. "Water on graphene: Hydrophobicity and dipole moment using density functional theory". In: *Physical Review B* 79.23 (2009), p. 235440.

[93]   Pawan Kumar Srivastava et al. "Relativistic nature of carriers: Origin of electron-hole conduction asymmetry in monolayer graphene". In: *Physical Review B* 96.24 (2017), p. 241407.

[94]   DS Novikov. "Elastic scattering theory and transport in graphene". In: *Physical Review B* 76.24 (2007), p. 245435.

[95]   Lars Buitinck et al. "API design for machine learning software: experiences from the scikit-learn project". In: *arXiv preprint arXiv:1309.0238* (2013).

[96]   Fabian Pedregosa et al. "Scikit-learn: Machine learning in Python". In: *Journal of machine learning research* 12.Oct (2011), pp. 2825–2830.

[97]   Matthew Kirk. *Thoughtful Machine Learning with Python: A Test-driven Approach.* " O'Reilly Media, Inc.", 2017.

[98]   Simon M Scott, David James, and Zulfiqur Ali. "Data analysis for electronic nose systems". In: *Microchimica Acta* 156.3-4 (2006), pp. 183–207.

[99]   *Marvell Nanofabrication Laboratory.* https://nanolab.berkeley.edu. Accessed: August 1, 2019.

[100]  *NR9-1000PY Negative Lift-off Resist, Futurrex, Inc.* http://futurrex.com/en/products/negative-photoresists/negative-lift-off-resists.html. Accessed: August 1, 2019.

[101]  *MICROPOSIT S1800 Photoresist, Microelectronic Technologies.* http://microchem.com/products/images/uploads/S1800_Photoresist.pdf. Accessed: August 1, 2019.

# Appendices

# Appendix A

# Detailed Fabrication Process Flow

A step-by-step GFET fabrication process flow is described below. The fabrication was performed in the Marvell Nanofabrication Laboratory at the University of California, Berkeley [99]. Some steps include the names of the used tools.

## A.1 Photolithography for the metal contact pads (Fig. 2.3b)

### A.1.1 Photoresist

– Product name: NR9-1000PY NEGA [100]

– Exposure wavelength: i-line, 365 nm

– Exposure dose: 390 mJ/cm$^2$

### A.1.2 Spin coating conditions

– Equipment: Spin coater (headway1 or 2)

– Program number: 7-9 (for custom conditions)

– Rotation speed: 3000 rpm,

– Ramp rate: 5000 rpm

– Duration: 40 sec

– Pre bake: 150°C, 1 min (Better to bake the sample with the same temperature while preparing the spin coater. The sample needs to be cooled down before the spin coating.)

## A.1.3   Exposure

– Equipment: Mask aligner (ksaligner)

– Exposure time (sec): (Exposure dose)/(UV i-line intensity, $x$)=(390 mJ/cm$^2$)/($x$ mW/cm$^2$)

– Post exposure bake (PEB): 100°C, 1 min

– Development: RD-6 (381 cabinet), 8-9 sec (longer development time increases a risk of peeling of graphene), rinse with DI-water, N$_2$ blow

# A.2   Metal deposition (Fig. 2.3c)

– Equipment: Electron beam evaporator (ultek2)

– The first layer: Pd, 25 nm, density: 12.038, z-ratio: 0.357

– The second layer: Au, 30-50 nm, density: 19.320, z-ratio: 0.381

# A.3   Lift-off process (Fig. 2.3d)

– Soak in acetone from a few hours to one night, rinse with DI-water, N$_2$ blow

# A.4   Photolithography for the graphene channel (Fig. 2.3e)

## A.4.1   Photoresist

– Product name: S1818 POSI (common use in Nanolab) [101]

– Exposure wavelength: g-line, 436 nm

– Exposure dose: 150 mJ/cm$^2$

## A.4.2   Spin coating conditions

– Equipment: Spin coater (headway1 or 2)

– Program number: 1 (No need to change the parameters)

– Rotation speed: 4100 rpm,

– Duration: 50 sec

– Pre bake: 120°C, 1 min (Better to bake the sample with the same temperature while preparing the spin coater. The sample needs to be cooled down before the spin coating.)

### A.4.3  Exposure

– Equipment: Mask aligner (ksaligner)

– Exposure time (sec): (Exposure dose)/(UV g-line intensity, $x$)=(150 mJ/cm$^2$)/($x$ mW/cm$^2$)

– Post exposure bake (PEB): No PEB

– Development: MF-26 (common use), 1 min, rinse with DI-water, N$_2$ blow

## A.5  Oxygen plasma etching (Fig. 2.3f)

– Equipment: Plasma etcher (ptherm)

– O$_2$ flow: 80-90 sccm

– RF power: 50 W

– Etching time: 7-10 sec

## A.6  Dicing the substrate (optional depending on the mask design)

– Cut the substrate into 5 mm x 5 mm dice by using a diamond pen

## A.7  Remove photoresist (Fig. 2.3g)

– Soak in acetone, Remover-PG, or 1165 from a few hours to one night, rinse with IPA and DI-water, N$_2$ blow. Although Remover-PG and 1165 dissolve/remove the photoresist better, they also cause peeling of graphene. On the contrary, acetone does not cause peeling of graphene, while the removal of photoresist is incomplete sometimes.

## A.8  Wire bonding

– Fix the substrate onto a test chip by using silver paste and cotton sticks. Twist the substrate with applying force for better adhesion.

– Equipment: Wire bonder (westbond with Al wire)

– Ultrasonic power 1 of 2: 300 (depending on the machine condition)

– Ultrasonic power 2 of 2: 280∼300 (depending on the machine condition)

– Ultrasonic time 1 of 2: 40

– Ultrasonic time 2 of 2: 40